ASIC-Integrated, High Density Flexible Electrode Array with Long-Term Reliability

by

Kyounghwan Na

A dissertation submitted in partial fulfillment
of the requirements for the degree of
Doctor of Philosophy
(Electrical Engineering)
in the University of Michigan
2020

Doctoral Committee:

Professor Euisik Yoon, Chair
Associate Professor Timothy M. Bruns
Professor Khalil Najafi
Associate Professor John P. Seymour, University of Texas Health
Professor Kensall D. Wise

Kyounghwan Na

khna@umich.edu

ORCID iD: 0000-0002-9365-397X

Table of Contents

List of Figures

List of Tables

Abstract

For several decades, extracellular recording has been widely used as a significant tool to understand brain function and behaviors. Extracellular recording enables the isolation of the activity of a single neuron. Therefore, the physiology and connectivity of individual neurons can be characterized by monitoring their activities and, in turn, with the correlation with the behaviors and physiological events. For a broader understanding of brain circuits, more individual neurons have to be simultaneously monitored and thus a larger scale and density of recording sites are required. Another important aim of the neuroscientist is chronic recordings to monitor the plastic change in neuronal network, but the instability of recording over long periods of time has not been fully addressed yet mainly due to biological failure caused by an acute damage and chronic tissue response, and device failure caused by adhesion failure, electrode delamination and insulation failure.

This work is concentrated on three objectives to address the challenges mentioned above and to improve neural interfaces: 1) to minimize acute damage during insertion of a flexible array, 2) to enhance the reliability of polymer-based neural electrode arrays, and 3) to increase the channel count within a limited shank width and with a small system form factor.

For the first objective, a novel T-shaped diamond shuttle to deliver a flexible array with less tissue damage was designed and fabricated. I have developed a versatile T-shaped ultra-nano-crystalline diamond shuttle which provides a 56% reduction in cross-sectional area

compared to a planar silicon shuttle with equivalent insertion strength, and still stiff enough to insert into different neural structures in small and medium animal models with the dura and epineurium intact. This same structure will theoretically reduce micro-vascular damage by 37% compared to standard probes. In vivo experiments with cat DRG and rat brain with dura verified the penetration capability of UNCD shuttle and the neural signals were successfully recorded.

For the second objective, a long-term reliable, high-density polyimide based neural electrode array was developed by submicron patterning and metal-polyimide adhesion improvement for traces. Also, a wafer level impedance lowering process was developed. Submicron patterning process by i-line stepper with an aid of contrast enhance material (CEM) was successfully developed and 64 channels with 0.5μm line and 0.5μm space could be implemented in 85μm width. A novel adhesion layer of TiO_2 was tested and showed a promising lifetime test result indicating more than 6 months of lifetime. A method for wafer level impedance lowering by substrate roughening was developed. The measured impedance of the roughened Pt electrode was 350kΩ at 1kHz and demonstrated 3X reduction compared with plain Pt electrodes. Integrating the presented advances, polyimide based neural probe with 64 channel was fabricated and tested by chronic in vivo recordings. The probe was validated until 14 days after implantation reliably showing 25 single units in average.

For the third objective, ASIC integrated, 256-channel recording system with a 4-shank polyimide neural probe was presented. A 256-channels neural probe with Ni/Au bumped silicon backend was fabricated and interconnected with 256-channel high density ASIC by ACF flip chip bonding. The form factor of the proposed system demonstrated 4X increase in channel count density per package volume. ACF bonding was characterized and measured as 99.7% yield with 3.2Ω of median contact resistance. The system was characterized by an in vitro recording

setup and the noise floor was measured as 17μV_{rms}. An acute In vivo validation was conducted and LFP signal from 198 channels and 20 clusters from spike signal were detected.

Overall, a compact package of 256-channel neural probe with high compliance was developed. Both the channel density per volume and the compliance of the probe were improved compared with the state-of-the-art active flexible probe system. This approach is potentially able to increase the density of package to the level of monolithically integrated system by design optimization maintaining high compliance of the neural probe. The compactness of high density probe recording system is a promising solution for a long-term chronic recording.

Chapter 1.
Introduction

History of recording brain activity

Intracellular recording is a direct mean to study the neurophysiology of a single neuron. However, it is hard to scale and it damages the neuron. Extracellular recording has become the prevailing method to understand brain functions and behaviors. In early research, microwires were used to record neural signals and they evolved into tetrodes[1], [2] and polytrodes[3]. Tetrodes and polytrodes enabled recordings from a larger number of neurons simultaneously. It was noted that a tetrode with 50μm diameter could monitor 100 neurons with successful separation. Microelectrode arrays provide miniaturization and geometry precision, which cannot be done with a tetrode. Also, a much higher density recording is possible thanks to the advances in microfabrication.

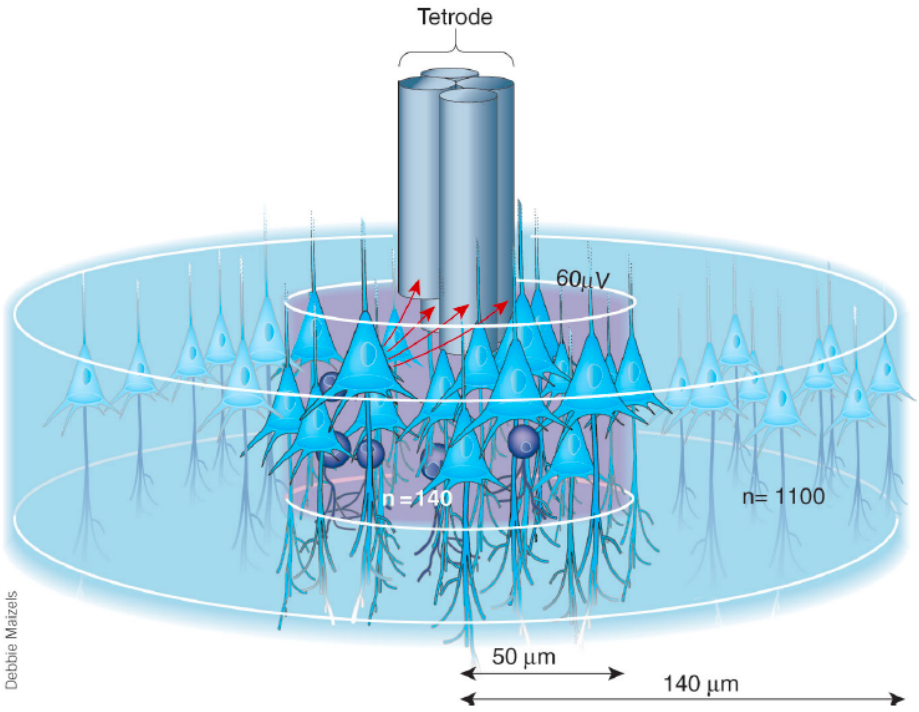

Figure 1. Schematic showing unit isolation quality using a wire tetrode according to the distance[4]

Kensall Wise was the first pioneer who adapted micromachining technology and developed microfabricated silicon neural probes[5]. His group in Michigan has advanced the planar type neural probe for several decades and it is widely called as "Michigan probe" shown in Figure 1-2. The Michigan probe lithographically defines the features on a silicon wafer and can be used to form a multishank array with many electrodes on a shank. It used boron doped silicon as an etch stop in the wafer dissolution process and the process enables needle-like sharp tips. The structure on top of a silicon shank is basically metal layers for the electrode, the traces, and the bonding pads, which are sandwiched by insulation layers. The Michigan probe has two main advantages over the Utah array which will be introduced below. An electrode array can be defined on a shank while the Utah array has only one electrode per shank. The other advantage is freedom of designing the length of a shank unlike the length of the Utah array being limited by

the wafer thickness. Recently, plasma dicing by DRIE and backside dry etching with SOI wafer is a more popular fabrication method due to a low cost and simple process.

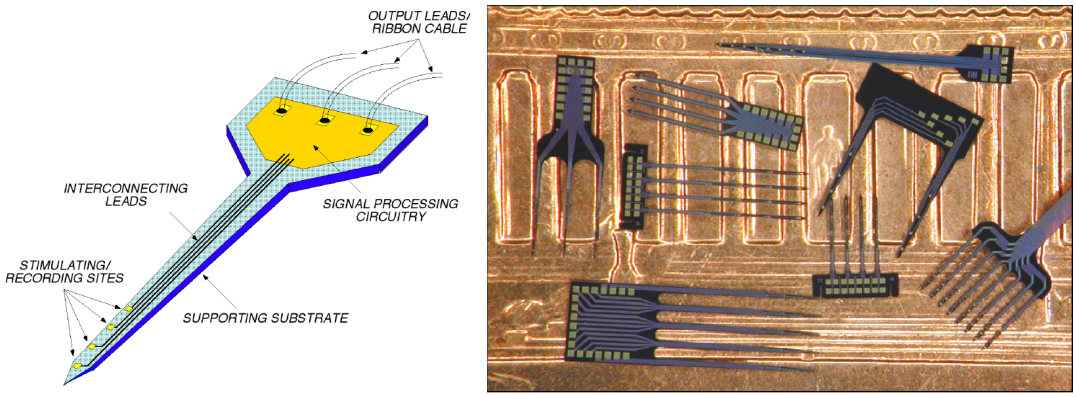

Figure 2. Michigan probe. a, Basic structure of a micromachined multi-electrode probe. b, Several different probe designs shown on the back of a U.S. penny[6].

Another big stream in the microelectrode array is the Utah Electrode Array[7]. It defines the probe shank in a bulk micromachining manner by vertical etching and sharpening of tines. Each tine acts as a single electrode and the typical design has 10 by 10 array of tines. Utah array is known as its good long-term reliability. A big advantage of Utah array is approval by the FDA for human applications[8]. Also, it provides a low profile even integrated with an ASIC due to an out of plane backend.

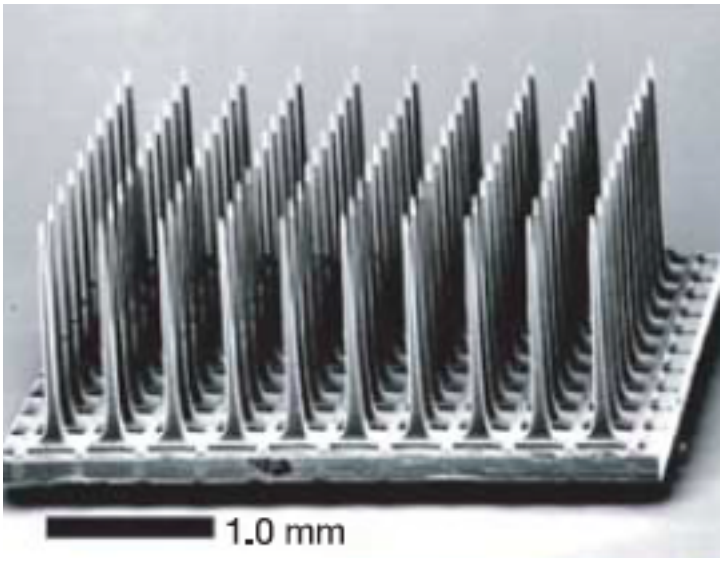

Figure 3. Example of Utah array ([8])

Another form of a neural recording array is a surface array. It is laid on top of the brain rather than penetrated through and thus it is far less invasive. Due to less geometrical limitation by the invasiveness, surface arrays present much higher density recording often monolithically integrated with CMOS array[9]. An advanced version of surface array is the Neurogrid[10]. Even though it has an ECoG configuration, they claimed that neuronal spikes were monitored and single units in motor cortex were detected without an invasive penetration.

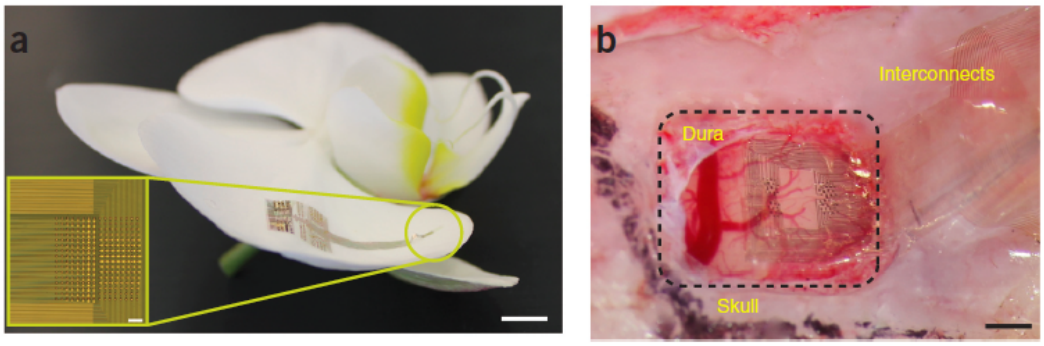

Figure 4. The NeuroGrid on a, an orchid petal. b, a rat somatosensory cortex[10].

High density recording

The lack of a systematic theory about neural activity is complicated by the scale of the human brain, with an estimated 85 billion neurons, 100 trillion synapses, and 100 types of chemical neurotransmitters[11]. Neural probe with large channel count and high density is an essential tool for the large identification of single neurons. According to the neuroscience version of Moore's law, the number of simultaneously recorded neurons has been doubled every 6.7 years since 1960[12]. However, achieving the whole brain mapping is still far off at this increasing rate. The fact justifies the tremendous investment into brain mapping technology, which is ongoing research.

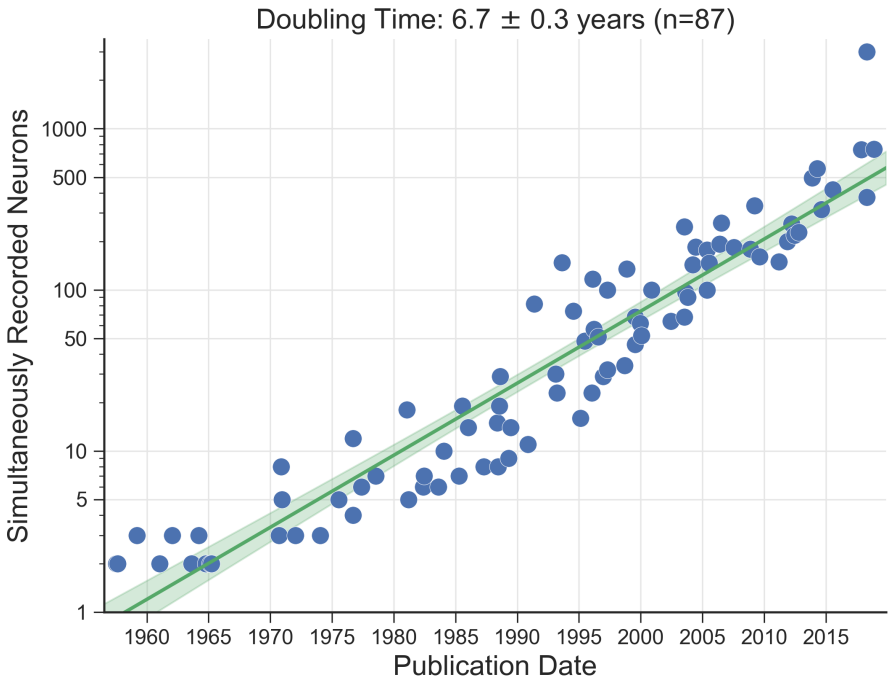

Figure 5. Tracking advances in neural recording[12]

A portion of neuroscientists are still relying on the tetrode for their electrophysiology studies but more neuroscientists are shifting their interest to microelectrode arrays since they

provide explicit advantages over the tetrode, such as miniaturization and geometric precision. Moreover, MEMS technology allows a variety of choices of materials and geometries, and the possibility of the integration with other impactful components such as ASIC, LED, and actuator[13], [14]. Huge number of electrodes also enables increasing the coverage of monitoring, which in turn allows recording from many neurons spanning multiple brain regions.

Increasing the density by accommodating a large number of electrodes within a limited width can be achieved by advanced microfabrication technologies. Scholvin et al demonstrated the first 1,000 channel neural probe by using electron beam lithography (EBL) and patterning 200nm-wide metal traces[15]. They showed the feasibility of the extension towards closed packed electrode array even though their gigantic package is not applicable to any neuroscience study beyond a head-fixed acute experiment. The researchers at HHMI and Imec developed a 966-electrode CMOS neural probe with 384 configurable channels using 130nm CMOS process on silicon-on-insulator (SOI) wafer[16]. It utilized advanced lithographic technology for CMOS process in order to implement a large number of electrodes within a 70μm width. Also, it eliminated a burdensome interconnection process with the assistance of a monolithically integrated multiplexer. One drawback is that this approach is limited to a silicon probe as of now due to a lack of comparable CMOS solution for polymer array.

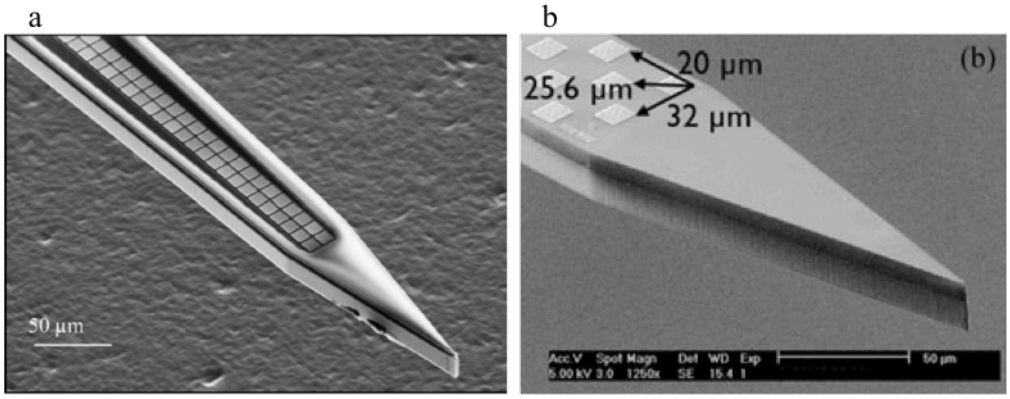

Figure 6. Recent advanced in high density neural probe. a, using E-beam lithograph[15]. b, using CMOS process[16].

Tissue response

The signal quality of recordings from an implantable neural probe typically degrades over time after insertion. It is believed that the foreign body reactions related to glial encapsulation, blood-brain barrier (BBB) breach, and loss of neuron cells is responsible for the quality decline[17]–[19]. The detrimental tissue reaction is complex and intertwined, and it includes insertion damage[20], [21], the intrinsic foreign body response[22], and micromotion-induced damage[23], [24]. Obviously, the implant size is a major factor to affect the insertion damage. It is almost impossible to avoid the blood vessel invasion if the implant size is beyond several tens of microns since the averaged distance between a neuron and a microvasculature is 15µm[25].

Relative motion of an implant due to respiration, vascular pulsatility, and head movements applies displacements and strains to the tissues around the implant[24], [26]. A sustained immune response is also associated with the implant size according to many related studies. Seymour et al demonstrated that the smaller structure showed significant advantages both in neuronal density and non-neuronal density[27]. Others also reported that the implant size is a critical factor for the local tissue reaction and the reduced astrocyte and microglia density was observed for sub-cellular structures[28].

Another factor to affect the tissue response, which is recently regarded more importantly, is the compliance of the implant. A large compliance mitigates the micro-motion effect by accompanying the tissue more than a stiff implant. The less tissue response with a flexible probe has been supported by other studies[29]–[32].

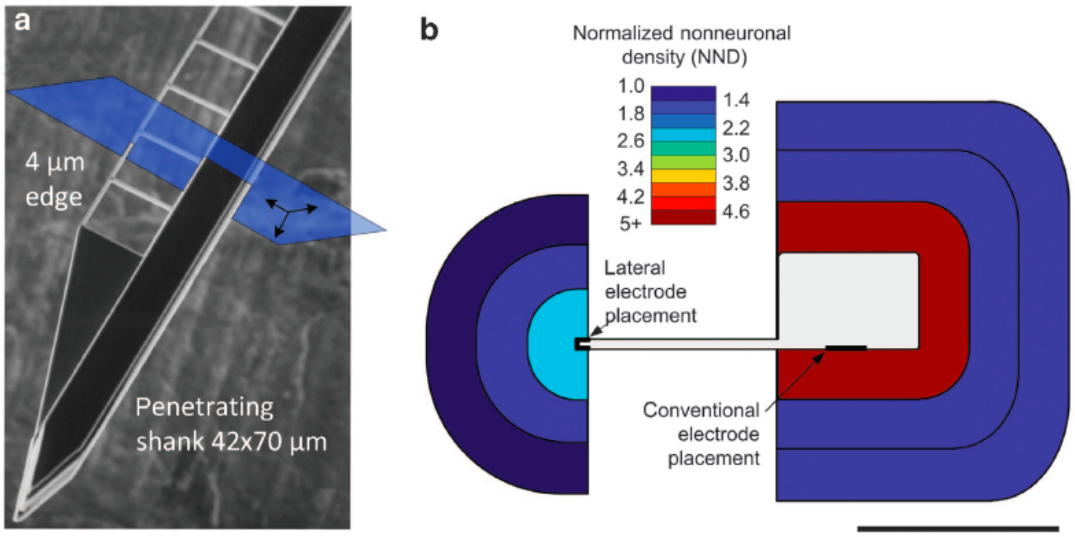

Figure 7. Seminal work supporting the hypothesis that the tissue response is a function of local device structure[27].

Flexible neural probe

Silicon has been extensively exploited in neural implants thanks to its excellent mechanical/electrical properties and the advances in Si microfabrication technology. Recently, another aspect has been taking into the consideration. A huge mechanical mismatch between Si implant with ~160GPa modulus and the surrounding tissues with several kPa modulus keeps inducing strain while an animal moves and respires. The relative displacement due to the micro-motion effect is in an inverse proportional relation with the compliance of the implant. There exists more obvious mechanical constrains, which is the implant's capability of penetration. Unfortunately, both the buckling load that determines the penetration capability and the

compliance are functions of E*I where E is Young's modulus and I is moment of inertia. Given a targeting buckling load, the compliance of the geometry is already limited.

There has been an emerging interest in highly compliant probe to minimize the sustained tissue response. Researchers have attempted to insert flexible arrays with assistance from a dissolvable stiffener, thread and needle, or a removable shuttle. Wu et al. demonstrated parylene-C based neural probe with dissolvable silk coating as the stiffener[14]. The silk patterning was precisely controlled and minimized just sufficient for the penetration but the dimension of stiffener had to be far much larger than silicon or carbon shuttle due to the low mechanical stiffness of silk. Recently, several groups have reported their triumphs in long-term chronic recording on implanted animals. Charles Lieber group in Harvard has developed SU-8 based ultra-flexible neural probes forming mesh structures with sub-micron thickness to achieve the bending stiffness to the level of the brain tissue[33], [34]. Yang et al. demonstrated a stable chronic recording result for more than 3 months and almost scar-free histology from their Neuron-like electronics (NeuE) with 0.9μm thickness and 1μm interconnect in mesh structure[33]. Fu et al. reported scaling up of SU-8 based mesh electronics up to 128 channels by increasing the width of the interconnect to 20μm[34]. Luan et al. presented another ultra-flexible neural probe based on SU-8 with 1μm thickness and its successful insertion using 10μm-diameter carbon fiber as an inserter[35]. They also validated that the probe functionality maintained for more than 4 months via chronic in vivo recordings. Guan et al. demonstrated polyimide version of the mesh electronics with 1.5-3 μm thickness extended to 1,024 channels[36]. They flip-chip bonded the backend of the probe to FPC using anisotropic conductive films (ACF). However, the head stage for 1,024 channels might be very bulky since it is a passive type head stage though they didn't specify the head stage for 1,024-channel device.

Loren Frank group in University of California, San Francisco has developed a 1,024 channel, polyimide based neural probe[37]. Chung et al. presented 64-channel active head stage integrating recording IC (Intan tech., RHD2164) and polyimide based neural probe with 3 metal layers in 14μm thickness and 80μm width. Also, they provided a packaging solution for 1,024-channel by stacking 16 of head stages and control board with FPGA. They used a trenched silicon shuttle for the convenience of the mounting process and demonstrated successful insertions. Reliable chronic in vivo recordings were presented from their 64-channel probes but no chronic result from 1,024-ch system was provided probably due to its bulkiness. The recent works of polymer based flexible neural probe are summarized in **Figure 8** and **Table 1**.

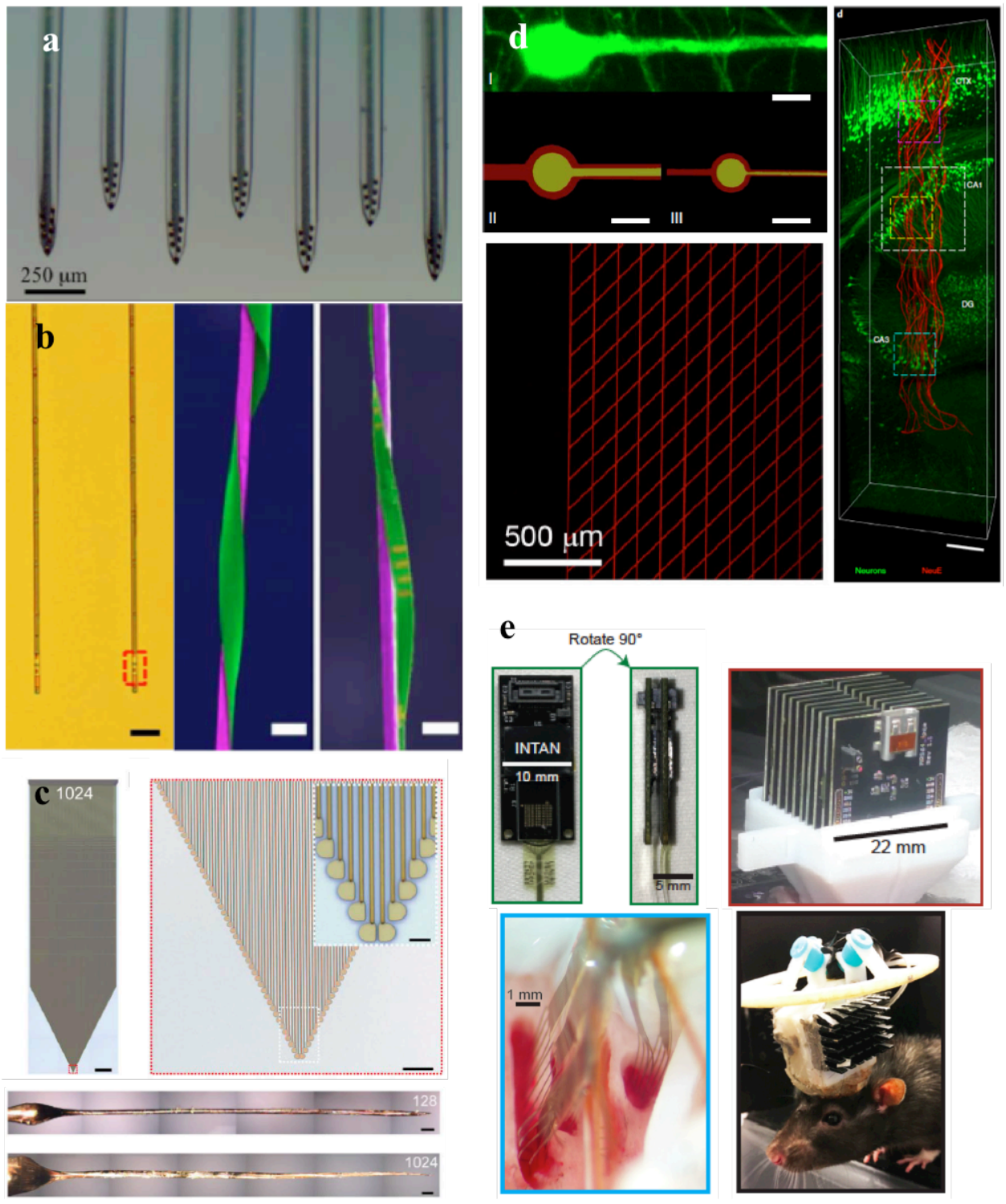

Figure 8. Recent advances in flexible neural probe a, Wu[14]. b, Luan[35]. c, Guan[36]. d, Yang[33]. e, Chung[38].

Table 1. Summary of recently reported polymer based flexible neural probes.

Authors	Material	Probe dimensions		Trace	# of site per shank	Total sites	Package type /rec. system	Chronic Recording	Publication, year
		w (μm)	t (μm)						
Chung & Frank	Polyimide	80	14	Ti/Au/Ti 3 layers	64	1,024	Active /Intan	> 160days	Neuron, 2019
Guan & Feng	Polyimide	3	1.5	Cr/Au/Cr	1	1,024	Passive	6 weeks	Sci. Adv., 2019
Hu, Meng	Parylene	150	20	N/A	8	64	Passive	-	JNE, 2018
Yang & Lieber	SU-8	1	0.9	Au	1	16	Passive /Intan	3 months	Nat. Mat., 2019
Fu & Lieber	SU-8	20	0.9	Au	4	128	Passive /Intan	4 months	PNAS, 2017
Luan & Xie	SU-8	10	1.5	Au	8	32	Passive /Intan	4 months	Adv. Sci., 2018

Proposed work

My goal in this work was to provide a sustainable, high density neural electrode package for chronic study. This work is concentrated on three objectives to continue the Michigan probe lineage; 1) to minimize the adverse tissue response including the acute damage during insertion and the strain-induced damage over time, 2) to improve the reliability and lifetime of polymer-based neural electrode arrays, and 3) to implement a high density array within a miniaturize package

Chapter 2.
Novel Diamond Shuttle to Deliver Flexible Array with Reduced Tissue Compression

Motivation towards strongest shuttle ever made

Implantable sensor arrays, especially when deployed in neural mapping studies, are most accurate and insightful when damage and disruption to nervous system circuitry is minimized. Minimizing damage and reactivity has been emphasized by recent global initiatives including the BRAIN Initiative, the NIH SPARC program, the GSK Innovation Challenge, and several DARPA funding programs, which have supported the development of new technology for mapping, monitoring, and/or controlling the nervous system with higher fidelity and longevity. Previous work demonstrated that size of an implant affects the neuron count and several glia markers of reactivity[27], [39]. A precise implant size to tissue damage function is still missing, but evidence suggests that care should be taken to minimize the damage to blood vessels which densely permeate nervous tissue[20], [40]. Central nervous system (CNS) neurons, for example, are located within ~15 μm of a capillary vessel[25], [41], [42] so damage to the blood-brain barrier is unavoidable. When designing an implantable device, the penetrating structure must be stiff enough to reach the desired target with accuracy and, more challenging, piercing a tough fibrous outer membrane protecting the neurons. These challenges have opposing solutions – make the device as fine as possible for minimal bleeding and cellular disruption, yet ensure it is sufficiently stiff so as not to buckle or move off-target during penetration. The challenge is underscored when the covering membrane, the epineurium or dura mater in the peripheral or central nervous systems respectively, is left intact during insertion.

Epineurium and dura mater are made of collagen fibers interspersed with elastin and fibroblasts that are at once tough and flexible[43], [44]. Cranial and spinal dura mater have a Young's modulus in the range of 2-100 MPa[45] (depending on species and location) and so compared to the parenchyma, whose modulus is ˜5 kPa, provide the primary resistance to device insertion. In the feline dorsal root ganglia (DRG), the epineurial thickness is in the range of 20-100 micrometers (typically 80μm)[46]. The dura can often be separated with minimal damage to the parenchyma below with surgical training and skill, however the creation of dural flaps severs blood vessels extending into brain and allows the brain to swell and dehydrate[20]. Furthermore, surgically removing the epineurium at the DRG or further into the periphery is not done in practice without damaging the nervous tissue. As such, a minimally invasive solution to penetrating through CNS and peripheral nervous system (PNS) membranes is needed.

State-of-the-art sensor arrays have taken different approaches to the problem of penetration when the membrane cannot be removed. One high-density and popular electrophysiology research tool is the "Utah" array[47], [48], which is a silicon array comprised of many ~70 μm diameter needles. It is inserted with a pneumatic insertion tool and can achieve an insertion velocity of 12 m/s[49]. The array has a wide base so it naturally stops when fully inserted but also may induce significant compression or impact trauma. No published quantification of the insertion force and compression distance exists, but significant bleeding has been reported[22], [50]. Potentially related to this issue, the histology clearly shows encapsulation around the shank tips[50]–[52] with a typical electrode-tip to axon distance of 40 to 150 μm. The resulting tissue restructuring around these microelectrodes prevents high-fidelity chronic recording, although it is still effective in recording population-based compound action potentials and for electrical stimulation[53]. Another popular recording/stimulation array, but

with a smaller footprint and greater electrode density, are planar silicon probes. Historically these have been called “Michigan” arrays but these micromachined silicon structures are now made by many groups[6], [16], [54]–[56] and companies. They are typically inserted in the CNS using a manual manipulator at a moderate speed so as to monitor for buckling during insertion. Given the risk of buckling or fracture, silicon planar probes are rarely used to penetrate tough membranes such as the dura and epineurium and there is even less known about the insertion mechanics. One study demonstrated there is a chronic breach in the blood-brain-barrier for rigid intracortical structures[57].

New research has been focused on implanting flexible arrays with assistance from a variety of techniques. Given the impressive flexibility and stretchability of nerves, ganglia, and the spinal cord, researchers have attempted to insert flexible forms of microelectrodes. The most common insertion techniques are pulling the array through the tissue using thread and needle, a dissolvable stiffener, or a removable shuttle, otherwise known as a stylet. Several groups have demonstrated the pull-through technique for intrafascicular recording used a fine commercial needle and suture[58], [59]. The diameter of these suture needles is hundreds of microns and risk causing significant trauma. As Wurth, et al., carefully demonstrated in their histology the electrode to axon distance is typically 100 microns or more over time[59]. A dissolvable stiffener comes at the cost of greater volume given the temporary material is several orders of magnitude less stiff than many inorganics[14], [60], let alone the potential reactivity induced by the degraded polymer itself. The shuttle or stylet approach[35], [38], [39], [61], [62] allows for stiffer materials and thus a smaller footprint than commercial needles or organic stiffeners. However, none of those approaches would allow for insertion through a tougher membrane without making the substrate much larger and at the cost of a significantly more tissue damage.

We sought to address the combined insertion challenge of minimizing the cross-sectional area and the tissue compression. This work added to previous research using a shuttle approach but having a unique T-shaped geometry and material to form a three-dimensional ultrananocrystalline diamond (UNCD) shuttle with 13-fold greater stiffness than a similar cross-section made with conventional silicon (**Figure 9a**). UNCD has the highest modulus of elasticity (800-1000 GPa)[63], [64] of any conformal thin-film and 5X and 3X higher than silicon[38], [62] and carbon[35]. We also successfully fabricated T-shaped UNCD shuttle using trench refilling process (**Figure 9b**). We used the shuttle to demonstrate the delivery of and neural recordings from an ultra-compliant polyimide array (**Figure 9c**). We expect this new ability to deliver higher-density bioelectronics with less compression and less vascular damage will improve the understanding of CNS and PNS function.

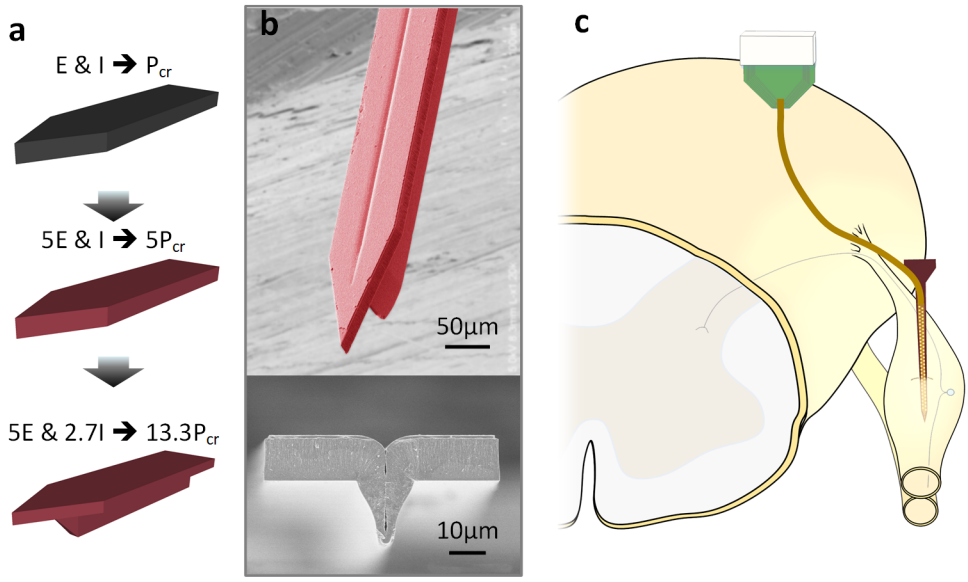

*Figure 9. Insertion concept, design concept, and fabrication of a ultra-nano-crystalline diamond (UNCD) shuttle. a, Progression of design improvement from a simple silicon shuttle, with a buckling load of Pcr, to an improvement of 13.3*Pcr by changing the Young's Modulus, E, and moment of inertia, I. b, SEM of released UNCD shuttle. c, Insertion of flexible electrode array into a dorsal root ganglia (DRG) using a rigid shuttle and retraction.*

Analysis on blood vessel invasion

While a reduction of area potentially leads to diminution of insertion damage to tissue, we have no biological evidence that this rule is still valid for T-shaped geometry. To address this, we modeled the damage using an available model of the density, size, and length of micro-vascular segments in the brain.

A publicly available three-dimensional micro-vascular network data for rat brain was used to simulate the blood vessel invasion induced by the insertions of various geometries. For simplicity, the 3-D model was projected into a 2-D plane assuming that the insertion was vertical and straight. We overlaid the contour of a variety of devices onto the microvasculature maps provided initially by scanning electron microscope (SEM) imaging and 3D reconstruction. The model assumes that the device contour damages any vessel when it crossed the entire width of a segment. This approach allows us to assess the performance of T-shape geometry in terms of a quantitative analysis of blood vessel invasion. The numbers of micro-vascular segments cut by

the footprints of the shanks were counted throughout 1,000 insertion iterations with randomized angles and locations for each geometry (**Figure 10 and Figure 11**). The distribution of the number of damaged blood vessels was fit to a Gaussian distribution to extract the mean value and the deviation.

The chosen T-beam cross-section contour was 11 x 65 μm on the planar portion and a vertical support that was 27.5μm-deep that tapered from 16 to 2μm-wide. This T-shaped UNCD (T-UNCD) was used for this model and throughout the study. The silicon device that has an equivalent buckling strength is 34-μm thick. All devices in this study are 65-μm wide which is generally the accepted width of a minimally damaging brain probe for chronic recording. On average the simulation produced a 36.6% reduction in blood vessel damage caused by the T-UNCD relative to the Si-34 rectangular silicon device (**Figure 10**).

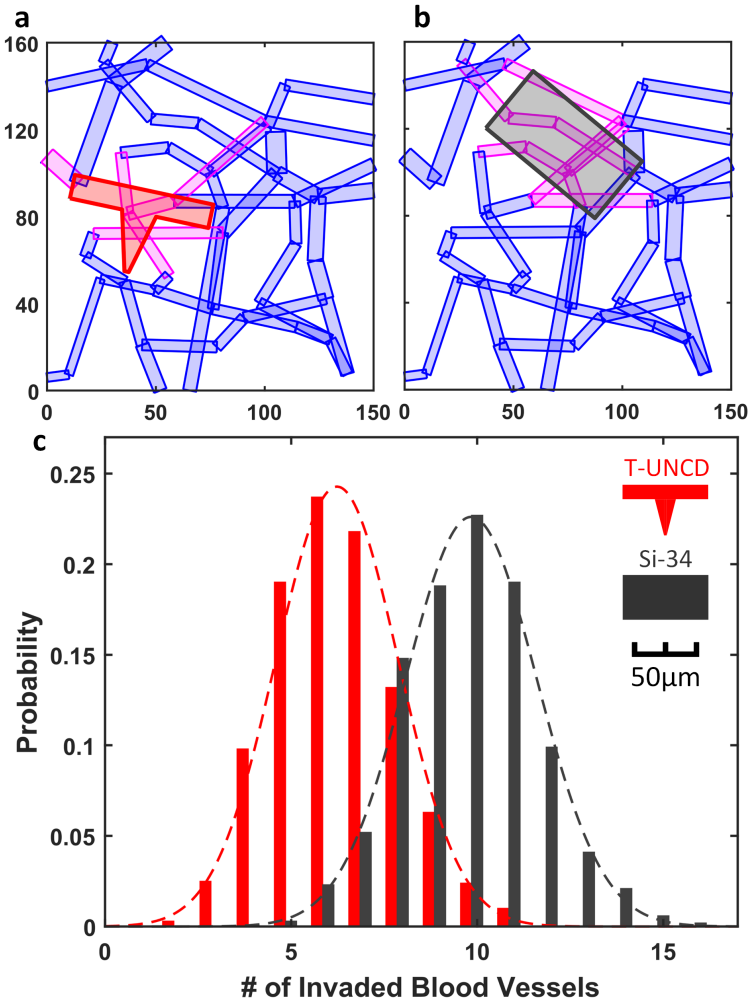

Figure 10. Simulation result of blood vessel invasion comparing Si (dark gray) and T-UNCD (red) having an identical buckling strength. Examples of invasion analysis with a, T shape with 65µm by 11µm on the planar portion and 27.5µm-deep, 16µm to 2µm-wide trapezoid for the vertical support, which has identical buckling strength with (b). b, 65µm by 34µm rectangle. c, Simulation result of 1,000 insertions yielded a Gaussian distribution of the number of invaded blood vessels. Mean values of two geometries from (a-b) were 6.23 and 9.84, respectively. Invaded blood vessels in (a-b) indicated in magenta. X and Y labels in (a-b) indicated the coordinates in µm.

Two important points of reference are a 15-µm thick silicon probe, which is sufficient for insertion in rodent models with the dura removed, and another commercially available neural probe that is 50-µm thick and intended for larger animal models. We compared these two against a T-UNCD structure that has equivalent stiffness with Si-15 (T-UNCD SMALL) and is considerably smaller in area. The simulation results were 1.4 vessels damaged compared to 5.8

vessels damaged by Si-15. By contrast, the 65x50-µm geometry caused damage that was 9.7-fold greater than the smaller T-UNCD (**Figure 11**).

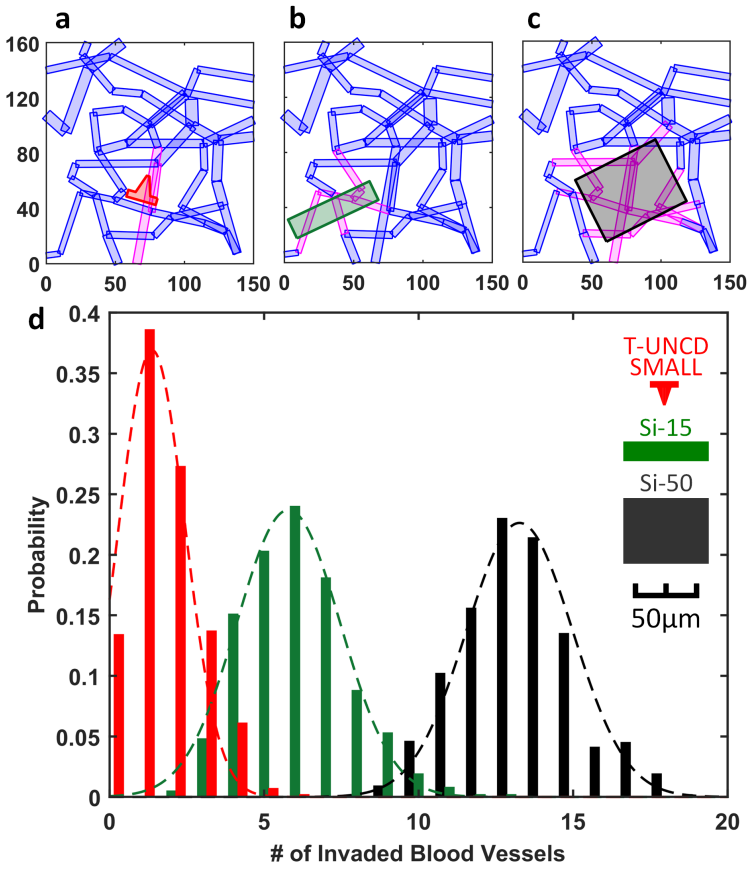

Figure 11. Simulation of blood vessel invasion based on various probe cross-sections. Examples of invasion analysis with a, T shape with 22 x 5 µm on the planar portion and 13.5µm-deep, 11 to 2µm-wide trapezoid for the vertical support (red, T-UNCD SMALL). b, 65µm by 15µm rectangle (green, Si-15). c, 65µm by 50µm rectangle(black, Si-50). d, Simulation of 1,000 insertions result in a Gaussian distribution of the numbers of invaded blood vessels. Mean values of three geometries from (a-c) were 1.4, 5.8, and 13.3, respectively. Invaded blood vessels in (a-c) indicated in magenta. X and Y labels in (a-c) indicated the coordinates in µm.

Trench filling with UNCD

The sticking coefficient (η_0) is a property of CVD deposition and is the most important parameter in determining a film's conformation around 3-D structures. η_0 is dependent on pressure, temperature, and the nature of each species, etc. Theoretically, the shape of the trench and the sticking coefficient determine the deposition profile. The sticking coefficient of UNCD deposition varies in a large range, and our specific conditions and sticking coefficient were

unknown because the hot filament chemical vapor deposition method used for this work was provided by an outside vendor and the details were proprietary. The challenge of trench filling of UNCD is the moderate conformality of the UNCD film. For example, the trial for the trench refilling showed a huge void since the concentrated deposition at the trench neck pinched off the trench too early (**Figure 12**). Therefore, a deposition modeling was critical for defining the proper silicon trench profile and thus minimizing void creation in the shuttle's vertical support.

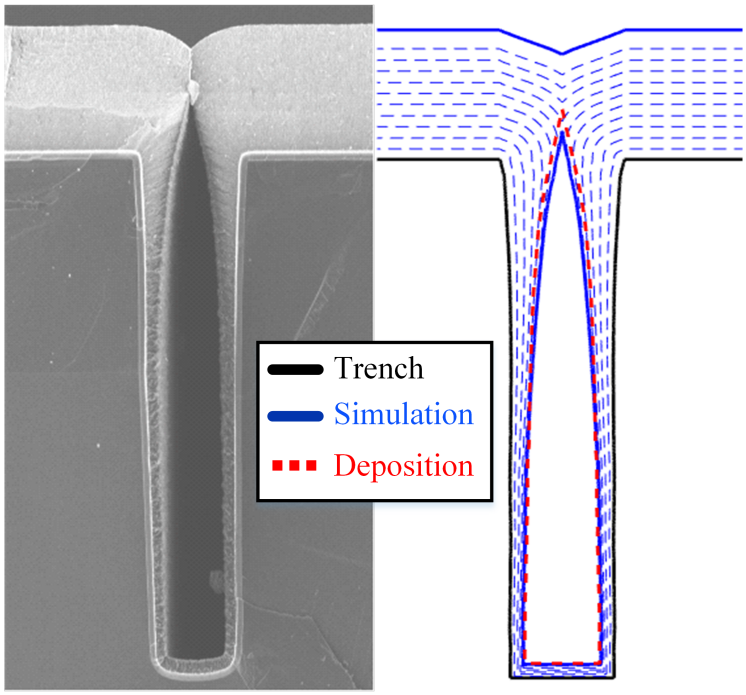

Figure 12. Failure of trench refilling in a vertical trench and prediction by the deposition model.

We developed a method to model the deposition profile and estimate the sticking coefficient during deposition. Ganguli et al[65] and Komiyama et al[66] suggested the governing equation of deposition model based on the mass conservation and it was reformulated as shown below. It was assumed that the width of trench is constant along with the depth as well as time. The assumptions are inappropriate due to tapered profile and increasing film thickness over time. The derivative equation becomes unsolvable form and analytical solution cannot be derived.

$$\frac{d}{dy}\left(\frac{2W^2}{3\eta_0}\frac{dC}{dy}\right) = C$$

Equation 1

where W is the width of trench, η_0 is the sticking coeffieient, and C is the concentration of reactant. Instead, we converted the derivative equation to a discrete form and iterated the calculation according to the depth and the time. The film thickness deposited on discrete coordinates of y during a unit time was calculated with the fixed width and then the width was updated considering the deposited film for the following calculation during the next unit time. The calculation was iterated until the time when the targeted total thickness was achieved.

Our deposition model fits best (R^2>0.94) with a sticking coefficient, η_0 = 0.079, which is a moderate sticking coefficient[67]. It suggested that the void formed would be less than 0.4 μm across when the trench's taper angle is less than 70˚. We fabricated various tapered trenches on Si using the combination of DRIE and isotropic dry etching of Si targeting less than 70˚ of tapering angle. The model predicted a slight hollow in the middle of the trench since the etched profile was not linear and the sidewall angle of some portion was above the critical angle (70˘) for void-free filling even though the averaged angle was more tapered. Since a small void has a small change in the moment of inertia, we also expect a small loss of mechanical strength. We confirmed that the model is well fitted to the actual deposition profile through several different geometries (**Figure 13**).

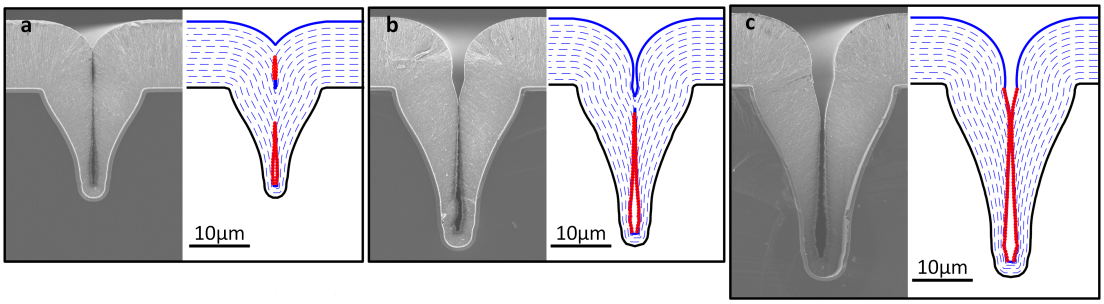

Figure 13. Simulation result of UNCD profile modeling. a, design A with 18.3μm-deep trench, R2=0.957. b, design B with 26.9μm-deep trench, R2=0.946. c, design C with 32.2μm-deep trench, R2=0.943. Blue solid line is the final outline of UNCD film. Blue dashed lines show the progression of deposition. Red lines indicate the measured profiles of UNCD film.

The angle of the silicon trench can be modified for deeper or wider geometries by combining different doses of isotropic and anisotropic dry etching. But, it is noted that the residual stress of UNCD film is not consistent during deposition and the resulting gradient make it challenging to control or compensate for residual stress with a thick film UNCD. Therefore, the moderate sticking coefficient and stress gradient will eventually limit the aspect ratio and film thickness so the upper limit of strength we estimate to be in the range of 65 gf based on our current film properties. This is sufficient for all of the animal models for which we currently have data.

Design and Fabrication

The process flow for the simple fabrication with two masks is illustrated in **Figure 14**. First, standard photolithography defined a trench pattern on a 4" silicon wafer. A tapered trench was formed on silicon wafer by the combination of DRIE and isotropic dry etching. Smooth sidewalls were achieved by thermal oxidation and removal followed by another thermal oxidation for sacrificial layer growth. Afterward, 11-μm thick UNCD film was deposited by hot filament chemical vapor deposition (CVD) at Advanced Diamond Technologies, Inc. (Romeoville, IL). Then, 2 μm-thick plasma-enhanced CVD silicon dioxide was deposited at

350˚C to be used as a hard mask for UNCD etching. Following photolithography, silicon dioxide and UNCD were dry-etched sequentially using C_4F_8 and O_2 chemistries, respectively. The UNCD-only devices were soaked in buffered hydrofluoric acid (BHF) for 6 hours and released from Si substrate by dissolving SiO_2 sacrificial layer. Devices were carefully rinsed with deionized water to remove any residual HF. Planar UNCD devices were fabricated on a same wafer without etching Si trench. Si shuttles were fabricated from SOI wafers with adequate device layer thickness (15µm and 50µm) by Si DRIE and release in BHF. All shuttle device have same 29.5˚ of tip angle by sharing the mask sets.

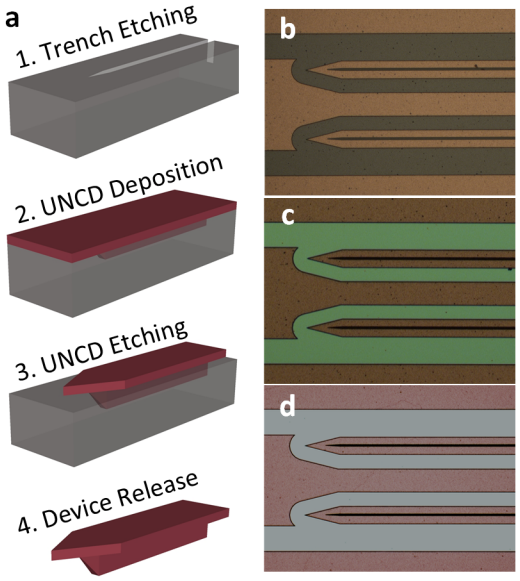

Figure 14. Process flow and pictures in the steps during fabrication. a, process flow of two mask fabrication. b, top view image after top oxide mask etching. c, top view image after UNCD etching, d, top view image after bottom oxide etching

Mechanical characterization

The most dominant mechanism of mechanical failure for insertion of a needle-shaped device is due to buckling. An insertion will end up with a failure when the buckling load is lower than the required insertion force. In this case, the shank keeps deflecting more without a load

increase and breaks eventually when the deflection-induced stress exceeds the fracture strength of the material. The characterization of buckling load was essential to analyze the results of insertion testing. Another goal of the buckling load measurement is the validation of the elastic modulus of UNCD and its structural design.

The initial setup for mechanical characterization was built using a precision load cell (Model 31, Honeywell, 50 g maximum), a digital multimeter (34011A, Agilent) and a motorized translation stage (MTS50-Z8, Thorlabs) **(Figure 15a)**. The silicon or UNCD shuttle was fixed to the end of load cell and the voltage output of the load cell was recorded through the ADC (225 samples per sec.) while the stage transfers the counterpart. The exerted force and travel distance were calculated by conversion of recorded data. The velocity and acceleration of the linear motor were 0.01 mm/s and 0.1 mm/s^2 respectively.

Buckling loads for 15μm-thick planar Si (Si-15), 50μm-thick planar Si (Si-50), 11μm-thick planar UNCD (P-UNCD) and T-shaped UNCD (T-UNCD) shanks were measured (**Figure 15**). The plateau in force-distance curve is the explicit indication of the occurrence of the buckling event. The buckling loads of Si-15 and Si-50 were measured as -8.4% and +11.3% of the calculated value (**Figure 15b**). The buckling load was calculated by equation,

$$P_{cr} = \frac{\pi^2 EI}{(KL)^2} \qquad \textit{Equation 2}$$

where E is Young's modulus, I is the moment of inertia, K is the effective length factor, and L is the length. The K value is dependent on the boundary condition and it is assumed as a fixed-pinned condition in which K=0.699 but as discussed later is not always true. For consistency, all shuttles were also 1.5-mm long unless otherwise stated.

The variation of thickness affects the buckling load significantly because the moment of inertia is proportional to the cubic of thickness. The range of UNCD's Young's modulus has been reported as 880-1000 GPa[63], [68], [69] and our estimated value based on our known geometry best fit to 800 GPa. The measured buckling load of P-UNCD was 2.3% lower than that of the calculation, and it implies that the estimation for Young's modulus is reasonable. The measurement of T-UNCD buckling load was 15.5% lower than the calculation and this is most likely due to the imperfection of the trench filling and the remaining void.

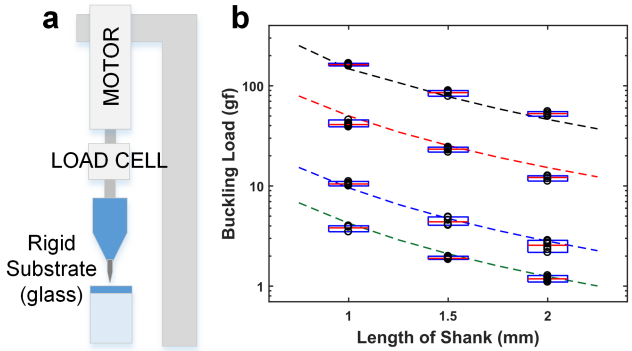

Figure 15. Buckling load characterization of various shuttles. a, Measurement setup with a load cell and a motor. b, Buckling load according to material, geometries and lengths, including two silicon geometries that are commercially available, N=7. Insertion speed was 0.01 mm/s in all cases.

Ex vivo and in vivo insertion test

In vitro insertion test with tissue phantom

Ex vivo tissue has a limited shelf life so many tests were conducted using a 100-µm thick PDMS sheet (Sylgard 184), to simulate dura and epinuerium, secured over a larger volume of agar gel. Our experiments showed that this phantom was stiffer than rat dura and almost as stiff as feline DRG epineurium (**Table 2**). Sylgard 184 (1-2 MPa)[70] and agar have similar moduli as dura[45] and parenchyma[71], [72]. The chisel-shaped tips for all variations of shuttles had identical angles and the thickness varied based on film thickness, which was chosen because it is

the standard tip of all Michigan-style probes. The measurement setup was identical to the setup for the buckling load measurement only except pushing a phantom instead of a rigid substrate (**Figure 16a**).

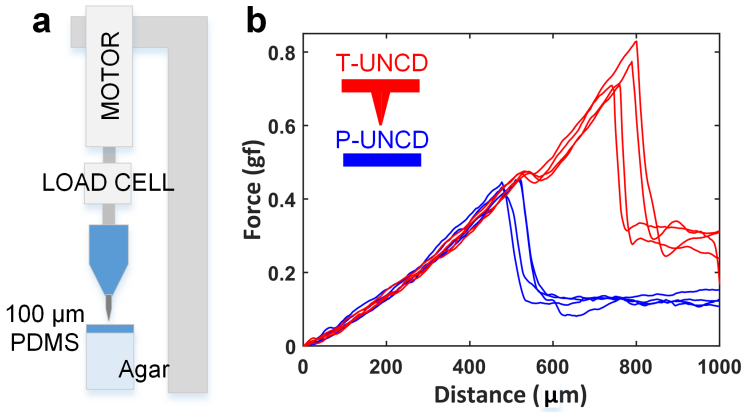

Figure 16. Measurement setup and force-distance curve for insertion through phantom. a, Measurement setup with a motor, a load cell and a tissue phantom with 100µm-thick PDMS. The phantom uses 100-µm thick layer of Sylgard 184 silicone (1-2 MPa, [70]) over 0.7% agar to represent a membrane and soft nervous tissue. b, Force-distance curve for P- UNCD and T-UNCD. T-UNCD showed two bumps, with the earlier one indicating the insertion of the planar tip. Insertion speed 0.01mm/s and acceleration 0.1mm/s^2.

A typical force response is an increasing force during the initial insertion until an abrupt drop indicating a puncture event. This force-distance pattern of one or more punctures in soft-tissue is well-documented[73]. It was expected that the thinner tip required less insertion force than thicker geometries as was actually observed (**Figure 17a**), though it was not linear. T-UNCD consistently showed multiple puncture events indicated by two force peaks. This corresponds to the tips of horizontal part and the vertical part of T-shape, respectively (**Figure 16b**). The first peak force occurred at the range of P-UNCD insertion forces (0.75 g) and the second occurred following a further increase of force. The average peak insertion force for this T-UNCD was 1.2 gf and was 8.7% higher than Si-15 (**Figure 17a**).

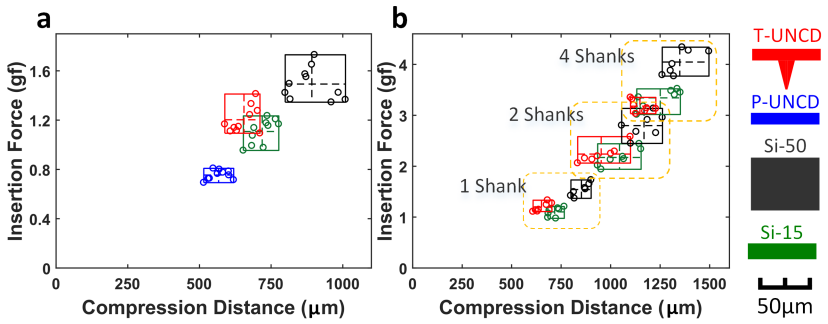

Figure 17. Mechanical characterization of various shuttles in a tissue phantom. a, Box plot results of insertion force of single shank shuttles, N=10. b, Box plot results of insertion force of 1, 2 and 4 shanks for three different probes, N=7 (planar diamond not tested). For 4-shanks, the force per shank was 0.8, 0.84, and 1.0 gf for T-UNCD, Si-15, and Si-50, respectively. The inter-shank spacing was 250 µm. Insertion speed was 0.01 mm/s in all cases.

The insertion force of 1, 2 and 4 shanks for each cohort were compared to investigate the behavior of multi-shank insertion (**Figure 17b**). Multiple shanks were 250 µm center-to-center from an adjacent shank. The force versus compression results, regardless of material and geometry, were less than a linear sum. Similarly, a three-dimensional assembly of six 4-shank UNCD arrays resulted in a decreasing force when normalized per shank (**Figure 18**).

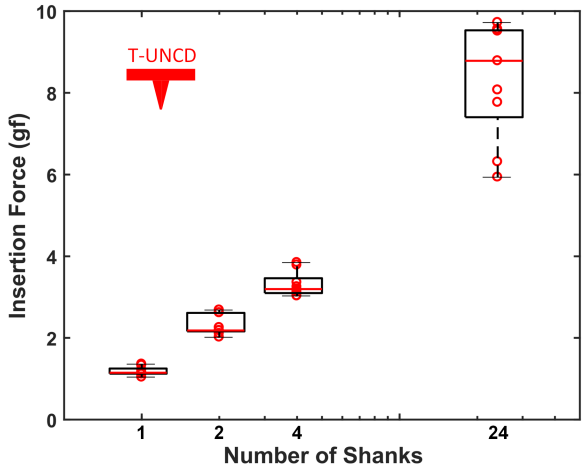

Figure 18. Phantom insertion force of 1,2,4 and 24 shanks for UNCD, N=7. To achieve 24 shanks, we arranged six 4-shank arrays in a hexagonal pattern. The force per shank in this case is 0.35 gf, a 66% and 72% force reduction relative to the 4-shank and 1-shank designs (Figure 3). This mechanism of local force reduction is yet unknown and may vary from shank to shank so more research on the local stress may help to reduce the size of a large number of shanks relative to the single shank version.

Ex vivo insertion test with explanted DRG

Ex vivo insertion tests with explanted feline L6, L7, and S1 DRG were conducted to evaluate the feasibility of epineurium penetration. The average insertion forces required for successful penetration of P-UNCD, Si-15, T-UNCD, and Si-50 were 1.15 ± 0.28, 0.96 ± 0.32, 1.92 ± 0.69 and 2.76 ± 0.61 gf, respectively (**Figure 19**). However, Si-15 had the most failures (9 failures in 15 trials) followed by P-UNCD (4 failures in 19 trials), with no failures observed for the other two geometries. Our results indicate that T-UNCD will penetrate the feline epineurium with 100% success like Si-50 but with only about half of the cross-sectional area (**Figure 19c**). P-UNCD and Si-15 will not reliably penetrate. In a qualitative *in vivo* test, the same T-UNCD design penetrated feline spinal cord (lumbar-sacral levels) nine times with zero failures where the dura is expected to be even thicker.

Throughout the *ex vivo* insertion tests with explanted feline DRG, many trials for Si-15 and P-UNCD resulted in failures (**Figure 19a and b**) even though this was not expected based on the standard assumption of a probe tip "pinned" to stationary tissue (**Figure 19d**). This commonly cited condition, where K = 0.699, may work for rodent brain implants but was incorrect for our *ex vivo* DRG experiments. Our results implied that the boundary condition at the contact between the tip and the tissue varied across trials presumably due to a varying angle of contact, the shape and curvature of the targeting tissue, and the friction of the tip at the surface. Also, that is a probable situation for *in vivo* insertion into peripheral nerve which will have similar variations. Adding to that risk is the breathing artifact observed in larger animal models. In these situations, the boundary condition is expected to be somewhere between fixed-guided where the tip is pinned sufficiently to the tissue but the tissue itself rotates or moves or fixed-free where the tip does not remain embedded in the surface and free to slip. This latter case

is most likely due to a large insertion angle, which is challenging to avoid on highly curved surfaces. Also, a duller tip will not pin as effectively as a sharp one. The *ex vivo* insertion results suggested that it would be safe and wise to design the mechanics of a shuttle based on the worst-case boundary condition, especially when inserted into the PNS. This means the structure should be 8X stiffer than one designed for the fixed-pinned condition.

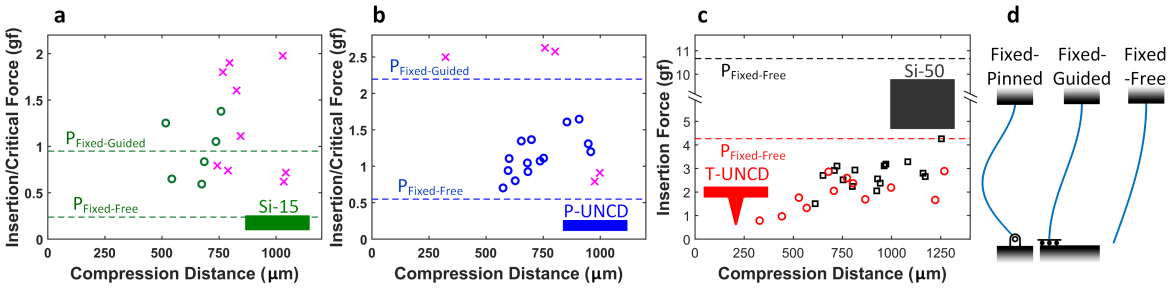

Figure 19. Result of ex-vivo insertions into cat DRG. a, 15µm-thick Si. "x" marks an insertion failure. b, 11µm-thick planar UNCD. c, T-shaped UNCD and 50µm-thick Si. d, Generic boundary conditions for the buckling load calculation (K=0.699, K=1, and K=2 respectively). The probe backend, at top, is fixed in each scenario and tissue is at the bottom. Theoretical limits noted as dashed lines in (a, b, c).

Table 2. Average peak insertion force

Needle	T-UNCD				Pulled pipette	
Tissue	Rat dura	Phantom	Cat DRG	Cat^{C} dura	Rat dura	Phantom
Force, g	0.68±0.22 N=6	1.2±0.1 N=10	1.9±0.7 N=6	1.4±0.2 N=2	0.40±0.03 N=2	1.7±0.2 N=8

Assembly with flexible electrode array

A flexible electrode array was fabricated broadly as we and others have described[74], [75]. One layer of 2.2 µm-thick polyimide (PI-2610 from HD Microsystems) was spin-coated on a sacrificial layer and fully cured at 350˚C. This thin, biostable PI is BPDA-PDA (3,3′,4,4′-biphenyltetracarboxilic dianhydride with p-phenylene diamine)[76]. This variety of polyimide

was chosen because of its high yield strength, flexibility, and low water absorption[77]. Metal patterning was formed in several steps depending on resolution requirements. 500-nm lines at 65-nm thickness were formed using a GCA stepper i-line lithography tool. This high resolution enabled 60 traces at a maximum width of 70 µm. Future work could also employ multi-layer metal. Wider and thicker metal was patterned using a Seuss MA-6 contact aligner over the interconnects and bond pads. A TiO_2 adhesion layer above and below metal traces was used to presumably improve adhesion, although not yet validated. The top PI-2010 layer was also 2.5-µm thick. The PI was etched by oxygen plasma to define the shape and open the electrical contact sites. Ti/Au electrode metal was patterned by a liftoff process and devices were released by the removal of the sacrificial layer. The electrode pitch was 40 µm. In order to decrease the impedance of the recording electrode sites, PEDOT-pTS was coated on Au electrodes as described elsewhere[78] (**Figure 20a**). The impedance in PBS was lowered to 24.0 ±1.45 kΩ from 1.98±0.752 MΩ of Au electrode (**Figure 20b**).

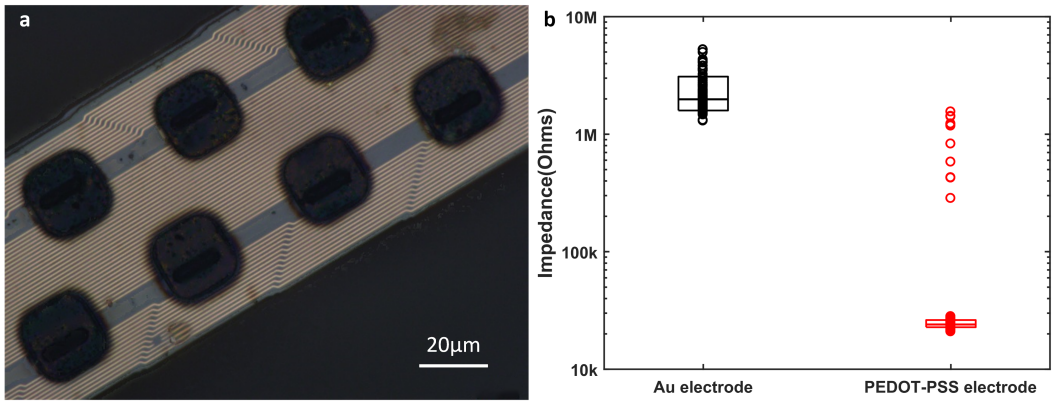

Figure 20. Picture and impedance of PEDOT:pTS coated electrodes. a, Poly(3,4-ethylenedioxythiophene: Sodium p-toluenesulfonate was plated on Au electrodes with a current of 690 nA and duration of 10 minutes as described in Patel, et. al 2016[78]. b, Impedances at 1kHz for non-coated Au electrodes and PEDOT-pTS coated electrodes, N=120. Top, middle and bottom lines of box plots indicates 90% value, harmonic mean, and 10% value, respectively. For the PEDOT-pTS coated electrodes, 14 electrodes with relatively high impedance were excluded as outliers.

The ultra-flexible electrode array was electrically assembled on a PCB and then mechanically assembled on a UNCD shuttle for *in vivo* insertion and recording. First, the PI arrays were ball bonded onto a printed circuit board[79] and the assembly was placed into a 3D-printed jacket designed to slide in the track of a shuttle jig (**Figure 21a**). Separately, a UNCD shuttle was aligned and mounted on a 3D-printed shuttle jig followed by dip coating into a beaker of PEG (12,000 MW) heated to 70-90°C (**Figure 21b**). The PI array assembly shown in **Figure 21c** was roughly aligned over the shuttle, aligning the vertical position by sliding the array assembly in its track on the jig. This position was then fixed to the shuttle backend by a small drop of PEG (4,000 MW). Precise self-alignment was achieved by once again dip-coating in heated PEG (12,000 MW). The resulting film was again 1 to 2 μm thick and transparent. This self-alignment achieved an accuracy of at least 5-μm.

Regarding the temporary adhesion of a polymer array onto the diamond shuttle, we describe our PEG mounting process below. The dissolution rate of PEG has to be carefully controlled so that the array doesn't separate prematurely during insertion and the dissolution and separation happens within a reasonable time after insertion. For cat DRG, this is not trivial because there are several hundred microns of relative DRG position shifting as the vertebral region is coupled to the body's movement during breathing. This movement is enough to either cause damage to the tissue or fracture the shuttle. We found that if the UNCD shuttle is removed within five minutes of insertion it did not break in three of three attempts. When left for longer, the shuttle fractured. Comparatively, a head-fixed rat surgery had no time limit and movement was hardly visible, although Gilletti et. al found this to be around 10-30 μm and varied with anesthesia[23]. We tested the molecular weight of PEG (4,000, 8,000, and 12,000 MW) and found the best result for our purposes to be dip coating with 12,000 MW. For rapid removal,

using the T-UNCD as a micropost is expected to be as effective as other microposts[35], [74] except it would also be stiffer and/or smaller. The thickness of PEG coated on a shuttle was below 5µm thickness and the alignment accuracy was < 3µm in the width direction.

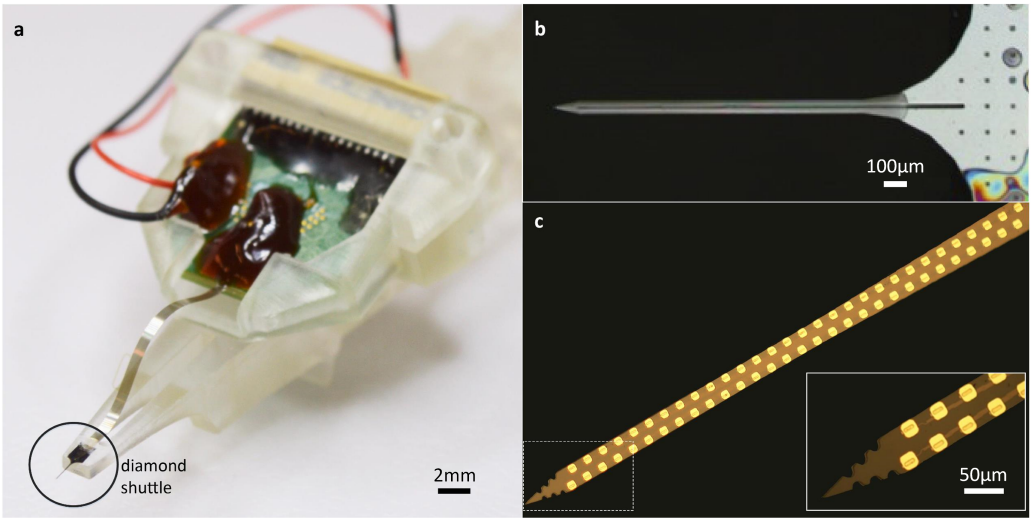

Figure 21. Assembly of high density flexible array mounted on UNCD shuttle. a, Photograph of entire assembly including the flexible polyimide array mounted on a UNCD shuttle. PCB is secured by a removable jacket that slides in a track of the shuttle jig. The insertion motor (not shown) is connected to the 3D printed shuttle jig. b, Top view of PEG-coated UNCD shuttle. c, Polyimide-based flexible array with 60 recording sites and (inset) zoomed view of the array tip.

In vivo experiment

Cat DRG

Procedures were performed in three adult, intact felines (male, 4.6-6.1 kg). Neural recordings were performed in two animals while only insertion testing was performed in a third. All steps were approved by the University of Michigan Institutional Animal Care and Use Committee (IACUC; protocol PRO00007296). As described elsewhere[75], felines were sedated with a ketamine-butorphanol-dexmedetomidine intramuscular dose prior to intubation and maintenance under isoflurane anesthesia (2-4%) with an intravenous saline drip (5-10 mL/kg/hr) and vitals monitored and maintained within normal ranges. A laminectomy was performed to expose the lumbosacral (~L7-S3) DRG. Bone screws were inserted into the iliac crests

bilaterally. The feline was placed into a custom testing stand[80] which supported the chest. Stainless steel wire was wrapped around each iliac crest bone screw and fixed to the stand, allowing for the lower abdomen and hind limbs to be suspended. This positioning reduced the relative motion due to breathing that would occur at the DRG. A jig holding a shuttle-mounted array was attached to a linear inserter (M-230.25, Physik Instrumente, Karlsruhe, Germany) mounted on a micromanipulator (KITE-R, World Precision Instruments, Sarasota, FL, USA), which was used to position the array just above a DRG (S1 or S2). The inserter was driven at a rate of 1.3 mm/s to insert the array and shuttle to a depth of 1.4 mm through the DRG. A variety of sensory stimuli were applied to activate sensory neurons, including brushing of different cutaneous dermatomes related to the DRG implanted (scrotum, anus, base of tail), infusion of saline into the bladder, and skin-surface electrical stimulation. Neural signals were sampled at 30 kHz with a Neural Interface Processor (Grapevine, Ripple, Salt Lake City, Utah, USA). After an experiment neural signals were first sorted in Offline Sorter (Plexon, Dallas, TX, USA) prior to analysis with custom scripts in MATLAB (Mathworks, Nantick, MA, USA).

The T-UNCD shuttle was inserted into the S1 or S2 DRG of three separate felines at 1.3 mm/s without oscillation. One animal had mechanical testing performed, which also included successful shuttle penetrations through the spinal cord dura (Table 1). In the other two animals, functional arrays successfully recorded neural activity. Evoked activity was recorded from a variety of stimulus types across the span of the array, including cutaneous neurons from unique locations in the perineal region and base of the tail (**Figure 22**). In the first animal experiment during six sensory input trials, a total of 28 different channels had a unit out of 42 functional channels, spanning 1 mm in depth across the array. We observed 7 putative units on subsets of these 28 channels, which were overlapping due to the closeness of the electrodes (40-μm pitch).

The average per trial was 11 units across 8 channels with single unit amplitudes between 35-323 μV peak-to-peak (mean 68 μVp-p, median 47 μVp-p).

In the second animal experiment, we observed approximately 40 putative units out of 48 channels spanning 1.06 mm in depth when the probe was in a fixed position. When the same probe was retracted, neural activity was observed on all 59 functional channels, including one putative bladder afferent (not shown). An average of 78 units across 32 channels were observed during each of eight evoked trials during testing with the electrode in a fixed position, with single unit amplitudes between 39-1313 μV peak-to-peak (mean 123 μVp-p, median 80 μVp-p). Across multiple trials in this fixed position, a total of 48 different channels had a unit (167 non-unique units observed) out of 59 functional channels, spanning 1.06 mm in depth. When this same probe was retracted, units clearly moved between electrodes, including appearing on electrodes that were deeper in the tissue, suggesting that the tip of the array may have initially been in an inactive region of the DRG or in the ventral root (**Figure 22a**). During movement of the probe, a total of 249 units were identified, with all 59 functional channels having activity across the full 1.2 mm span. Single units during the probe movement trial were within 50-1273 μV peak-to-peak (mean 199 μVp-p, median 125 μVp-p).

As the channels within the electrode array were separated by 40 μm, some units appear on multiple channels and we used careful manual sorting followed by comparison of waveform shapes across neighboring channels to report putative units. High-density arrays, like that used here, are best employed using an unbiased polytrode analysis as others have demonstrated[16], [81], [82] to eliminate double counts but also to increase the number of unique identifiable units when performing an in-depth mapping study[1].

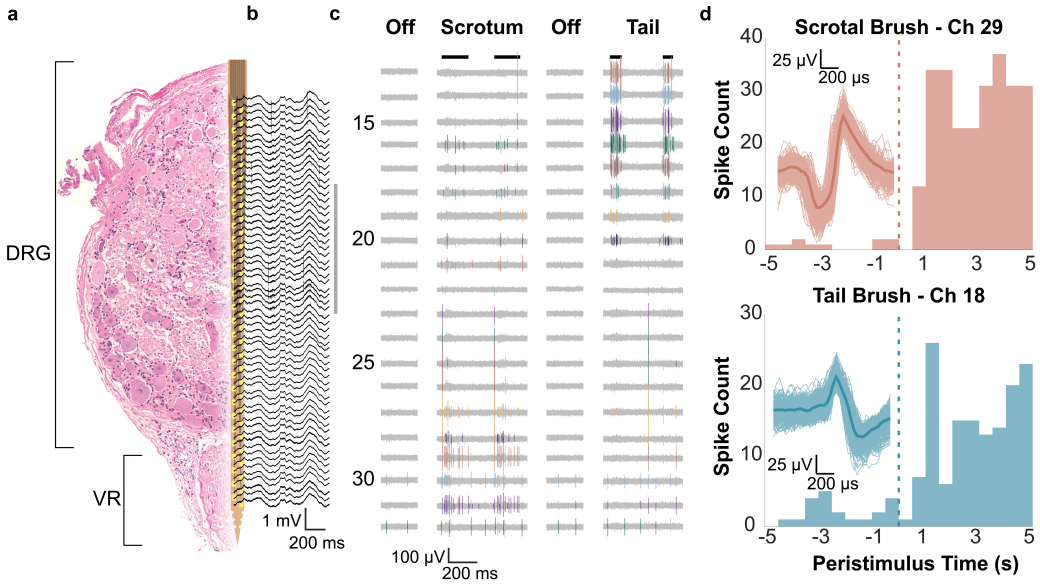

Figure 22. Recorded neural signals from feline sacral DRG for evoked stimuli. a, Diagram of the array in DRG. On the left is a representative hematoxylin and eosin stained cross-section of an example DRG with the ventral root (VR) below. Overlaid is a CAD diagram of the array, with array sites in yellow. The array and DRG are to scale. b, Wideband signal (highpass filter with 2 Hz cutoff) recorded during scrotum brushing. c, High pass filtered signals recorded during two sensory input trials (scrotum and tail brush strokes indicated by black lines at top). Channels shown are indicated by the gray vertical line to the right of (b). Manually sorted single units are in color. d, Peri-stimulus time histograms (PSTHs) for two channels and trial types, labeled and colored by channel numbers shown in (c). For both units shown, brushing starts at 0 s and continues through 5 s, including multiple individual strokes. Overlaid on each PSTH are the corresponding spike waveforms, with the mean waveform given as a dark thick line of the same color.

Rat dura

The experiment was approved by the Institutional Animal Care and Use Committee at the University of Michigan (protocol number: PRO00007275). Two male wistar rats (600 g) were implanted with a UNCD-polyimide electrode under isoflurane anesthesia (1.2 – 1.5%). No prior experimentation had been performed on this rat. Atropine (0.05 mg/kg, s.c.) was administered after anesthesia induction to reduce saliva production, and the rectal temperature was monitored and kept constant at 36–37 °C with a DC temperature controller (TCAT-LV; Physitemp, Clifton, NJ, USA). Proper depth of anesthesia was maintained by confirming the lack of nociceptive reflex. A craniotomy was drilled (4 by 4 mm), carefully paying attention to not damage the dura mater. The hole was cleaned and filled with sterile saline solution (0.9%, MWI, USA) and kept

wet until the custom-electrode was implanted at 1 mm posterior from bregma and 2.8 mm lateral of the midline, in the S1FL area of the somatosensory cortex.

The electrode was inserted to a 1.5 mm depth in the cortex. In one of the rats, the separation process was initiated by applying sterile saline on the array ten minutes after insertion. Once the upper part of the polyimide was separated the UNCD shuttle was slowly moved (50 μm up and down) until a complete separation was visible under microscope. Then, the shuttle was retracted while the recording electrode was kept in place.

We inserted the T-UNCD shuttle into the motor cortex through dura mater at 0.01 mm/s without fracture or failure. The depth of insertion was 1.5 mm and the compression was 642 μm. Separately, we also inserted the T-UNCD – polymer device through dura mater of anesthetized rats (2 insertions in each of 2 rats) also without failure. The flexible electrode was attached to the T-UNCD in the same way as in the feline surgery. The separation process was initiated by applying sterile saline on the array ten minutes after insertion. Once the upper part of the polyimide was separated the UNCD shuttle was slowly moved (50 μm up and down) until a complete separation was visible under microscope. Then, the shuttle was retracted while the recording electrode was kept in place (**Figure 23**). Then, wideband (0.3 Hz – 3000 Hz) and single unit neuronal activity were recorded from the somatosensory cortex of the rat (N=1, Supp. Fig. 9a and b). The spontaneous neuronal activity was recorded for 30 minutes and 20 putative single units were found (**Figure 24**). The recorded signals (n = 60 channels) were amplified (200X gain) and stored after digitization at 20 kHz sampling rate per channel (RHD2132 and RHD2000 Evaluation System, Intan Technologies, Los Angeles, CA).

The recorded data were analyzed by custom-written scripts in MATLAB (MathWorks, USA). Neuronal spikes were detected from the digitally high-pass filtered signals (0.5–3 kHz) by

Spikedetekt2 (https://github.com/klusta-team/spikedetekt2). Detected spikes were automatically sorted using KlustaKwik2[83], followed by manual adjustment of the clusters using KlustaViewa software[81] to get well-isolated single units (multi-unit and noise clusters were discarded).

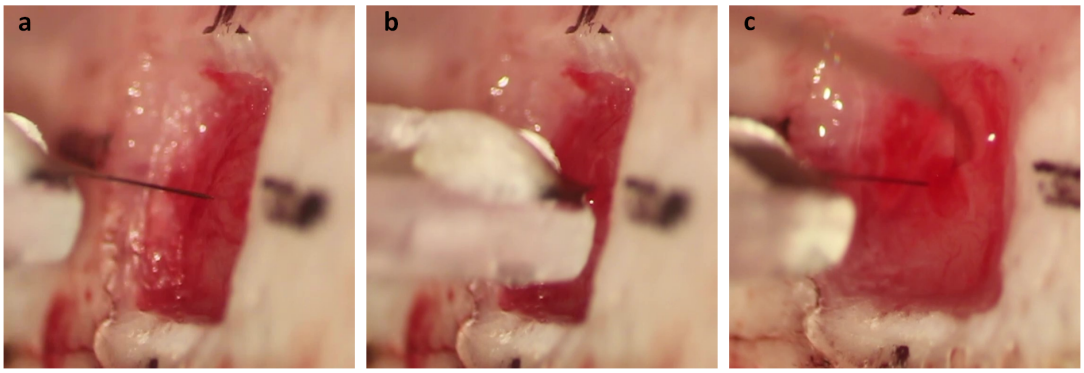

Figure 23. Captured images during in vivo insertion on a rat brain. a, a flexible array on a UNCD shuttle before insertion. b, completed insertion with both the flexible array and the shuttle inside the brain. c, successful retraction of the shuttle leaving the flexible array inside the brain.

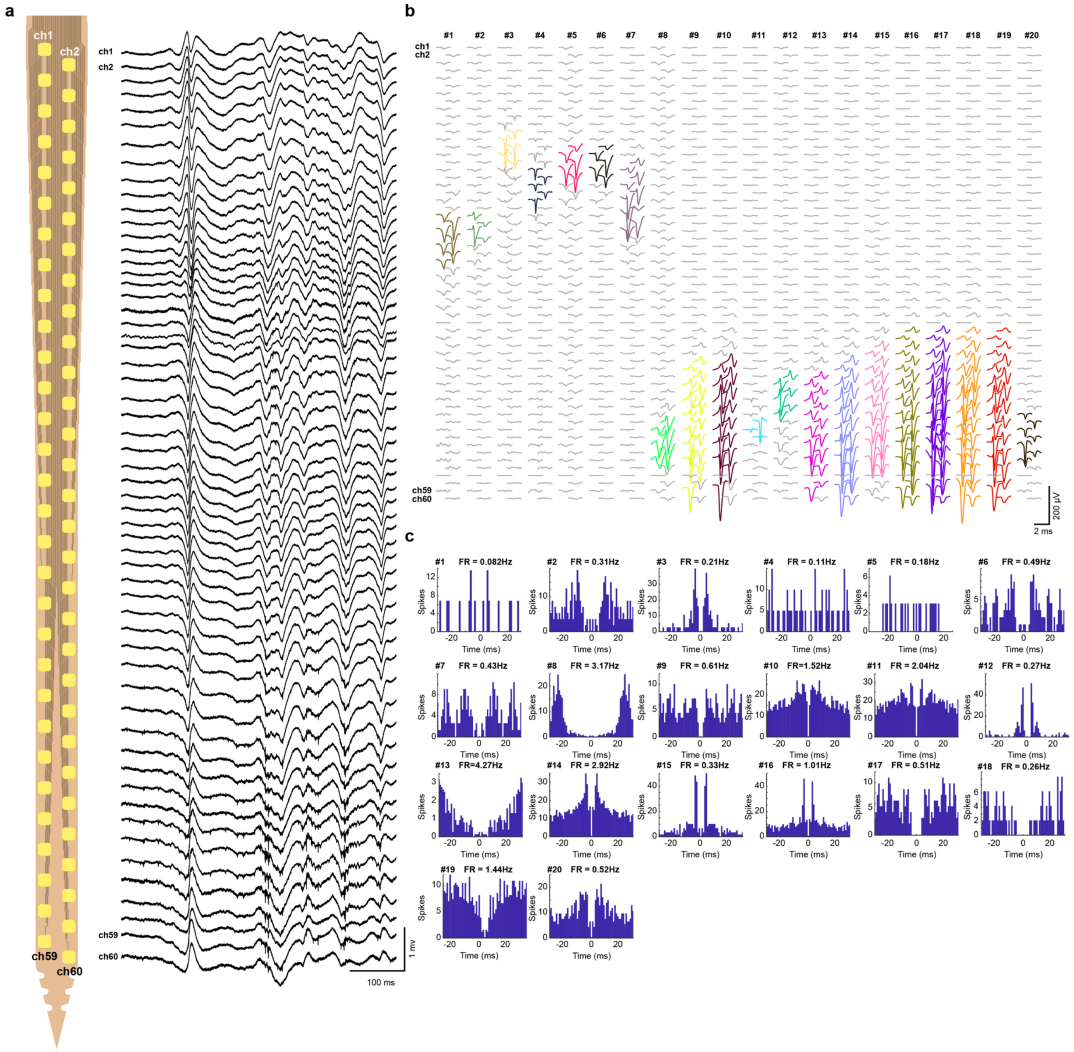

Figure 24. Recorded neural signal from somatosensory cortex of rat. a, Wide-band (0.3 – 3000 Hz) spiking activity recorded on a flexible electrode from S1FL region of an anesthetized rat (right) and a schematic of the probe sites (left). Note the spiking activity at the bottom of the shank. b, Recording of high number of well-isolated single units. The spiking data was quantified for 20 putative single units recorded simultaneously from S1FL (same animal and session as in a). Plots show average single-unit triggered waveforms (n = number of spikes, at least 500) on all channels. Note the single unit activity is present across multiple channels but the larger than expected range is due to the movement of probe relative to the brain tissue over the course of 30 minutes. c, Auto-correlation histograms of the 20 putative single units (same as b). Mean firing rate (FR) value is shown for each unit above the histogram.

Discussions

We demonstrated that in rat and feline models of dura and thick epineurium, our novel T-beam UNCD shuttle could deliver a thin, flexible high-density microelectrode array that would be especially useful in neural mapping studies. The reduced-footprint with high stiffness features of the shuttle exhibited better insertion features in tissue analogues and *ex vivo* neural tissue than

standard probes. There are also many design opportunities for thicker or thinner UNCD shuttles whose thickness, including the vertical support, can be in the range of 5 to 52 μm, which is potentially translated into the range of buckling load up to 102 gf. As we demonstrate in our results, important considerations like the boundary condition of a buckling model are especially important in the periphery. We also compare this shuttle approach to others.

Mounting a polymer array on the shuttle and the separation after insertion is an important, practical issue for a successful *in vivo* experiment. Fortunately, a planar polymer array will self-align on a planar shuttle due to geometrical similarity and surface tension when dipped in a solution of water or polyethylene glycol. This may be a simpler approach than using a cylinder-shaped shuttle, e.g. tungsten wire or carbon wire[35], [74] where the fabrication is expensive and does not scale to multi-shank devices. Also the resulting cross-section is a rectangle tangent to a circle and thus creating more damage than either alone. T-UNCD has the advantages of both stiffness and a matching geometry for the high-density polymer arrays used here and by other groups[37], [58], [59]. Also, compared to the stylet approach, the planar shuttle is more appropriate to deliver multi-shank electrodes readily enabling higher channel count. Furthermore the T-UNCD forms a sharp tip that is effectively notched to create a micropost. Luan et. al demonstrated the micropost but this version required focused ion beam etching which is slow and costly compared to large-scale microfabrication. Nonetheless the micropost concept is advantageous if the immediate release of a device is critical in an application and the potential of bending the polymer tip is not a concern. Future work may use the T-UNCD as a micropost in order to speed the release after insertion in feline DRG experiments where breathing movement was significant. In the above acute recording demonstration, the shuttle remained for almost an hour at a time and in each case the shuttle was broken from breathing movements. When the

shuttle was removed within 5 minutes of implant, the shuttle was intact, but releasing the biosensor array within 5 minutes using polyethylene glycol was not possible in our experience. Thus the micropost approach with the UNCD would be ideal for chronic recordings in large animals with significant tissue movement.

We believe that T-UNCD is superior to other shuttles even when a large insertion force is not required (e.g., when dura mater is removed). Assuming 6mm length of a shank, buckling loads of T-UNCD SMALL and Si-15 are estimated as 0.19 gf and 0.16 gf, and the former reduces the blood vessel damage to 24% of the latter (**Figure 10**). T-UNCD SMALL has 37% less cross-sectional area than 20μm-diameter tungsten wire which has an estimated buckling load of 0.18gf.

Conclusion

High-density bioelectronics for the nervous system have a long way to progress before we achieve biomimetic scale, equivalent tissue mechanics, and effectively no tissue-reactivity but the modeling and materials work shown here is an important step in that direction. The results presented here demonstrate the flexible polymer array inserted through the toughest nervous system tissues to obtain neural signals. We have developed a versatile T-shaped ultra-nano-crystalline diamond shuttle which provides a 56% reduction in cross-sectional area compared to a planar silicon shuttle with equivalent insertion strength, and still stiff enough to insert into different neural structures in small and medium animal models with the dura and epineurium intact. This same structure will theoretically reduce micro-vascular damage by 37% compared to standard probes. More broadly, the use and deployment of advanced bioelectronics as developed here is critical for high-resolution scientific research into the nervous system and will contribute to future clinical devices in the treatment of neurological damage and disorders.

Chapter 3.
High Density, Flexible Array with Low Impedance Site and Long Term Reliability

Introduction

Implantable neural probe takes a key role of monitoring the activities of individual neurons with a great temporal/spatial resolution. It is an important tool for the neuroscientists to deeply understand the brain functional map and eventually it promises clinical treatment of a variety of neurological disorders. However, the signal quality generally degrades over time after insertion. It is widely believed that the main cause of the degradation of recording functionality is the foreign body reaction, and the implanted shank induces a glial scar formation and a loss of neuron cell nearby. The sustained immune response leads to diminishing of the signal-to-noise ratio since the glial encapsulation sheath increases the impedance of recording site and also the distance from the electrode to the nearest viable neuron cell increases. The main hypothesis is that the relative displacement due to the brain micromotions by respiration, vascular pulsatility, and head movements induces the mechanical stress and strain to the tissue around the implant and it is the most responsible factor for the tissue reaction[26].

In this sense, the compliance of the probe shank is considered as an important designing factor for the long-term recording in that a more compliant device expect to induce less tissue response. However, the shank also has to be stiff enough to penetrate the tissue for insertion without buckling. Both the compliance and buckling load of geometry are functions of EI where E is Young's modulus of material and I is the moment of inertia dependent on the dimensions, and those are in inverse proportion to each other. A fast emerging approach is the flexible

electrode array implanted with the aid of insertion tool such as shuttle or stylet. In this approach, the probe compliance can increase by shrinking the dimensions without considering buckling until other constraints (the width to accommodate desirable number of channel, the easiness of handling according to the thickness, etc.) arise.

To date, the most dominant materials for the flexible neural probe are parylene-C and polyimide. Both polyimide and parylene-C have a plenty of suitable properties for neural implants in terms of flexibility, insulation, and biocompatibility. Furthermore, those can be fabricated by micromachining process along with keeping thinness. A significant advantage of Parylene-C over polyimide is that Parylene-C is a US Food and Drugs Administration (USP class VI) approved material. However, Parylene-C presents critical drawbacks regarding the chronic use. Yasuda et al reported that Parylene-C has an inherent problem as an insulation layer for long-term use due to the breakdown of bulk phase by the salt intrusion[84]. Moreover, thickness of Parylene-C based device cannot be less than 7μm because it would otherwise be impractical to handle due to stress induced curling[85].

Among various types of Polyimide, "BPDA-PDA type of polyimide looks to be most suitable for in vivo applications, as it is the least polar of all the polyimides, with the consequence of having the lowest water uptake of only 0.045%. This leads to reduced plasticization 89 of the material during application in the body and to a much lower volume (and as a consequence stress) increase in the device"[77]. Besides, the intrinsic film stress of BPDA-PDA polyimide is reported as only 2MPa and it is empirically proved that 4μm-thick BPDA-PDA polyimide array presented no issue with handling and no critical curling due to film stress.

A significant challenge in polyimide based neural probe is the poor adhesion and the long-term reliability[77]. Polyimide is an inert material and it is a great advantage as an

insulation layer. But it generally results in the poor adhesion, especially with metals. The poor adhesion induces the failures with traces and electrodes, and affects the long-term stability. Another challenge, not only for polyimide array but also for general neural probe is the reduction of the electrode impedance to achieve high SNR. PEDOT-PSS and Pt-bk are the most successful materials for lowering the impedance up to date[10], [78], [86], [87]. However, the structural stability and the long-term reliability of those porous materials is not fully addressed yet. Also, those methods have to be done by a tedious electrode-level procedure. There is need for a method for reliable low impedance electrode by high throughput process, i.e. wafer-level process. In this work, the aim was to develop a polyimide based flexible neural probe with enhanced long-term reliability and low impedance recording site by wafer-level process.

Design

The probe design and layout is shown in **Figure 25**. The electrode configuration was designed as a polytrode with three rows and 20μm inter-electrode distance. Each shank had 64 electrodes spanning 420μm and the size of the electrodes was 193μm^2. The maximum width of the shank was 84.5μm and the width became narrow down to 60μm at about 220μm from the tip. The length of the implantable shank was 6mm and the length of the cable part was 20mm. The backend had two rows of 104μm-pitched bonding pads for ball bumping, known as microflex interconnect (MFI)[79].

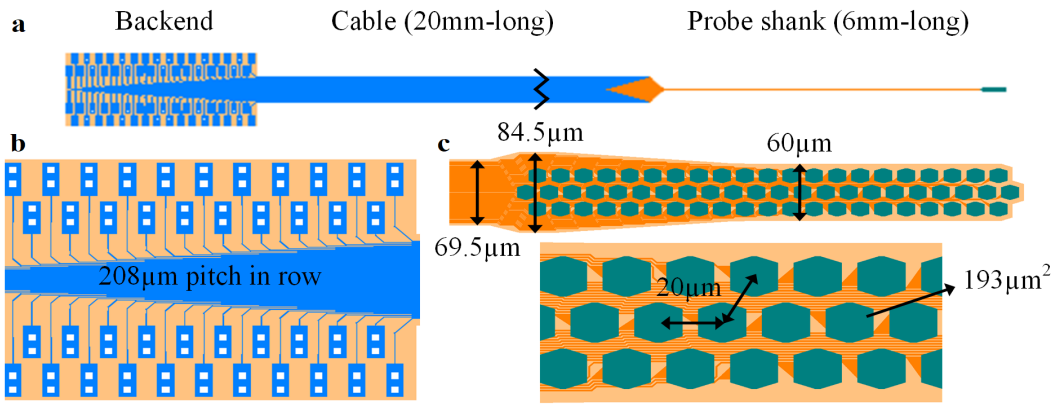

Figure 25. Schematic of the probe design and electrode configuration. a, flexible probe design including probe shank, cable and backend. b, backend for ball bumping with 208µm-pitched, staggered pads (effective pitch 104µm). c, design of shank and 64 channel electrode.

Fabrication

The fabrication process is illustrated in **Figure 26**. The process began with 525µm-thick Si wafer with Cr/Au/Cr (100/500/500Å) sacrificial layer. This sacrificial layer has been steadily used utilizing abnormally fast undercutting of gold film on chrome due to the formation of electrochemical cell. BPDA-PDA type polyimide (PI-2610, HD microsystems) was selected as the material for flexible probe due to its desirable properties such as low film stress and low moisture uptake[77]. The bottom polyimide (~2µm) was spun on the wafer and fully cured at 350˚C for 30 minutes. Following oxygen plasma to increase adhesion, 10Å of Titanium was deposited by sputtering. The Titanium layer was turned into Titanium oxide by another oxygen plasma and this is a critical step to increase the adhesion between polyimide and metal stack on it. I will discuss more details on the adhesion improvement later in this chapter. Then, reactive-sputtered Titanium oxide was deposited. PR patterning with 0.5µm of critical feature was done with the aid of a 365nm i-line stepper (AS200, GCA) and Pt/Au/Pt (100/400/100Å) was deposited by e-beam evaporator and patterned by liftoff. Another liftoff process patterned Pt/Au/Pt (250/2,500/250Å) with larger feature size followed by reactive sputtering of TiOx to

fully cover the metal stacks to improve the adhesion of polyimide on metal. The top polyimide layer (~1.8μm) was spun and fully cured as the bottom polyimide layer. Polyimide was etched to define the devices and to form contact openings with TiO_2 as a masking layer. Double layer of Liftoff Resist (LOR) and PR was patterned for the formation of the electrodes. A wafer-level polyimide roughening process was followed by 900Å Pt sputtering and liftoff in remover PG. The details of the roughening process will be described in the following section. Finally, the wafer was soaked in Cr etchant for more than 4 hours to release the polyimide probes.

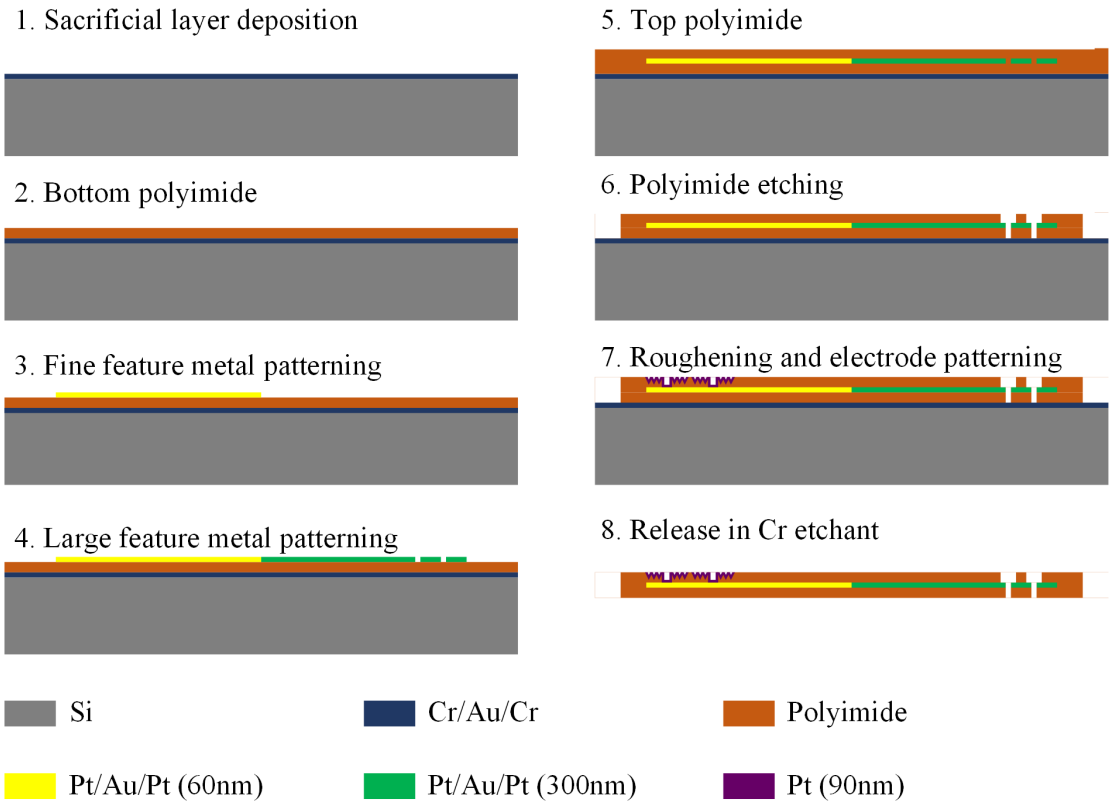

Figure 26. Process flow of polyimide-based neural probe with roughened electrodes.

In order to pattern submicron feature of metal with 0.5μm line and 0.5μm space, a liftoff process was conducted using a double layered resists with 200nm-thick Polymethylglutarimide (PMGI; SF-5S, MicroChem) and 600nm-thick PR. Also, 400nm-thick contrast enhancement

material (CEM; CEM-365iS, microSi) was used to extend the resolution limit of the optical lithography system. CEM is a photo bleachable material, which is opaque to the exposure wavelength and becomes almost transparent on exposure. It is bleached faster at higher intensity so it is possible to completely expose the underlying photoresist by adjusting the bleaching dynamics properly. Since the thickness of undercut layer (PMGI) was 200nm, the metal thickness that could be patterned by liftoff was limited to 60nm. 0.5μm-wide and 0.5μm-space metal traces (Pt/Au/Pt) with 60nm thickness and more than 5mm of length were successfully fabricated with reasonably high yield as shown in **Figure 27**.

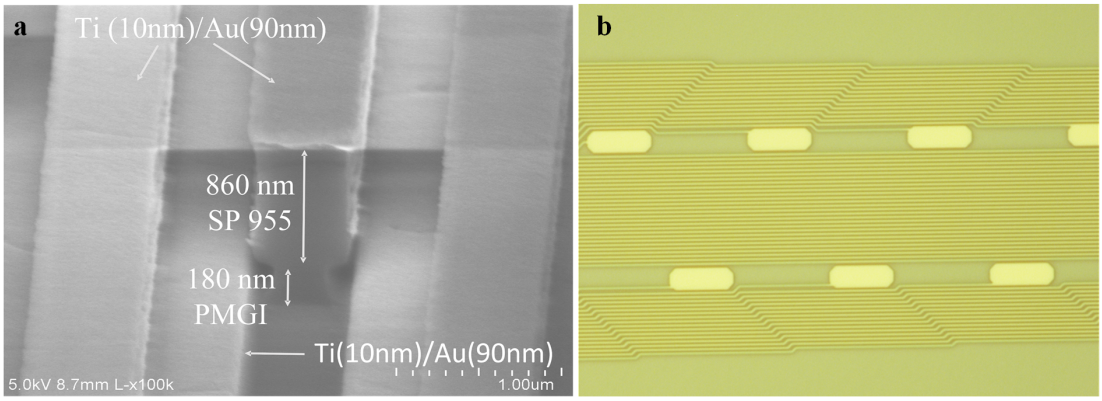

Figure 27. Submicron metal patterning. a, SEM image with Ti/Au deposited on PMGI/PR double layer. b, microscopic image of submicron metal traces patterned on polyimide.

A hard mask is required for polyimide etching due to its oxygen plasma chemistry. Aluminum has been used for the masking material for the previous works ([88]) but Aluminum induced roughened and unclear opening due to re-sputtering during etching process with oxygen plasma. Instead, TiO_2 was used as a masking layer to achieve cleanness of contact opening for recording site and bonding pad. The etched surface was clean and smooth.

Roughened-Pt (R-Pt) electrode

Electrodes with a small geometric area afford greater spatial resolution and tetrode-like redundancy, which improves spike sorting accuracy[1], [81], [89], [90]. This constrains our geometric space and therefore requires high-surface area modification techniques ([10], [61], [78], [91]) but lowers impedance and improves the signal-to-noise ratio (SNR). However, the longevity of the lowered impedance is still disputable mainly due to poor adhesion of functional material and/or fragility of nano-structured electrode. More importantly, most of the impedance reduction methods were device-level process, which is relatively low throughput and becoming more time-consuming and tedious as the channel count rises rapidly for large-scale recording. Paik et al. reported wafer-level impedance lowering process using a polysilicon roughening technique[92]. In this study, they showed that the polysilicon layer on top of a highly doped glass formed a highly roughened surface due to nucleation inhibition. Unfortunately, this process is not applicable to polymer based fabrication processes. A novel wafer-level roughening process for impedance reduction (down to ~350 kΩ at 1 kHz) on a polyimide substrate was developed utilizing an atomic self-patterning technique. The polymer substrate was roughened instead of the electrode material using a simple wafer-level process that is based on the fact that angstrom-thick metal films nucleate on the surface and sufficiently mask the polymer. It increased the effective contact area between the substrate and the electrode, and in turn the adhesion strength also improved.

The fabrication process for the roughened Pt (R-Pt) electrode is described in **Figure 28**. First, ~10Å of Ti was deposited on the wafer with patterned PR for electrode metal liftoff. Then, the area on PR and top polyimide uncovered by Ti was etched by oxygen plasma with low plasma density and it formed the roughened surface due to high selectivity and undercutting.

Throughout this roughening process, we could etch ~200-nm deep trenches with ~100-nm wide features. Roughened Pt electrode shown in **Figure 29** was patterned by the liftoff process. The impedance spectrum was measured in phosphate buffered saline (PBS) solution between 200Hz and 5kHz using nanoZ impedance tester (Plexon Inc.). The measured impedance of the electrodes with 193μm^2 of projected area was 347.6 kΩ at 1 kHz in average over 101 electrodes, which is 3X reduction from 1.055MΩ of plain Pt electrode impedance with identical area (Figure 3-5b). The impedance of the plain Pt electrode agreed with the normalized value from the previously reported results[93], [94], [95].

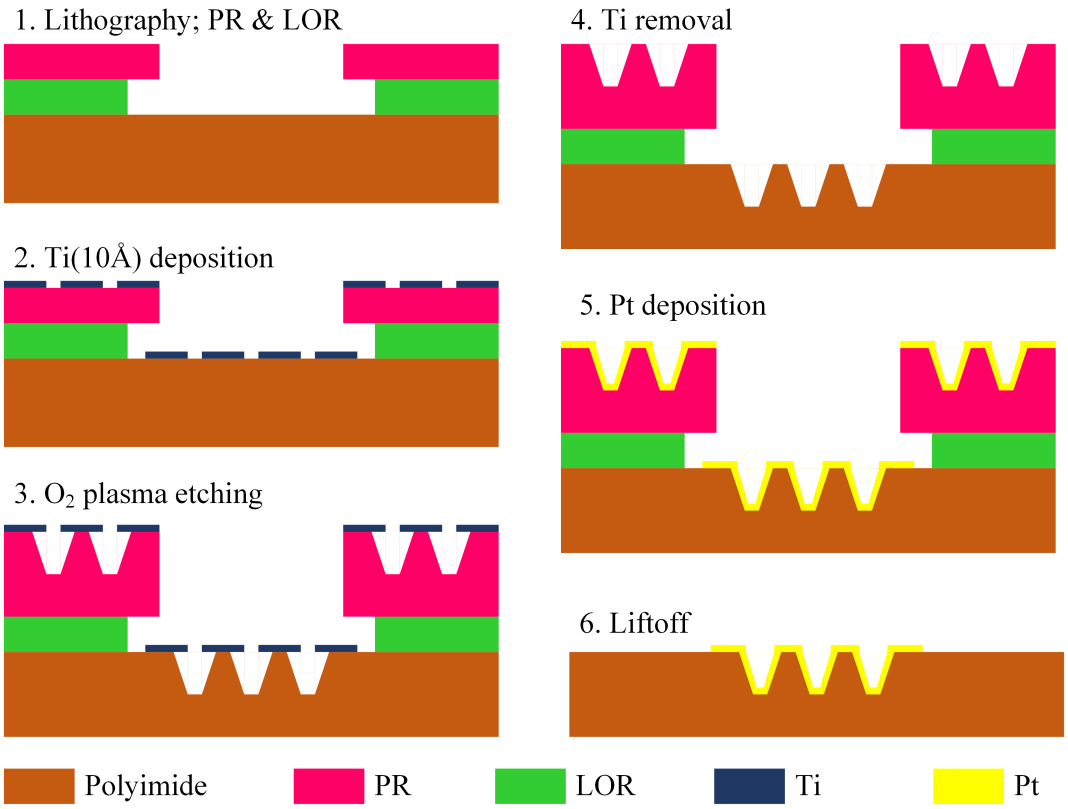

Figure 28. Process details on PI roughening and electrode patterning.

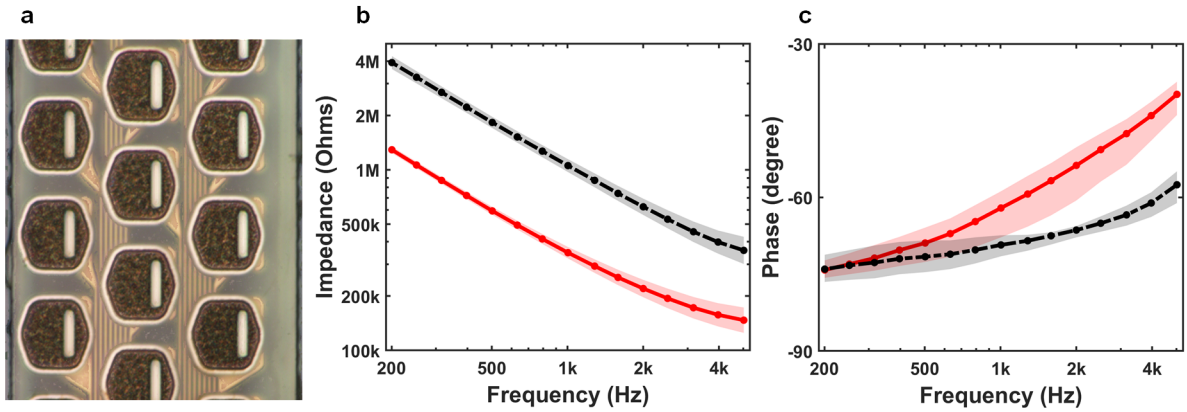

Figure 29. R-Pt electrode and plain-Pt electrode. a, Microscopic picture of roughened Pt electrodes with 193 µm2 on a released polyimide-based array. Long smooth oval is contact pad between surface and trace only 2-µm wide. Traces are 0.5 µm wide with 0.5 µm gap. b, Measured impedance of roughened Pt electrodes (red, N=101) and plain Pt electrodes(black, N=81) showed 347.6 kΩ and 1.055MΩ in average at 1 kHz, respectively. c, Measured phase. Shaded areas indicate ±1σ variation (68%).

Metal-PI adhesion improvement

Polyimide is the most prevailing material for flexible bioelectronics due to its superior properties and chemical inertness. The lifetime of neural implants is becoming more important along with the trend towards chronic monitoring over several months to years. Major causes of neural implant failure are the failure of encapsulation layer such as material degradation, delamination and expansion of pinholes, and the adhesion loss of interconnect conductor from the substrate. Polyimide is a material with high chemical stability and low reactivity. It was reported that polyimide minimally degrades in PBS[76]. This feature makes polyimide a reliable substrate for insulation but also week adhesion with metals. Early research on adhesion of metal on polyimide proved that Ti and Cr forms covalent bondings when deposited on polyimide[96], [97]. However, in wet and ionic environment of in vivo experiment, adhesion loss and delamination of metal from polyimide has continued to be a problem. Moreover, the adhesion issue is becoming more problematic while the width of interconnects shrinks for higher electrode density. Here, I proposed a novel adhesive layer and metal stack to improve the adhesion between metal and polyimide so as to increase lifetime of the implantable device.

There are three interfaces in the conventional polyimide-based electrode array with metal interconnect sandwiched by two polyimide layers as shown in **Figure 30**. It is known that the adhesion in polyimide-to-polyimide interface is relatively stronger than other two metal-to-polyimide interfaces but a trace will be eventually failed by formation of an electrical pathway through polyimide-to-polyimide interface. Therefore, all three interfaces potentially take roles in the failure mechanism.

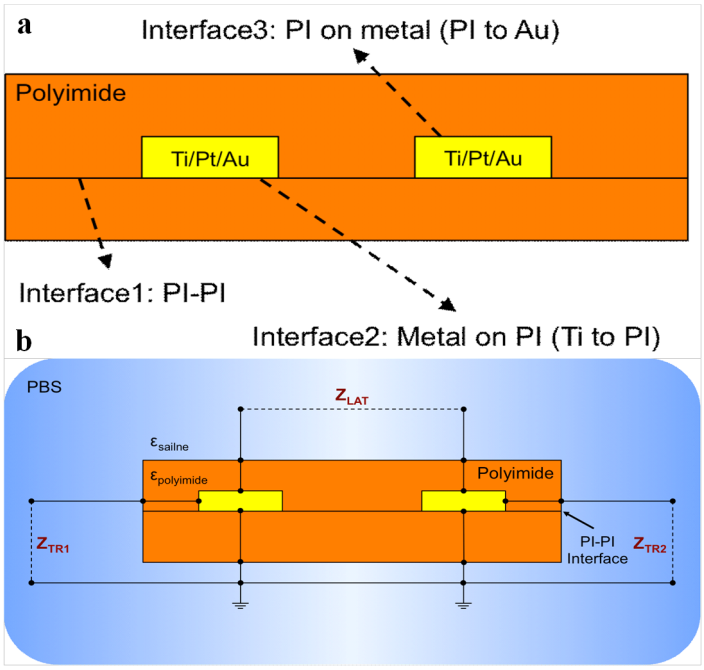

Figure 30. Interfaces in a conventional polyimide-based electrode array. a, three interfaces between two PI layers and sandwiched metal; PI-PI, Metal-on-PI, and PI-on-Metal. b, three measurements using IDE; lateral impedance between two channels, two of transverse impedance between the channels and the surrounding PBS solution.

Girardeaux et al. reported that the formation of TiO_2 during Ti deposition significantly reduced the adhesion to polyimide by interfering the formation of covalent bonding between Ti and polyimide[96], [97]. Also, Miyauchi et al. suggested that the failure mechanism of Cr-polyimide bonding is related to the oxidation of Cr due to oxygen diffusion and formation of CrO_x[98]. The previous studies implied that fully oxidized layer with covalent bonding with polyimide would greatly increase the reliability of the interface.

Here, we introduced oxidized Ti formed by thin Ti layer deposition and following oxygen plasma to oxidize it as a reliable adhesive layer. As mentioned earlier, the deposited Ti would generate covalent bonding with polyimide and it would be fully oxidized by oxygen plasma if the thickness were carefully controlled so there happens no more oxidation that induces adhesion failure. **Figure 31** showed the result of the adhesion test of metal-on-polyimide. The samples with different adhesion layer/metal stack on polyimide were prepared and the adhesion was assessed by tape testing after soaking in 87˚C saline for 32X acceleration compared to 37˚C saline. Ti/Pt/Au is selected as a control since it is the most conventional metal stack being used in MEMS devices. Au on oxidized Ti showed almost no delamination after 6 days soaking and few local delamination after 12 days soaking in 87˚C saline, which are equivalent to 6 months and 1 year soaking in 37˚C saline, respectively, while the conventional stack with Ti/Pt/Au showed massive delamination after 6 days and even complete delamination after 12 days. Interestingly, oxidized Ti/Ti/Pt/Au layer failed much earlier (6days soaking) and it apparently supports the hypothesized failure mechanism by oxidation since oxidized Ti/Ti layer is not fully oxidized and should have more probability to be oxidized by oxygen diffusion.

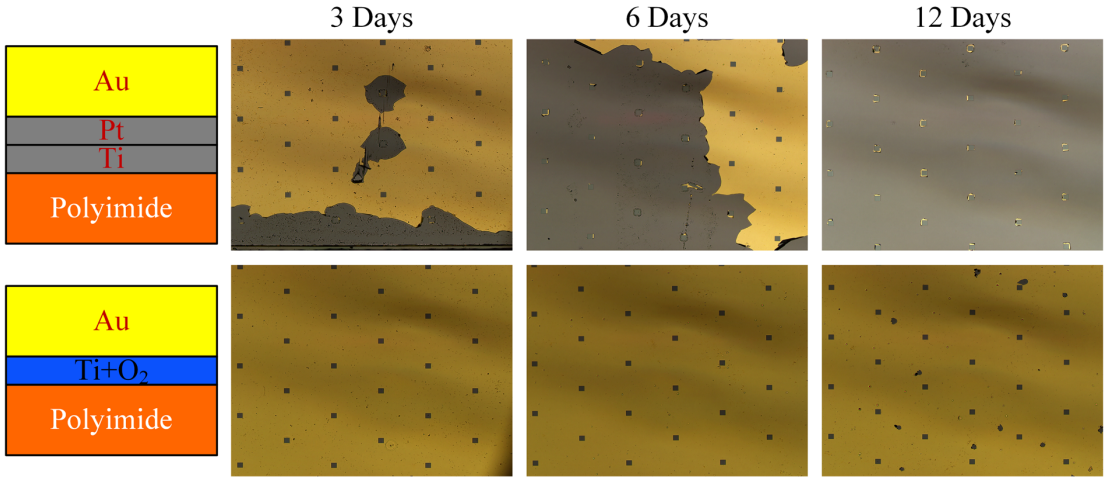

Figure 31. Adhesion test for metal-on-polyimide interface up to 12 days soaking in 87˚C PBS solution. Conventional stack shows in top raw and proposed stack shows in bottom raw. Gray surface indicates delamination. Regularly located small rectangles are pre-defined pattern to allow PBS absorption to polyimide.

Three different stacks (PI/Au as control, PI/TiO_2/Au and PI/TiO_2/Ti/Pt/Au) were prepared and tested to study the adhesion of polyimide-on-metal. Unlike metal-on-polyimide, the result of the adhesion test of polyimide-on-metal suggested that sputtered TiO_2 could be an effective adhesion layer (**Figure 32**). Polyimide on TiO_2 delaminated far more slowly than Polyimide on Au did. There existed a significant difference with and without Ti/Pt and the result suggested that the adhesion failure occurred at the interface between Au and TiO_2, not PI and Au in these cases. The amount of delamination was in an unacceptable range even with the best stack but the fact that the delamination initiated at the edge and proceeded to the center implies that some uncontrolled factor such as direct exposure to PBS and mechanical tension induced by pre-delaminated polyimide accelerate the progress. Therefore, this data is effective not for the quantitative prediction but only for the relative comparison.

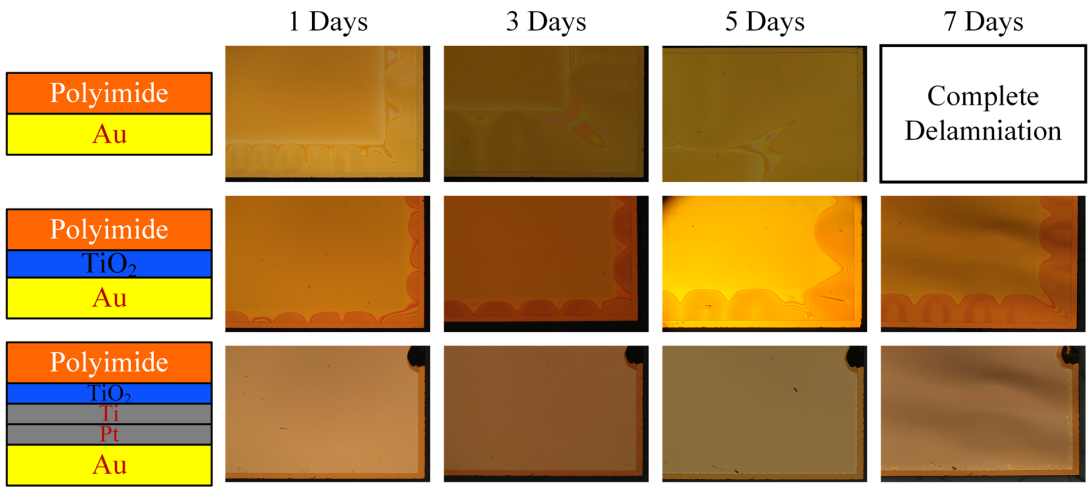

Figure 32. Adhesion test for metal-on-polyimide interface up to 7 days soaking in 87˚C PBS solution. Polyimide starts slightly inside the diced edge.

Through the preliminary adhesion test, it was proved that oxidized Ti and TiO_2 layers are effective adhesion layer for metal on polyimide and for polyimide on metal, repectively. Also, it was evidenced by the study of Chen et al. that TiO_2 showed larger work of adhesion with Pt than Au[99]. Given these findings, oxidized Ti/Pt/Au/Pt/TiO_2 was proposed for long-term reliable metal stack. However, it was not answered if TiO_2 enhances the adhesion between two polyimide layers and which interfaces fails prior to the other, polyimide-polyimide or polyimide-metal. Polyimide probes with 9 of recording channels and 16 of blind channels were fabricated and utilized for the accelerated lifetime test (ALT) as described in **Figure 33**. Blind channels have identical trace lines with normal recording channels but no electrical connection to recording sites as shown in **Figure 32b**. The recording channels were placed between every two blind channels so each blind channel would potentially crosstalk with one adjacent recording channel (**Figure 33a**). The line and space of the trace line were 0.5µm for all devices. The change of blind channel impedance was characterized to assess the lifetime in electrical performance of interfaces. The feature size of trace was 0.5µm line and 0.5µm space through 6mm-long shank and 4µm line and 4µm space through 24mm-long cable. Three different stacks including two

experimental groups and one control group were prepared (**Figure 34**). The experimental groups have metal stack of oxidized Ti/Pt/Au/Pt/TiO_2. In the first group called as "TiO_2 on field", the field outside the metal traces was coated with oxidized Ti and sputtered TiO_2 between two polyimide layers and in the other group called as "TiO_2 on metal", the field was directly interfaced with two polyimide layers. The control group has Pt/Au/Pt as metal stack and no additional adhesion layer between polyimide layers as the second experimental group.

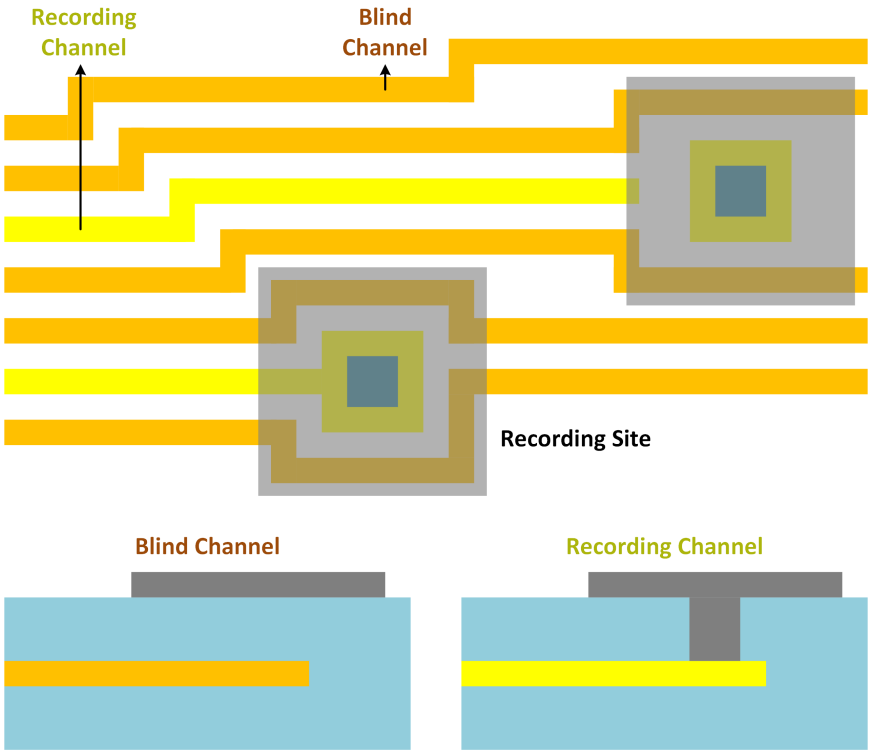

Figure 33. Blind channel and recording channel. a, layout of test sample showing two blind channels placed between recording channels. b-c. cross-section view of blind channel (b) and recording channel (c).

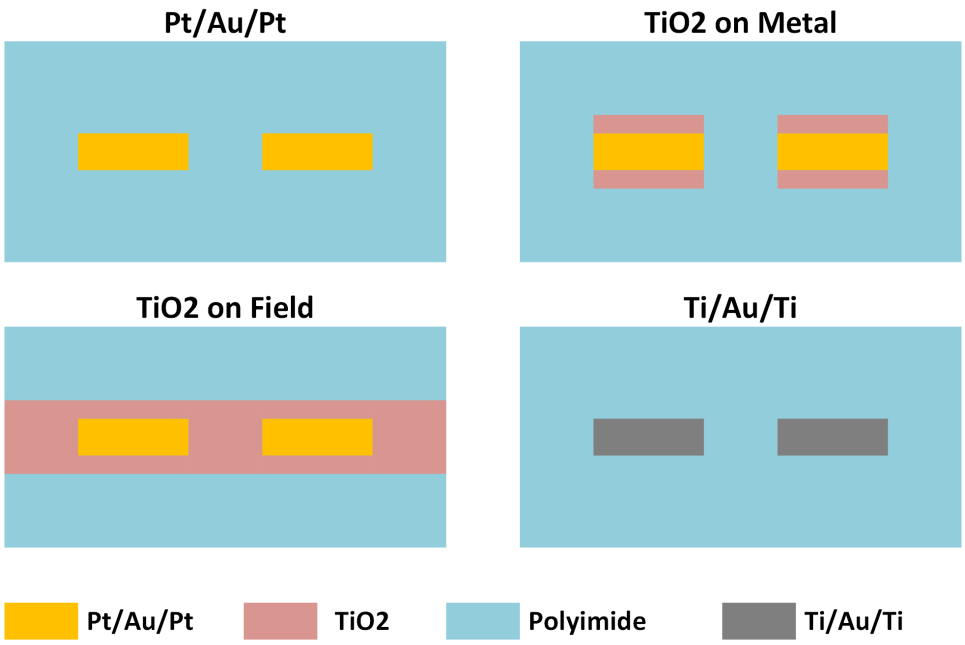

Figure 34. Cross-section of metal stacks utilized for lifetime test.

We monitored the impedance of the blind and recording channels for 12 days with soaking in 76˚C PBS solution that accelerates the test approximately with a factor of 15 compared with 37˚C in vivo condition. 3 samples per each cohort were measured and total number of channels monitored were more than 30 for each group. As seen in **Figure 35a**, the blind channel impedance of TiO_2 on field group has dropped very slightly and slowly until 12 days after soaking in 76˚C PBS while that with the control group rapidly decreased since the test started and reached near saturation state after 8 days soaking. The TiO_2 on metal group demonstrated moderate drop between two extremes. The phase change shown in **Figure 35b** was a foreseeing indication of increase of electrical coupling. For all cohorts, the phase was close to -90˚ initially indicating the coupling impedance was capacitive. As the degradation proceeded, the phase increased because of the domination of the constant phase element due to electrical double layer formed between metal and PBS. By comparing two earlier failed group, Pt/Au/PT and TiO_2 on metal, it can be hypothesized that the adhesion layers on and underneath the metal played an

significant role in the trace failure in the early phase and presumably the delamination of metal from the polyimide layer accelerated the formation of the low impedance path in the polyimide-to-polyimide interface. By comparing two experimental groups, it would be reasonable to claim that TiO_2 enhanced the adhesion between polyimides as well as the adhesion between polyimide and metal.

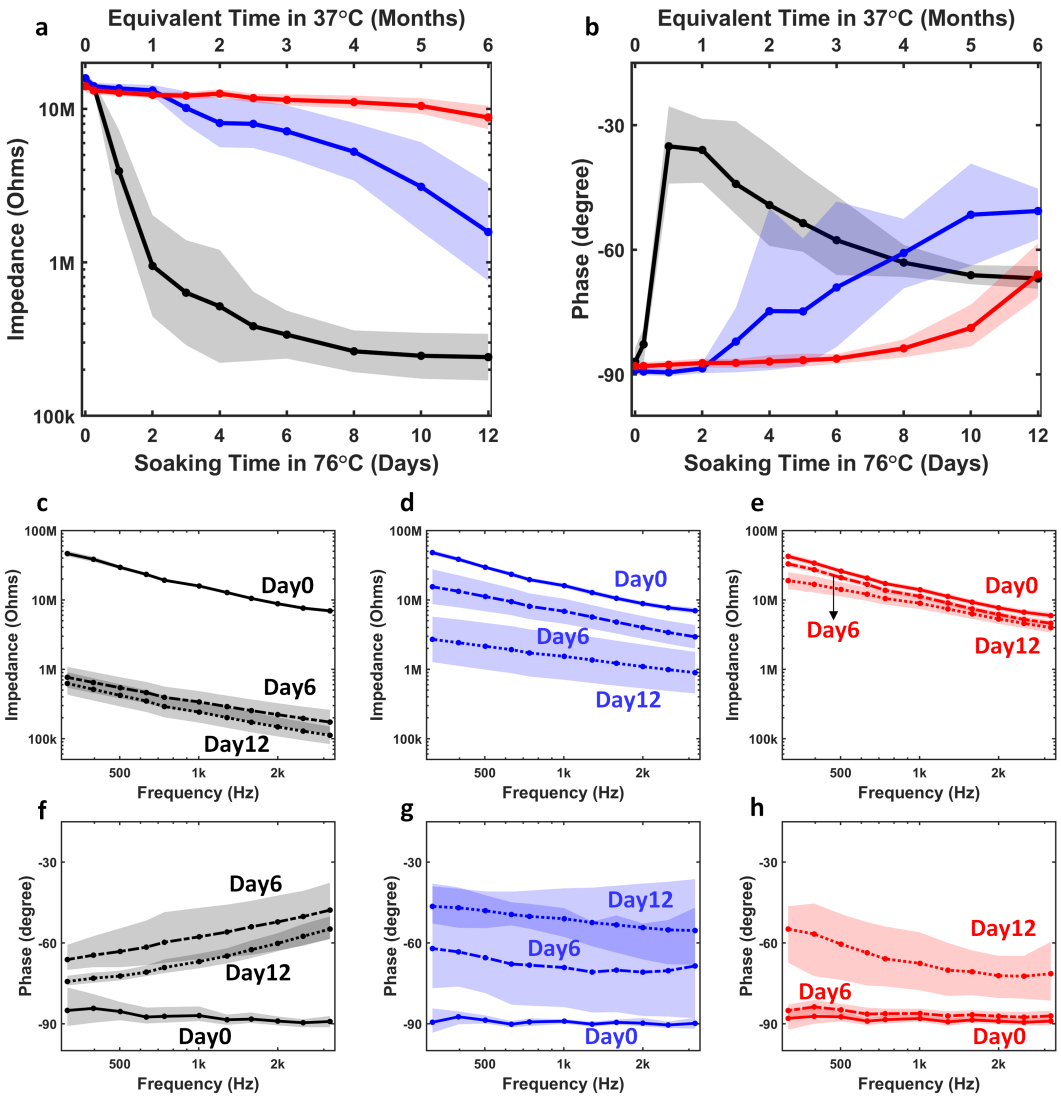

Figure 35. Result of accelerated lifetime test (ALT) over 12days in 76˚C PBS to study the adhesion improvement by TiO2. a, impedance amplitude, b, phase change of blind channel, c-h, frequency swept impedance (c-e) and phase (f-h) of Pt/Au/PT (c, f), TiO_2 on metal (d, g), and TiO_2 on field (e, f). Color codes indicate each stack, Pt/Au/Pt (black), TiO_2 on metal (blue), and TiO_2 on field (red).

Chung et al. has reported a successful recording and single unit detection from a chronic in vivo study for more than 5 months with polyimide based flexible probes using Ti/Au/Ti as the trace metal stack[37]. Though the dimensions of trace line was not specified, they might implement 3-5µm line/space features according to the reported shank width. Scaling down for high density potentially induces issues of adhesion and lifetime. Therefore, Ti/Au/Ti and the proposed stack, fabricated in our group, were tested for long-term lifetime with an identical test setup. As mentioned earlier, the proposed stack, Ti on field, showed the slow degradation and slight impedance change for 5 months equivalency. On the other hand, Ti/Au/Ti stack with 0.5µm line/space showed a rapid drop of impedance similar to Pt/Au/Pt stack as seen in **Figure 36**. The result suggested that polyimide probes with Ti/Au/Ti fabricated by our group is not reliable and applicable to a chronic in vivo study.

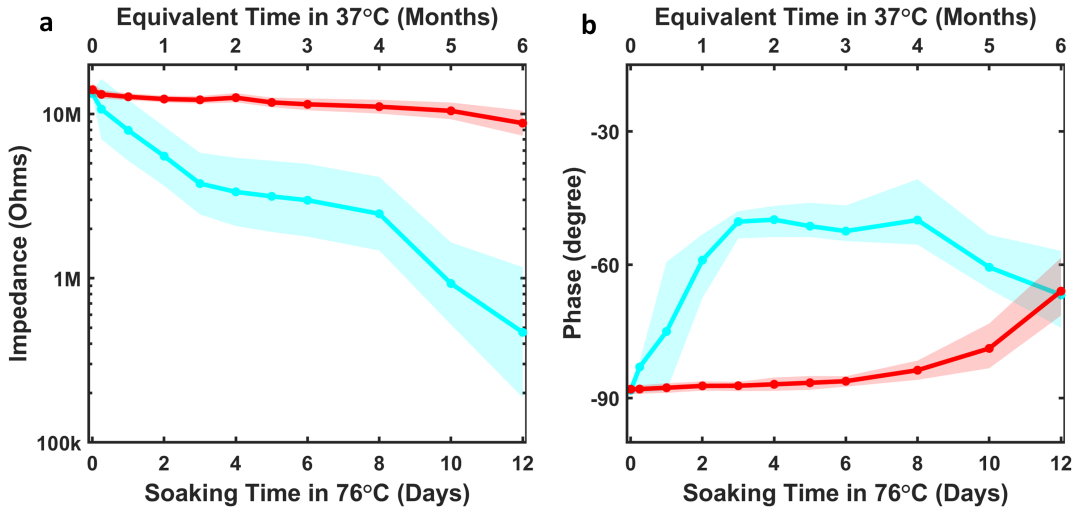

Figure 36. Result of accelerated lifetime test (ALT) over 12days in 76˚C PBS comparing the proposed stack with a conventional stack. a, impedance amplitude, b, phase change of blind channel, Color codes indicate each stack, Ti/Au/Ti (cyan) and TiO_2 on field (red).

In order to estimate the lifetime of the neural probes according to the coupling impedance, a criteria for device failure had to be defined considering performance degeneration due to increment of coupling between traces. The characteristics that can be affected by the change of coupling impedance are mainly crosstalk between channels and signal attenuation. Recorded neural signal can be attenuated by leakage current through unwanted electrical path between channels. Also, false-positive units can be detected due to channel crosstalk. The equivalent circuit model shown in **Figure 37a** suggested by Lopez et al. was used to analysis the effect of decrease of coupling impedance[100]. I assumed 200μV of neural signal input, 1MΩ of electrode impedance, and 13MΩ of load impedance of amplifier circuitry. The shunt impedance between the imbedded trace and the brain was ignored since it is usually >100MΩ and far large than other critical components mentioned above. If the ratio between the recorded signals from an input applied channel and a adjacent channel is greater than typical signal-to-noise ratio (SNR) during in vivo recording, the crosstalk signal might not be able to be detected as neural spike signal. The noise floor for in vivo is typically 20-30μV. Based upon the assumptions and the circuit model analysis, the impedance of blind channel should be larger than 7MΩ to be classified as working channel. 100% of the blind channel in TiO_2 on filed was able to maintain its high impedance after 5 months equivalency while as Pt/Au/Pt and Ti/Au/Ti showed the yields below 10% in terms of functionality after 1.5 months equivalency as seen in **Figure 37b**. This data indicates that metal to polyimide adhesion is a key factor to affect the lifetime since Pt/Au/Pt, Ti/Au/Ti and TiO_2 on metal have same PI-PI interface and different metal stacks. It could be hypothesized that adhesion failure between PI and metal occurs first and then accelerates PI-PI interface failure inducing low impedance of blind channels. Also, it was evident that TiO_2 enhanced the adhesion of PI-PI interface.

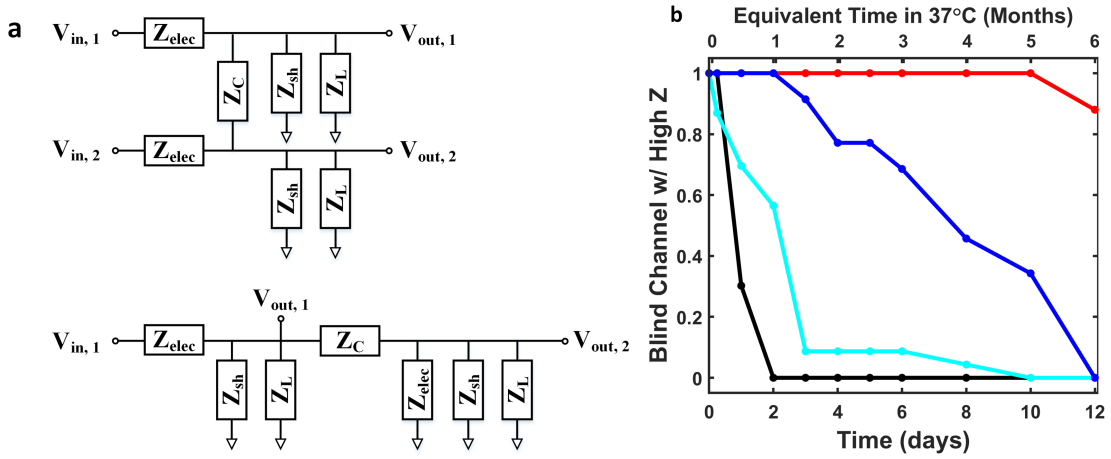

Figure 37. Equivalent circuit model and success rate of blind channels. a, equivalent circuit model of two adjacent channels and simplified circuit when input to channel 2 is grounded. b, fraction of number of blind channels with high impedance for Pt/Au/Pt (black), Ti/Au/Ti (cyan), TiO_2 on metal (blue) and TiO_2 on field (red).

In vivo Validation

Chronic in vivo experiment with the presented polyimide based neural probes was conducted. One day before the surgery, flexible probe was attached to a mechanical shuttle by PEG using the method described in Chapter 2.

The animal procedures were approved by the Institutional Animal Care and Use Committee of the New York University IACUC (protocol number: 160926). One male Long Evans rats (380 g) was used in this study. The rat was kept on a regular 12 h–12 h light–dark cycle and housed in pairs before surgery. No prior experimentation had been performed on this animal. Atropine (0.05 mg/kg, s.c.) was administered after isoflurane anesthesia induction to reduce saliva production. The body temperature was monitored and kept constant at 36–37 °C with a DC temperature controller (TCAT-LV; Physitemp, Clifton, NJ, USA). Stages of anesthesia were maintained by confirming the lack of nociceptive reflex. Skin of the head was shaved and the surface of the skull was cleaned by hydrogen peroxide (2%). A ground screw was

positioned above the cerebellum. Then, a 1.8-mm diameter craniotomy was drilled at 3 mm posterior from bregma and 2 mm lateral of the midline. The dura was removed and the flexible probe was lowered at 1 mm/min speed until we saw characteristic electrophysiological features of the CA1 region of the hippocampus on the channels that are located at the tip of the probe. 20 minutes later the flexible probe was released from the shuttle and the silicon shank was retracted. The craniotomy was covered with a small amount of silicone gel (Dow Corning® 3-4680) and we let it cure (approximately 10 minutes). We then applied very liquid Stoelting (product number: 51459) dental cement and let it cure (approximately 2 minutes). Then, we used 2-component cement (Unifast LC) to build up around the area. Once this last layer of cement is cured, the PCB of the flexible probe is released from the shuttle (personal discussion with Carl E. Schoonover). A copper-mesh based Faraday cage was built around the probe and the PCB was attached to metal bars (Vandecasteele, 2012). Buprenex was administered to the animal up to postoperative day 2.

3 days after the surgery we performed home cage recordings regularly (home cage dimensions are 40x30x50 cm, width x length x height). Each recording lasted at least 2 hours to collect enough number of spikes. The recorded signals (n = 64 channels) were acquired using an Intan RHD2000 recording system (Intantech, USA).

The recorded data was analyzed by custom scripts written in MATLAB (MathWorks, USA). Offline, spikes were detected and automatically sorted using the Kilosort algorithm (Pachitariu et al.) followed by manual curation using Phy (https://phy-contrib.readthedocs.io/) to get well-isolated single units (multi-unit and noise clusters were discarded).

The result is shown in **Figure 38**. The single units were successfully detected up to 14 days after implantation and the averaged 25 units were monitored. Spike signal and

autocorrelogram are displayed for 20 units and it is shown there are many pyramidal neurons and two interneurons according to the autocorrelogram. After implantation, there was no unit detected until 6 days and the spike signal came back after 8 days. The number of single units and signal quality such as spike amplitude and signal-to-noise ration was stably maintained up to 14 days.

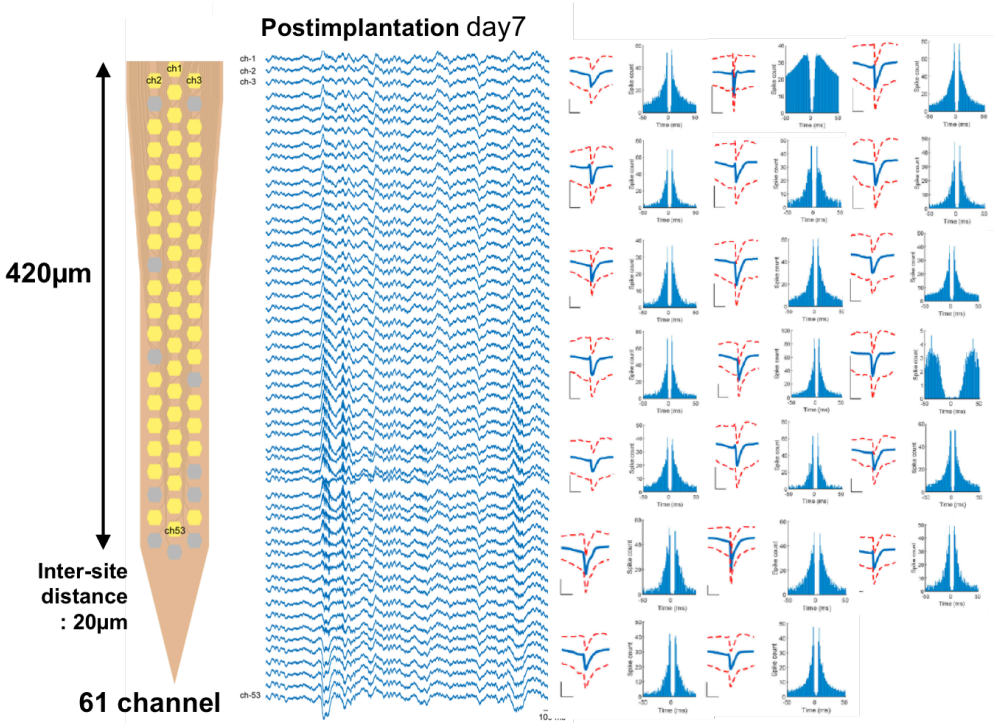

Figure 38. In vivo recording from rat hippocampus. Probe layout, raw traces at postimplantation day7 and detected single units (20 shown among total 25 isolated units).

However, a huge crosstalk was observed after 14 day after implantation. A spike signal spans all of the shank rather than centered at a certain channel and gradually distributed in terms of signal amplitude. Histogram of spike amplitude obviously showed that the neural spike signal was leaked and overall noise signal was increased to ~100μV even though the crosstalk was almost not distinguishable from a real single unit even after 83 days implantation. Impedance data implies that there were global electrical shorts showing an abrupt drop in impedance amplitude.

It was characterized that impedance of both R-Pt electrode and blind channels were consistently maintained after 5 months equivalency as plotted in **Figure 39a**. However, the impedance of blind channels was gradually decreased right after implantation and the disconnected channels also showed similar trend (**Figure 39b**). The cause for this discrepancy between in vitro accelerated test and chronic in vivo test has to be figured out. There are several possibilities. The head stage PCB and the method for securing it could be responsible in that all channels including blind channels and unintentionally disconnected channels were globally became shorted abruptly. The validity of the accelerated lifetime test also has to be reviewed and verified whether or not the test condition is much lower acceleration than expected. More devices will be chronically tested to collect a statistically meaningful amount of data.

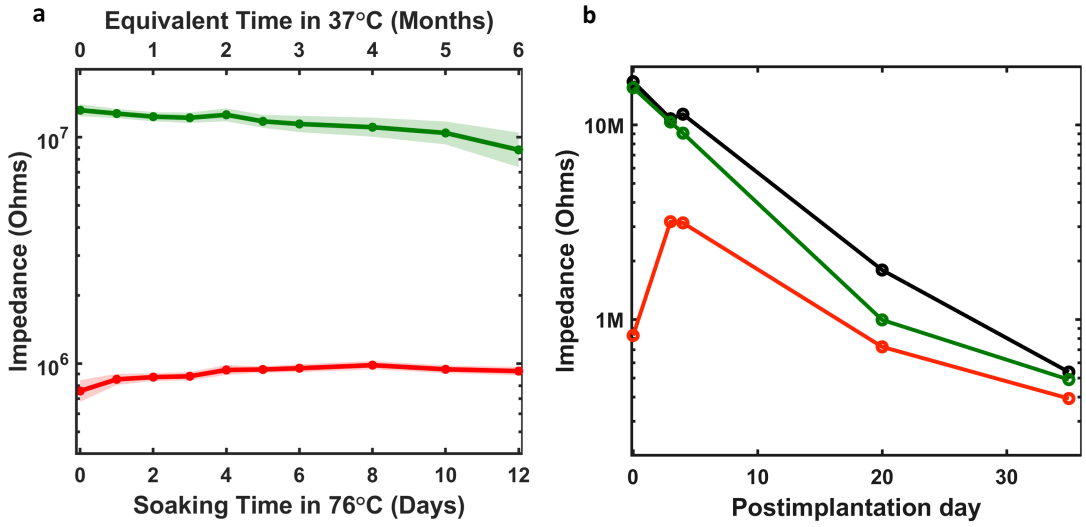

Figure 39. Impedance change of recording channels and blind channels in accelerated lifetime and chronic in vivo test. a, impedance change of R-Pt and blind channels in 76˚C PBS. Colors indicate R-Pt (red) and blind channels (green), respectively. b, impedance change of R-Pt, blind channels and disconnected channels for chronic in vivo test. Colors indicate R-Pt (red), blind channels (green), and disconnected channels (black), respectively

Discussions

In order to integrate a large channel count on a single probe shank, one might consider either increase the shank width, shrink the trace dimensions, or stack multiple trace layers. It has

been widely believed that a shank with a width more than 100μm would induce significantly more tissue damage due to its large footprint. Stacking of multiple metal lines is one way to scale the number of channel count without increasing the shank width. However, multi-layer device inevitably increases the total thickness of the probe and it will exponentially compromise the compliance since the compliance changes with a cubic of thickness while as it is proportional to the width of the device. Also, the thickness of the polymer insulation would greatly affect the long-term reliability because water diffusion would be exponentially decreased by the thickness increase. As a result, there is a trade-off between the compliance and the lifetime of device. Therefore, the probe dimensions including the trace line/gap, the polymer thickness, etc has to be smartly designed according to the targeting lifetime.

Roughened electrode was able to reduce the impedance of recording sites with a factor of 3 by wafer level process. In terms of the impedance, the best metal that can be deposited by wafer level micro-fabrication process is Iridium. However, Iridium has intrinsically high film stress up to GPa range, which makes hard to implement Iridium for polymer probes due to delamination. The increase surface area of the roughened electrode potentially enhances the adhesion between Iridium and polymer. The process for roughening still needs to be optimized since it is using extremely thin layer and careful monitoring of the deposition rate is required to maintain its performance.

It has not been theoretically proven if oxidized Ti effectively enhances the adhesion on polyimide even though it is hypothesized that a covalent bonding formation and full oxidation might eliminate the causes of adhesion failure. More sophisticated surface analysis such as XPS or TEM has to be conducted to confirm the existence of the covalent bonding and the surface

reactivity. Chemical interpretation and analysis would be required to figure out the mechanism how oxidized Ti and sputtered TiO_2 assist the adhesion of polyimide.

Accelerated lifetime test in PBS solution is a good way to anticipate the in vivo lifetime of implantable device. However, there might be much more factors that participate in the degradation such as reactions with cells and ions. The chronic in vivo results indeed presented discrepancy between ALT and in vivo. Therefore, in vivo validation is mandatory to confirm the lifetime of the devices even though a bench top test shows a promising result. Also, through chronic in vivo test, we may be able to collect much more useful information to judge the lifetime and functionality such as anatomy, LFP and spikes, spike amplitude distribution, and LFP frequency response from 1Hz-1kHz. Since it was shown that the huge crosstalk developed over time in vivo chronic was the most critical issue in terms of long-term functionality, it would be greatly beneficial to implement few blind channels along with recording channels to monitor the coupling impedance between channels. Impedance change of blind channel would be a trustable indication for growth of crosstalk.

Conclusion

A long-term reliable, polyimide based neural probe has been developed and demonstrated. Submicron patterning process by i-line stepper with an aid of contrast enhance material (CEM) was successfully developed and 64 channels could be implemented in 85μm width. A novel adhesion layer of TiO_2 was tested and showed a promising lifetime test result indicating more than 6 months of lifetime. A method for wafer level impedance lowering by substrate roughening was developed and demonstrated 3X reduction in impedance at 1kHz. Integrating the presented advances, polyimide based neural probe with 64 channel was fabricated and tested by chronic in vivo recordings. The probe was validated until 14 days after

implantation showing 25 single units in average. The probe was failed after 14 days and more chronic validation has to be performed after specifying the source of the failure.

Chapter 4.
Compact Packaging by Integration of High Density ASIC Using Anisotropic Conductive Film Bonding

Introduction

Simultaneous and parallel neural recording from higher channel count is truly demanded to understand the fundamental neural circuit and the functional connectivity more deeply. A signal redundancy due to densely packed electrode array improves the spatial resolution and the accuracy of single unit detection. Also, development of a massive parallel electrode array is essential to monitor a large volume and multiple brain regions. However, as rapidly increasing the channel count, packaging and interconnection for interfacing probe to external instrumentation becomes more burdensome[15] reported the first 4-digits (1,000) channel neural probe using e-beam lithography. But the form factor of the whole system was unacceptably large for any study beyond the head-fixed acute recording, mostly due to the huge number of the interfacing connectors. It vividly displayed the necessity of integration of a multiplexing ASIC for high channel count electrode array. ASIC can be integrated by hybrid integration[101] or monolithic integration[13]. Lopez et al demonstrated a 966-electrode neural probe in 0.13μm SOI CMOS, which implemented in situ buffering under each electrode. Their approach had substantial advantages of the fine feature using CMOS process, and convenient assembly and

small packaging due to monolithic integration. Unfortunately, it is not applicable to polymer based neural probe since a trustable solution for CMOS process on polymer does not exist yet. Chung et al reported 1,024 channel, polyimide based neural probe hybrid-integrated with recording ASIC from Intan technologies[37]. However, the packaging volume was still too large compared to the monolithic integration approach mainly due to the low density of the commercially most popular Intan ASIC. In our group, we developed a 256-channel recording ASIC with an area-efficient amplifier and a circuit-under-pad (CUP) configuration arrayed in area (Unpublished work). The most area-consuming parts in neural recording ASIC, particularly for a large number of channels, are AC-coupling capacitors in the low noise amplifier (LNA) and the bonding pads for input. In order to reduce the size, the AC coupling capacitor was placed on top of the active circuits and the top plate took the role of an input pad (**Figure 40a**). The area consumption was further reduced by shifting the half of passives for the LNA into the reference electrode. The customized ASIC presented more than 12 times higher density compared with Intan RHD2164 that is most popularly used in the community (**Figure 40b**). Furthermore, it is even > 40% denser than the monolithic approach that has the most advanced to date[13].

The CUP-configured ASIC with 2D-arrayed bonding pads brought a challenge in the interconnection. Wire bonding is not an applicable method in the area pad configuration and more importantly it applies excessively high pressure with GPa range that possibly damages the capacitor oxide under the bonding pad. MFI technology is the prevailing method for interconnection of polymer probe and capable of 2D array bonding but it also requires high pressure and relatively large pitch of bonding pad even though it is theoretically applicable to 100μm pitch. It is indisputable that flip chip bonding is well fitted to the area pad. Conventional flip chip bonding methods utilize solder as the mechanical/electrical bonding material and the

most advanced method allows very fine pitch up to 50µm in-line and 40µm/80µm for staggered as using solder-capped Cu pillar. However, it necessitates under-bump-metallization (UBM) on ASIC in order to block the solder diffusion into the circuitry and prevent the oxidation of the pad metal. UBM is more critical to CUP configured ASIC since the circuit is placed under the bonding pad and the fatal solder diffusion ruins the functionality of the circuit. Die-level process to form UBM is tricky and laborious so it would be beneficial to avoid it if possible. The solution we proposed is the flip chip bonding using anisotropic conductive film (ACF) to meet all the requirements mentioned above. ACF requires a moderate pressure (<150MPa) and temperature (<230˚C). Moreover, ACF eliminates the necessity of UBM since it is a solder-free material and the bonding capability through Al pad with the native oxide has reported[102].

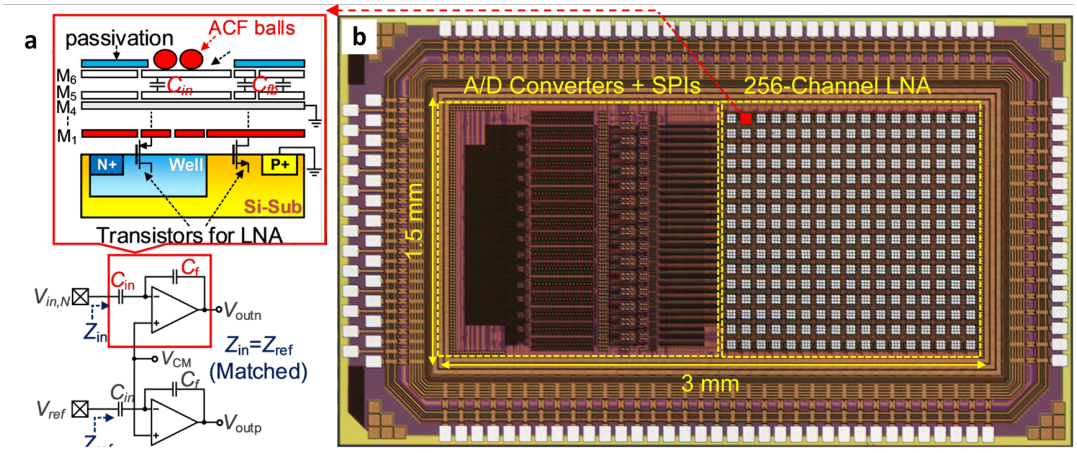

Figure 40. High density recording ASIC. a, Circuit-under-pad implementation of recording chip. b, 256-channel recording chip with CUP and area pads.

Fine Pitch Flip Chip (FPFC) Bonding

The demand for interconnection of high density and narrow pitch I/O pads on ASICs is emerging as semiconductor devices become more sophisticated and miniaturized. Flip-chip bonding technology is one of the most promising technologies to realize high density and high performance interconnection method for integrated circuit chips. For the conventional flip chip

bonding, the solder balls are formed on an IC by either electroplating, solder ball placement or stencil printing on top of underbump metallization (UBM) on IC bonding pads. The conventional solder balls are usually bigger than 100μm and thus not applicable for very fine pitch interconnection below 100μm pitch. Recent advances in solder ball formation and flip chip bonding dramatically shrunk the pad pitch as minimizing possibility of electrical shorts. It has been reported that the hybrid bump with Indium cap on Copper pillar formed by electroplating successfully demonstrated fine pitch (<20μm) interconnection without significant inter-bump interruption[103]. However, there still remain several practical issues on flip chip bonding methods using solder reflow. As the bonding pitch diminishes, the stand-off height of the bump has to be maintained to avoid electrical shorts between very close bonding pads and thus it results in high aspect ratio of bump structure. High stand-off height is also required for void-free underfilling. The high aspect ratio bumps inevitably encounters a possibility of mechanical instability and also the underfilling material should be very carefully selected to avoid or minimize the thermal/mechanical mismatch between the underfilling resin and the metal bumps. Even with a proper selection of underfilling material, there are still risks in capturing void in underfilling layer, which potentially induces excessive thermal stress and stress concentration in a joint. More practically, a die level process for UBM and bumping is tricky especially for the bonding pads on the edge of a die even though the wafer level process is more straightforward and relatively easy. Therefore, the advanced flip chip bonding techniques are not a cost efficient solution for research field where massive production is not desired.

Anisotropic conductive film (ACF) is basically a thermosetting resin containing conductive particles, which are metal-coated spheres with polymer cores. ACF bonding is lead-free and environmentally friendly flip chip bonding process and is one of the highest density

bonding methods to date (<10μm pitch). ACF bonding is being broadly used in the industry of flat panel display to bond the drive IC on glass panel. Compared with solder reflow, ACF intrinsically shows far less electrical short probability due to its working principle, in which particles without pressure are insulated. The biggest advantage of ACF bonding over flip chip bonding based on solder reflow is that ACF is a readily underfilled material with non-conductive, spreadable resin containing conductive particles so no additional underfilling is necessary. Also, it does not require further patterning/metallization on an IC die since no melting/reflow of metal is included in the process and Al pad with native oxide is readily bondable with moderate bonding pressure, 40-120MPa. ACF technology is still being advanced driven by industries' need and the new advances will be easily adaptable without significant modifications from already established setup and conditions.

Anisotropic Conductive Film (ACF) Bonding

A various types of ACF from many companies are available in the market. A selection of adequate product to our approach was a key factor for success. Through deep exploration, it was found that AC-8955YW from Hitachi chemical requires the smallest area so enables the highest density among a variety of ACFs that are available to academic research. Theoretically, 50μm-pitched area pads array with 40μm-wide pad and 10μm of space can be interconnected by this ACF. It has a double layer structure consisting of ACF layer and NCF layer (**Figure 41a**). The resin in the ACF layer has high viscosity so it is more possible to catch the particle instead of flowing out while the NCF layer has low viscosity to provide the mechanical bonding and the fluidity of the film. Also, it has conductive particles covered by an insulation layer to avoid the electrical short by laterally aligned particles even in case of 10μm space between pads (**Figure 41b**).

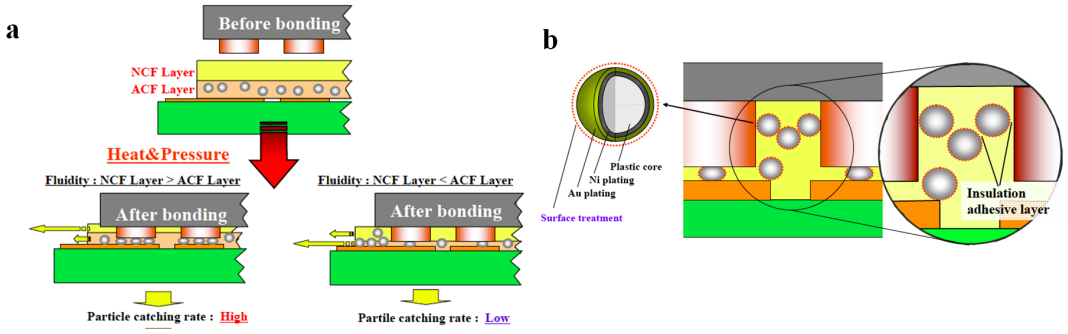

Figure 41. Advanced features of AC8955YW ACF. a, schematic to show high capture possibility of double layered ACF. b, anti-shorting surface treatment even in case of lateral alignment of particles.

The process starts with laminating and pre-bonding of ACF on the bottom substrate such as glass panel. Then, the bonding pads on the top substrate such as driver IC are aligned to those on the bottom substrate. Heat and pressure are applied to press down the conductive particle to make a sufficient deflection for electrical connection. Also, the resin is melt and cured by the heat and it provides the mechanical bonding between two substrates. (**Figure 42**)

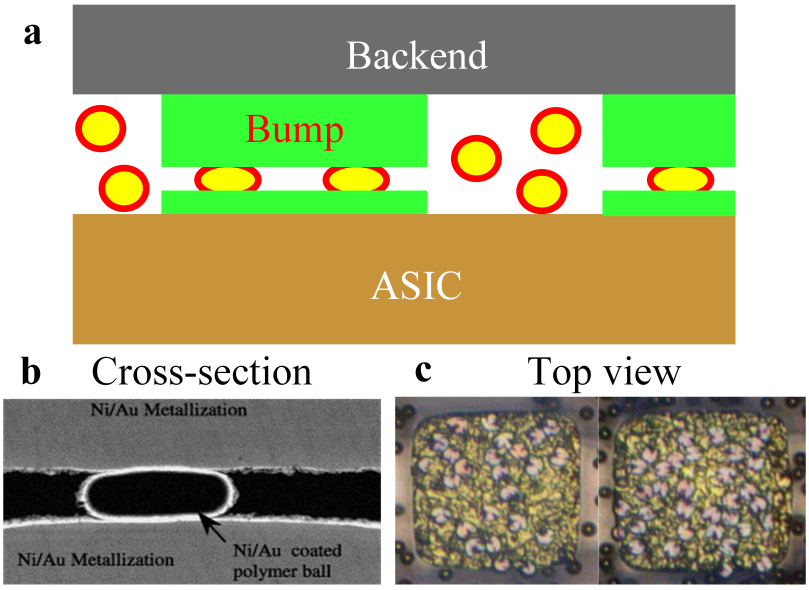

Figure 42. Working principle of anisotropic conductive film (ACF). a, schematic of working principle of ACF showing deflection of conductive particle under protruding bumps, b, cross-sectional view of a deflected particle. c, top view of captured and deflected particles.

Test samples for ACF bonding characterization have been prepared as described below. A dummy chip representing ASIC and an interposer representing probe backend were designed for four terminal sensing to measure the contact resistance, known as Kelvin sensing. All the bonding pads for ACF bonding in the dummy chip was linearly chained and terminated with large bonding pads in each end. Each ACF bonding pad in the interposer was separately routed to two outer metal pads for probing. In this manner, four terminals per each ACF bonding site were accessible to flow electrical current through two of those and to measure the voltage across the site through the other two (**Figure 43**). Another critical feature that we should test was the bonding capability on Al pads with native oxide. Thus, 1μm-thick Al layer was used as the material for the bonding pads in the dummy chip. The bumps in the interposer was electroplated Ni with 16-20μm height and was coated with 100nm-thick sputtered Au to prevent the oxidation.

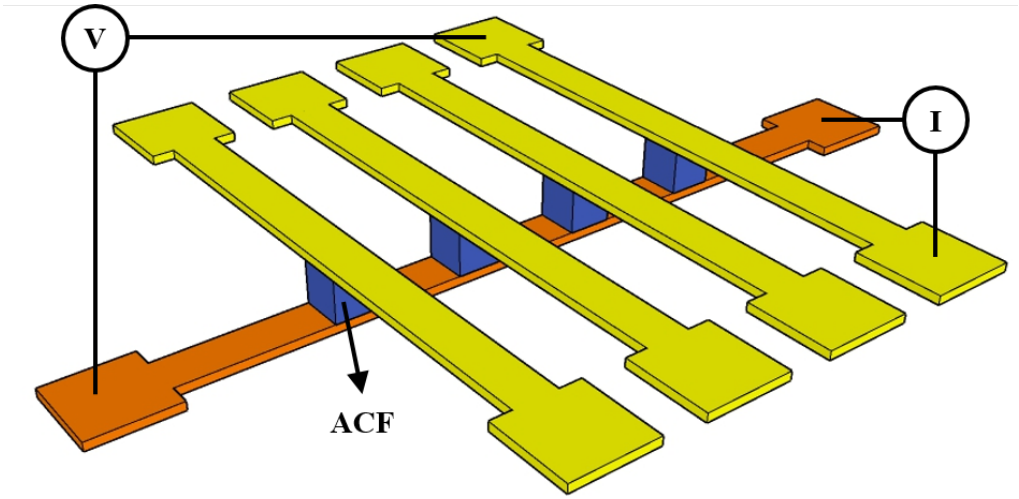

Figure 43. Test pattern design and measurement method. Orange bar represents metal on bottom plate with linearly chained bonding pads and yellow bars represent metal on top plate with two separate access to each bonding site. Voltage across a bonding site is measured while 1mA current flows across the same site. Ohmic drop due to the current takes place only in the ACF bonding.

The ACF bonding tests using the test samples described above have been conducted to find the optimal bonding condition and characterize the yield and the contact resistance of ACF

in the geometry and the system. Also, the bonding capability of ACF on Al pads with relatively thick native oxide has been verified.

For a successful flip chip bonding, the coplanarity between two surfaces is very important. Height inconsistency due to a tool's angular misalignment, die non-uniformity, bump height, debris, etc. may result in open circuit or high contact resistance. The use of PDMS cushion layer compensates the height difference and assists to distribute the pressure uniformly. 100μm thick PDMS cushion can deform 50μm with 2MPa and thus, even assuming 10s of micron height difference, it spreads 80MPa of bonding pressure with less than 2% of uniformity.

Through iteration of parametric experiment, we found that 80MPa and 230˚C are the optimal parameters. Under this condition, we have achieved 99.7% of connection yield and no electrical short observed from 5 samples having 16 by 16 pad array with 75μm pitch (**Figure 44**). Only 4 open circuits were observed among total 1280 bonding sites. The median contact resistance was 3.18Ω. The contact resistance was measured higher than the expected range mostly due to small bonding area but it is acceptable in that the resistance of the bonding is in series connection with the recoding site impedance which is in the range of several hundreds kΩ.

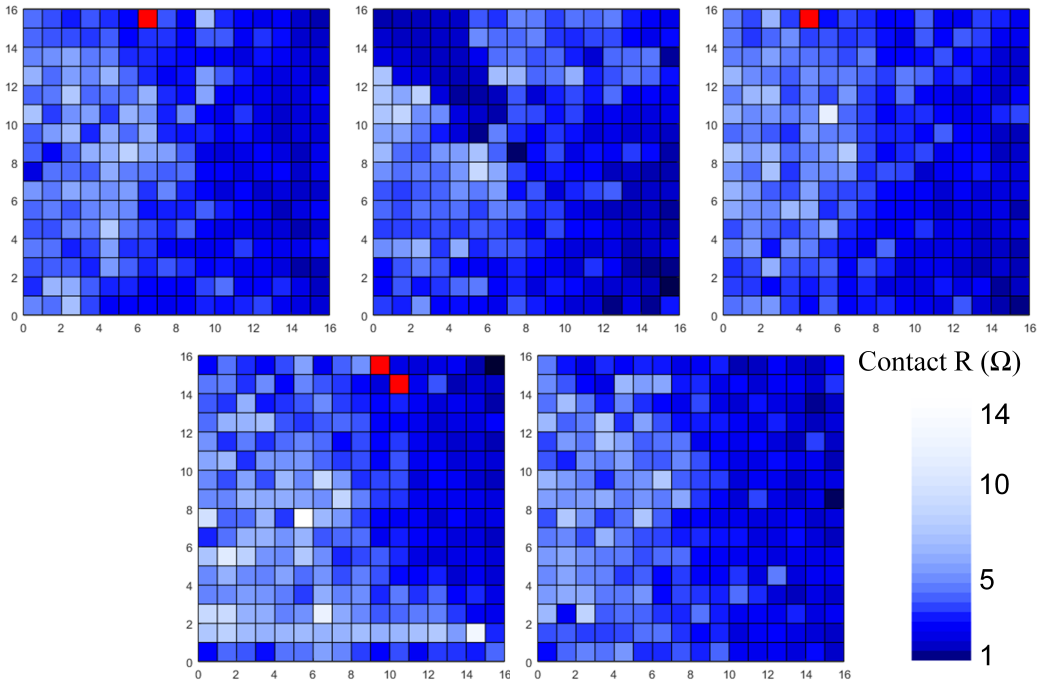

Figure 44. Bonding maps of ACF bonding from 5 samples showing connection yield and contact resistance distribution. Bonding condition was identical to all samples with 120MPa and 230˚C. Red indicates open circuit.

The fidelity of ACF bonding was tested by applying 3mA DC current continuously as shown in **Figure 45**. The contact resistances of 10 bonding sites were monitored up to 240 hours. Except three outliers, seven of them showed less than 3% difference in either direction. The contact resistance of two of three outliers abruptly dropped at a certain time point and stayed. Only site presented relatively large increase ~7% but it also seemed stable once it bounced.

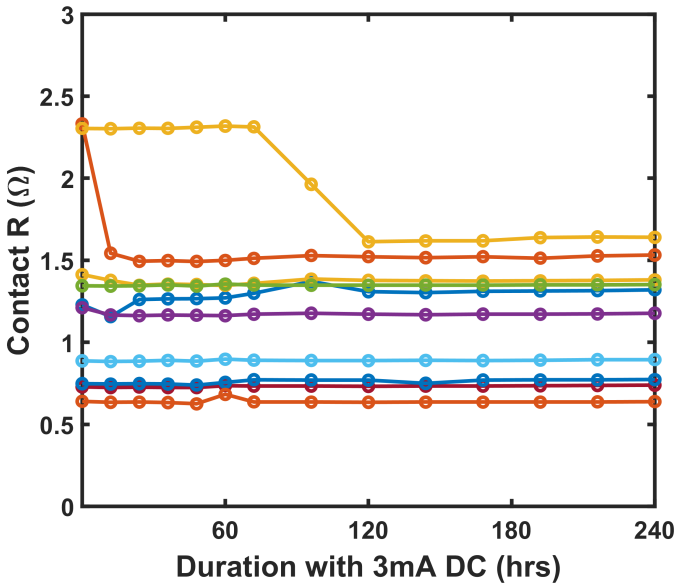

Figure 45. Fidelity test of ACF bonding by continuously flowing 3mA DC current. Two outliers showed abrupt drop and stayed stable. 7 sites showed less than 3% difference during 240 hours. N=10.

Probe design

The electrode and probe design was identical to the aforementioned polytrode with 20µm inter-electrode distance, 420µm span, and 193µm^2 area. This time, 64 channel and 256 channel probes were laid out with the identical shank design and with single and four shanks, respectively. At the backend of 256 channel version, 256 of bumps were placed as 16 by 16 array with 75µm pitch including 40µm of bump width and 35µm of inter-space, which matched with the configuration on the recording ASIC and met the working specification of the chosen ACF, AC-8955YW. For 64-channel, the bump was arrayed as 4 by 16 with the same dimension. The targeted bump height was between 16-20µm in order for ACF to work properly. The backend size was 2.3mm by 2.4mm, slightly smaller than ASIC size.

Fabrication

The fabrication process basically added the rigid and bumped backend to the probe fabrication in chapter 2. The process flow is illustrated in **Figure 46**. The process began with a

silicon wafer with 2μm-thick thermally grown silicon dioxide layer. TiO_2 was deposited to improve the adhesion of polyimide on the wafer, followed by bottom polyimide layer spinning and curing. An adhesion improving layers of oxidized Ti and TiO_2 were deposited and submicron metal (Pt/Au/Pt, 10/40/10nm) was defined by liftoff process. Then, the polyimide below the area for the trace and the bump on the backend was removed by oxygen plasma. Larger metal patterning, deposition of TiO_2 adhesion layer, spinning and curing of second polyimide, polyimide etching, electrode patterning were done as same as the previously presented process. The SiO_2 on the backside was patterned after the second polyimide curing. Au coated Ni bump array was formed through the processes of seed layer deposition, PR patterning for electroplating, Ni electroplating, Au deposition following Ar etching for oxide removal, and etching of seed layer with PR mask. The wafer was mounted on a carrier wafer using Santovac as a bonding material and Si was etched by DRIE with patterned silicon dioxide as the etch mask until the etch stop layer of the top silicon dioxide layer was exposed. The oxide was removed in BHF and the devices were released in acetone by removing Santovac.

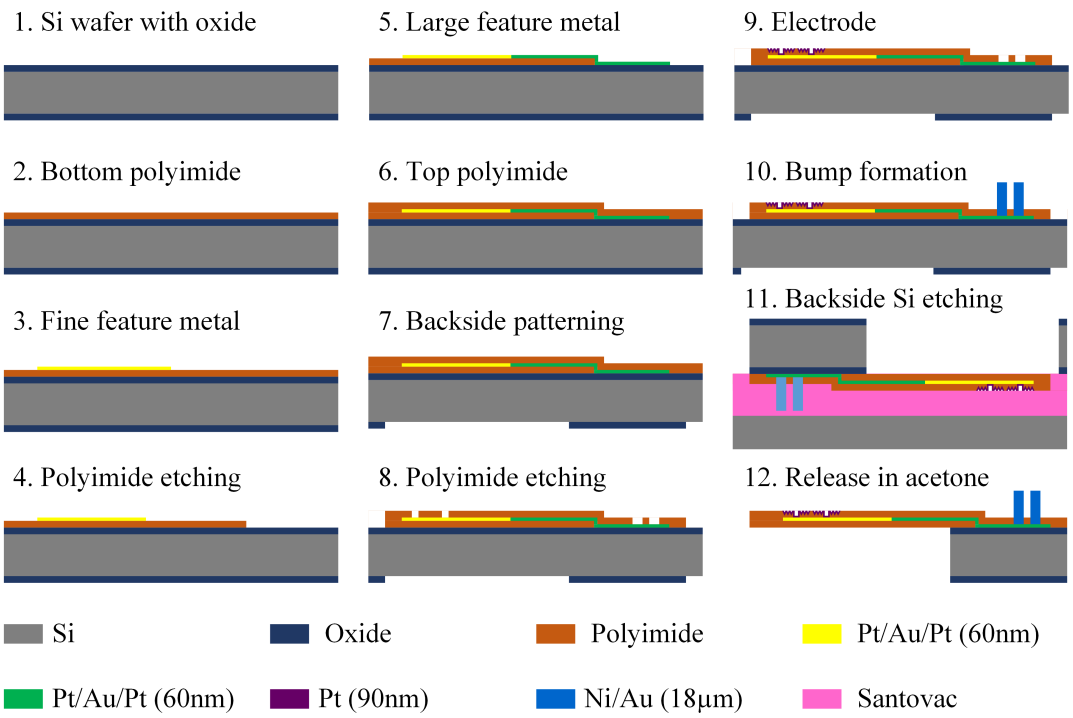

Figure 46. Process flow of polyimide-based neural probe with roughened electrodes, rigid and bumped backend.

Packaging and assembly

The ASIC was integrated with the fabricated probe utilizing ACF bonding. The ACF bonding process was conducted using a flip chip bonder (Fineplacer lambda, Finetech Inc.) that enables <3μm alignment accuracy. 2mm by 3mm piece of ACF was pre-bonded on ASIC after removing a protection tape. Then, the protection film on the other side was removed and probe backend was pre-bonded on ACF layer with careful alignment. ASIC-ACF-probe stack, active probe was pressed in the same tool with 80MPa pressure and temperature was increased to 230˚C. In order to assist co-planarity between the device and the tool head, PDMS sheet was placed inbetween as a pressure buffer. The active probe was attached on a PCB with glue and silver paste and then the pads for power, ground and signal peripheral interface (SPI) on ASIC were wire-bonded to the pads on PCB with two of 12-pins Omnetics connectors. After testing the

functionality of the system by in vitro setup, the probe shank was mounted on a rigid shuttle in a way described in Chapter 2.

In vitro characterization

The active probe was characterized with an in vitro setup described in **Figure 47**. The headstage PCB with the active probe was connected to the motherboard with FPGA through two standard SPI cables from Intan Technology. The shank of polyimide probe was soaked in PBS solution in which a counter electrode was soaked and the counter electrode was electrically interfaced with the recording sites on the probe by electrical double layer formation. The ground and the reference pins on the headstage were tied and the counter electrode was also tied for the input referred noise measurement (**Figure 47a**). For in vitro signal recording, input signal of sinusoidal wave with 1 mV_{p-p} and 1 kHz was generated by a function generator and 100X attenuator, and applied between GND/REF of the headstage and the counter electrode that was soaked in PBS solution as shown in **Figure 47b**.

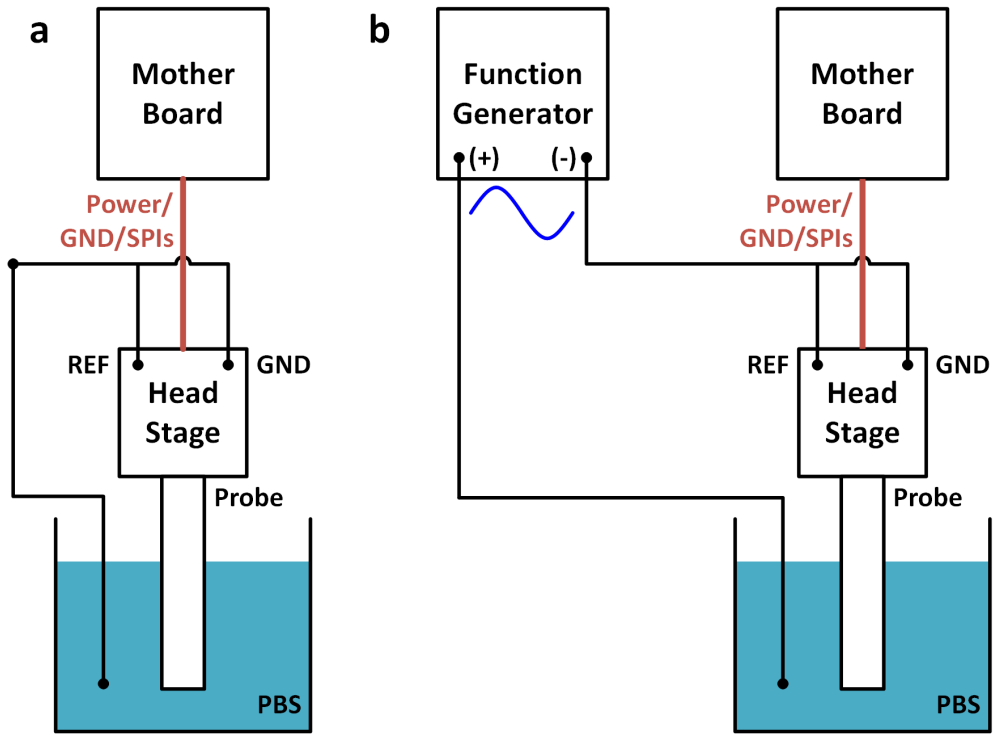

Figure 47. Measurement setup for in vitro characterization. a, for input referred noise measurement, b, for in vitro signal recording.

In order to verify the setup, 32-ch Intan headstage (RHD 2132, Intan Technologies) and silicon based neural probe from Neurolight Technologies were used as reference. The input referred noise of Intan headstage and silicon probe measured with the setup was 2.5 μV_{rms} in average over 16 channels, which is fitted to Intan's reported specification. Also, RMS noise from 1 mV_{p-p} sine wave input at 1kHz was measured as 7.5 μV_{rms} and it is well agreed with typical RMS noise during in vivo, 6-10μV_{rms}. The in vitro setup was validated that it doesn't generate unexpectedly large noise and is valid to characterize the system. The characterization result from the active probe is presented in **Figure 48**. The input referred noise of the system was measured as 12.5 μV_{rms} (**Figure 48a**). The output recorded from the sinusoidal input is seen in **Figure 48b** and the SNR was calculated as 27.2 dB in average across 16 channels through fast furrier transform (FFT) analysis, which is shown **Figure 48c**. The SNR of the active probe was

measured with 1mV$_{p-p}$ input signal between 300-4,000Hz of frequency that covers most of neural spike and as shown in **Figure 48d**, the SNR was quite consistent over the neural spike frequencies.

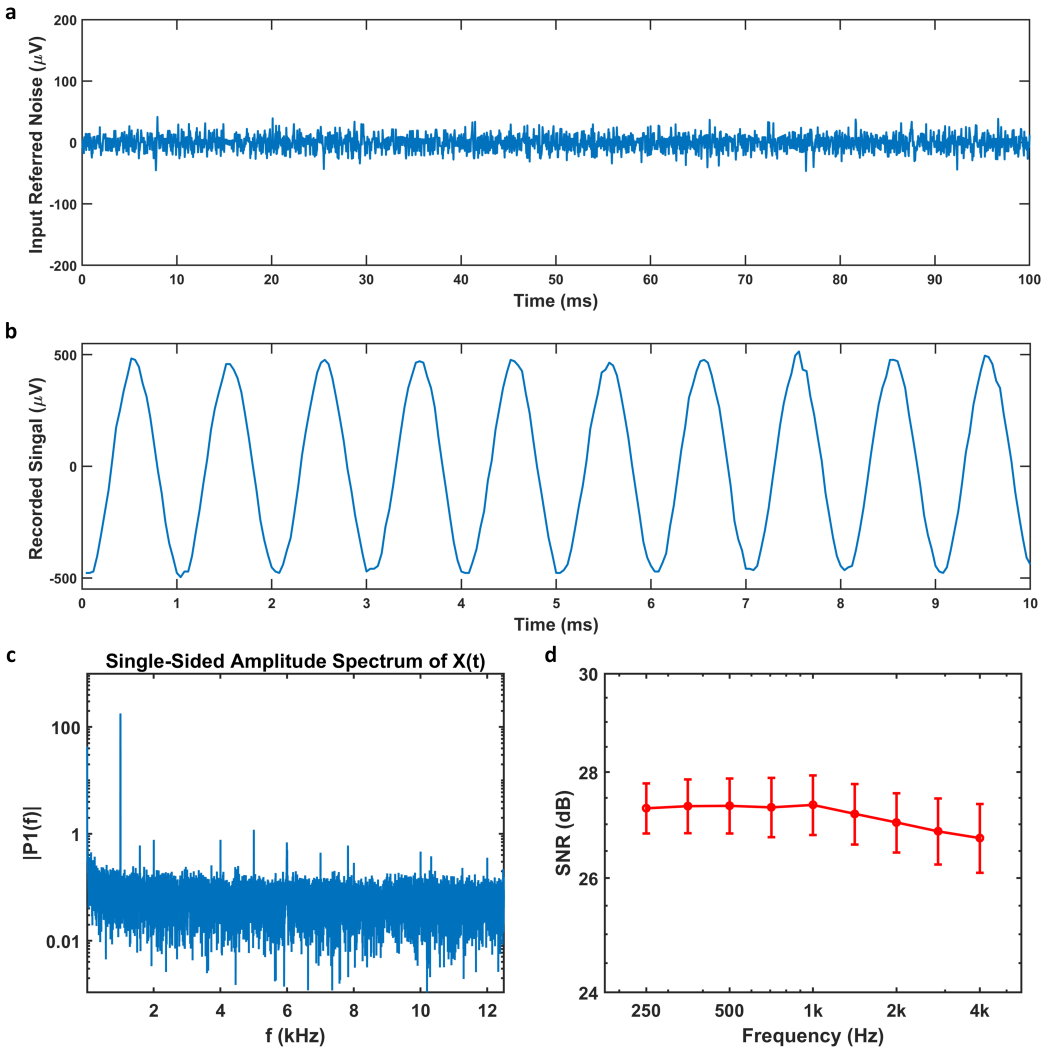

Figure 48. In vitro characterization of active probe. a, Input referred noise of ASIC with a polyimide probe assembled. b, recorded signal from 1mVp-p sine wave input at 1kHz. c, FFT in the frequency domain showing peak at 1 kHz. d, measured and calculated SN according to the frequency of input signal.

In vivo validation

In vivo experiment was conducted to verify the functionality of the integrated system. The assembled probe was mounted and temporarily fixed on a planar UNCD shuttle using the

method explained in Chapter 2. This method successfully worked for 4 shanks within 5μm of alignment accuracy in the width direction.

The animal procedures were approved by the Institutional Animal Care and Use Committee of the New York University IACUC and the University of Michigan IACUC (protocol numbers are: 160926 and PRO-7275). One-one male Long Evans rats (380 g) were used in the acute study. The rats were kept on a regular 12 h–12 h light–dark cycle and housed in pairs before surgery. No prior experimentation had been performed on this animal. Atropine (0.05 mg/kg, s.c.) was administered after isoflurane anesthesia induction to reduce saliva production. The body temperature was monitored and kept constant at 36–37 °C with a DC temperature controller (TCAT-LV; Physitemp, Clifton, NJ, USA). Stages of anesthesia were maintained by confirming the lack of nociceptive reflex. Skin of the head was shaved and the surface of the skull was cleaned by hydrogen peroxide (2%). A ground screw was positioned above the cerebellum. Then, a 1.8-mm diameter craniotomy was drilled at 3 mm posterior from bregma and 2 mm lateral of the midline. The dura was removed and the flexible probe was lowered at 1 mm/min speed until we saw characteristic electrophysiological features of the CA1 region of the hippocampus on the channels that are located at the tip of the probe.

To test an active probe, the craniotomy was filled with sterile saline solution and 2 hour recording was performed under anesthesia. The recorded signals (n = 256 channels) were acquired using C code based recording software that is developed in our group. At the end of the recording, the animal was euthanized.

The recorded data were analyzed by custom scripts written in MATLAB (MathWorks, USA). Offline, spikes were detected and automatically sorted using the Kilosort algorithm

(Pachitariu et al.) followed by manual curation using Phy (https://phy-contrib.readthedocs.io/) to get well-isolated single units (multi-unit and noise clusters were discarded).

The recorded in vivo data is shown in **Figure 49**. This is an unfiltered, raw trace and the shanks are 250μm apart from each other. Clear local field potential (LFP) signal such as sharp ripples was successfully recorded from total 198 channels. Spike events are indicated with different colors showing firing from several neighboring channels and gradual distribution in amplitude along those channels. It is more obviously observed in highlighted plot in **Figure 50**. After spike sorting of 25 min recording session data, 20 clean clusters were found by automatic sorting and manual curation. Some examples of the detected single units are displayed in **Figure 51**. The calculated RMS noise after high pass filtered at 500Hz was 17μV_{rms}. Throughout the in vivo experiment, the functionality of the assembled package was validated by recorded neural signal of LFP and spike signals.

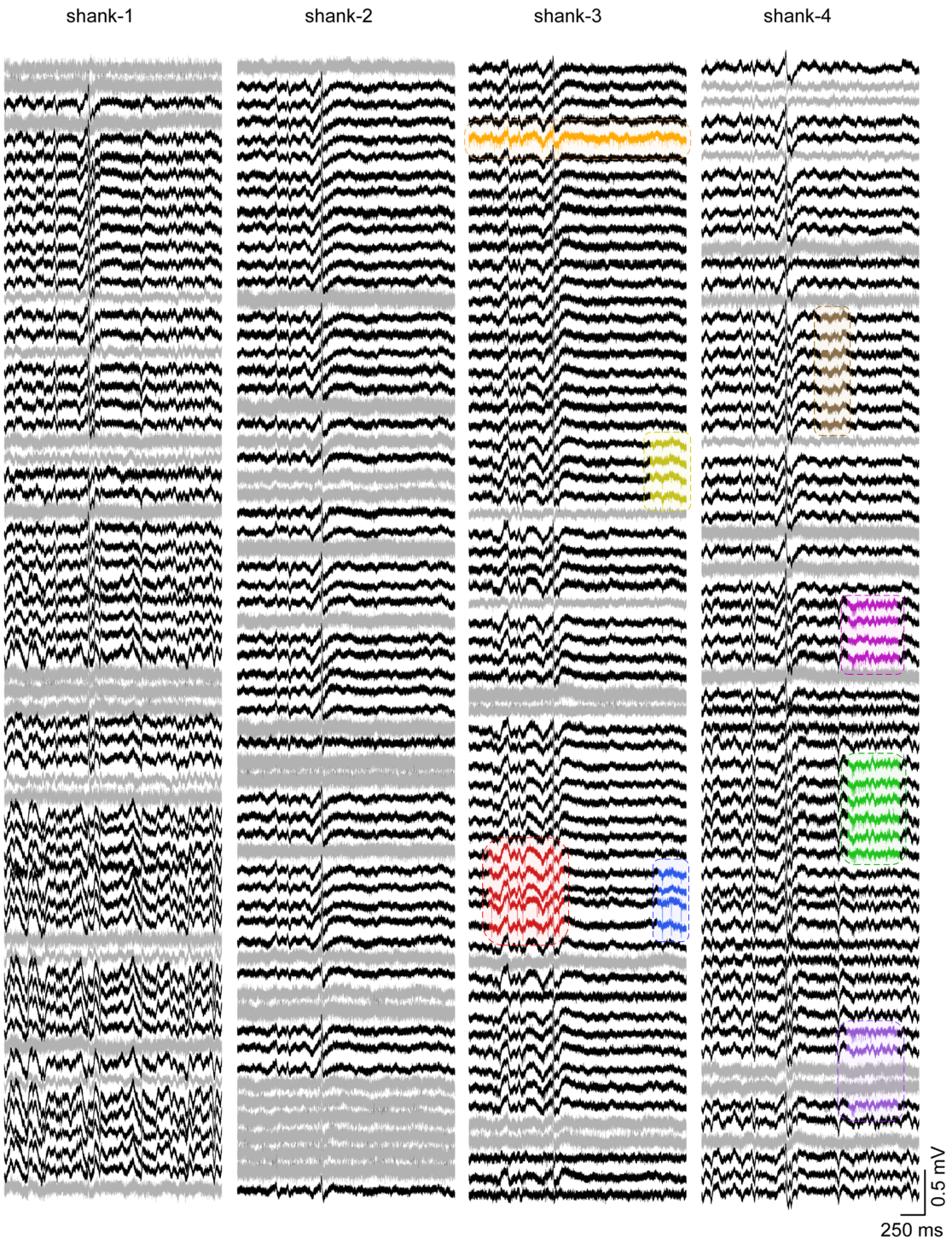

Figure 49. Raw in vivo data from 256-ch active probe on a rat. Bottom is the tip of the probe and each color indicates different spike events.

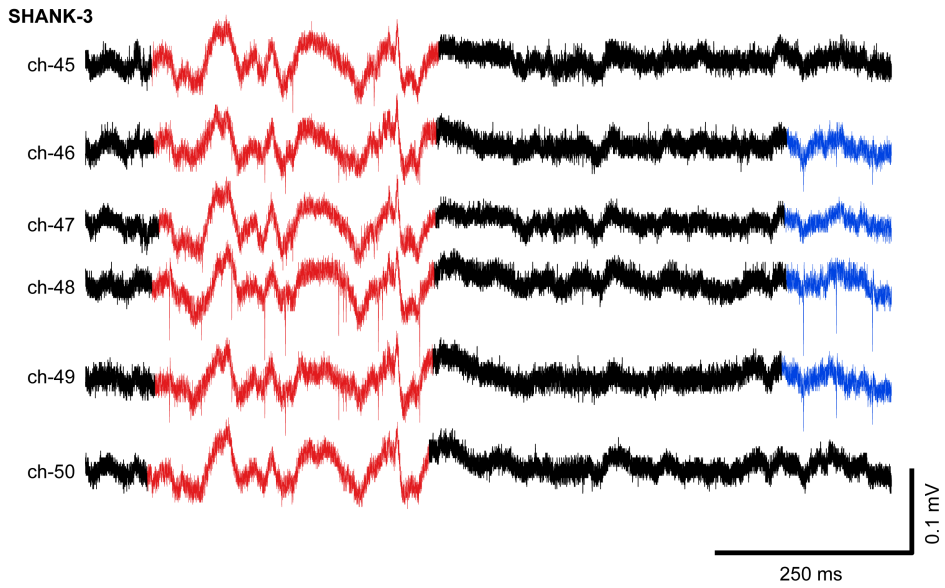

Figure 50. Highlighted view of the channels with spikes on shank 3.

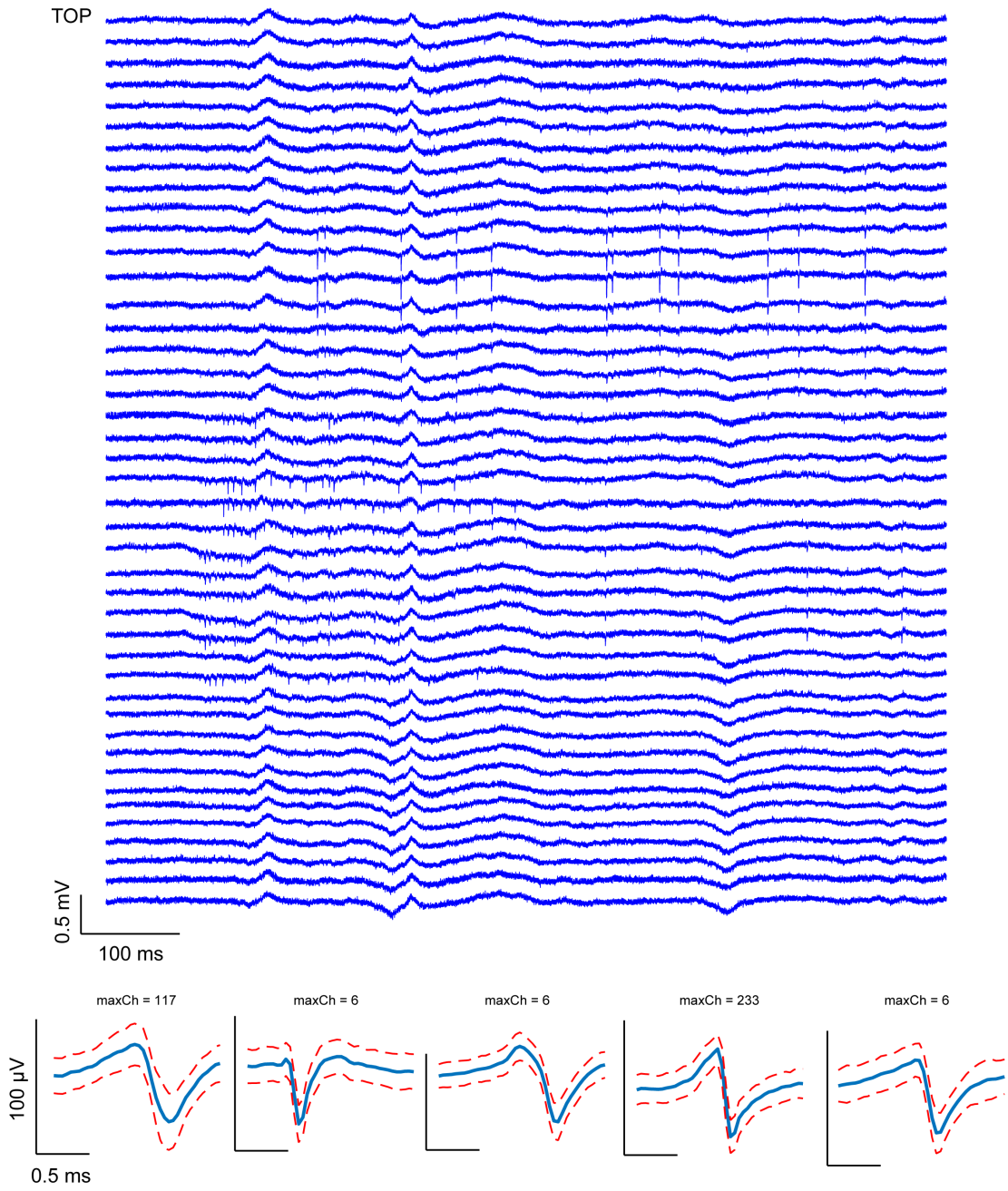

Figure 51. Raw in vivo data from shank 3 and examples of detected single units. Bottom is the tip of the probe. 5 of representative single units are displayed.

Discussions

Even though the LFP and the spike signal were measured and clusters were founded through spike sorting, there are still several issues remaining. First, the spike signal was successfully measured from only two shanks although other shanks also showed LFP signals. Presumably, the location of the other two shanks was out of the hippocampus and it implies that the implantation procedure has to be optimized furthermore. Second, system integration has to be improved. The noise floor of active probe was higher than the conventional head stage from Intan Technologies. We found that ASIC itself has ~10μV_{rms} input referred noise. Also, simultaneous recording from 256 channels showed significant increment of noise compared with 64 channels recording from the identical system, especially when the head stage is interfaced with the motherboard by 90cm-long cable unlike 15cm-long cable. Therefore, optimization and revision of ASIC design and system integration would be required for quality improvement.

ACF bonding would be potentially a good solution for high-density interconnection in that the development of ACF technology is driven by industries and is being rapidly advanced. However, the uniformity of the bump height will become more critical as the pitch of bonding site shrinks. PDMS cushion I presented would help to mitigate the issue but it is rather more beneficial to fabricate uniform bump array to begin with. Chemical mechanical polishing (CMP) process following over plating of bump metal has to be adapted for further improvement.

Conclusion

ASIC integrated, 256-channel recording system with a 4-shank polyimide neural probe was presented. A 256-channels neural probe with Ni/Au bumped silicon backend was fabricated and interconnected with 256-channel high density ASIC by ACF flip chip bonding. The form factor of the proposed system demonstrated 4X increase in channel count density per package

volume. The system was characterized by an in vitro recording setup and the noise floor was measured as $17\mu V_{rms}$. An acute In vivo validation was conducted and LFP signal from 198 channels and 20 clusters from spike signal were detected. Noise reduction through system optimization is required and also in vivo validation with more probes is needed with a precise positioning of probes.

Chapter 5.
Summary and Future Works

Summary

We have developed a versatile T-shaped ultra-nano-crystalline diamond shuttle which provides a 56% reduction in cross-sectional area compared to a planar silicon shuttle with equivalent insertion strength, and still stiff enough to insert into different neural structures in small and medium animal models with the dura and epineurium intact. This same structure will theoretically reduce micro-vascular damage by 37% compared to standard probes. In vivo experiments with cat DRG and rat brain with dura verified the penetration capability of UNCD shuttle and the neural signals were successfully recorded.

A long-term reliable, polyimide based neural probe has been developed and demonstrated. Submicron patterning process by i-line stepper with an aid of contrast enhance material (CEM) was successfully developed and 64 channels with 0.5μm line and 0.5μm space could be implemented in 85μm width. A novel adhesion layer of TiO_2 was tested and showed a promising lifetime test result indicating more than 6 months of lifetime. A method for wafer level impedance lowering by substrate roughening was developed. The measured impedance of the roughened Pr electrode was 350kΩ at 1kHz and demonstrated 3X reduction compared with plain Pt electrodes. Integrating the presented advances, polyimide based neural probe with 64

channel was fabricated and tested by chronic in vivo recordings. The probe was validated until 14 days after implantation reliably showing 25 single units in average.

ASIC integrated, 256-channel recording system with a 4-shank polyimide neural probe was presented. A 256-channels neural probe with Ni/Au bumped silicon backend was fabricated and interconnected with 256-channel high density ASIC by ACF flip chip bonding. The form factor of the proposed system demonstrated 4X increase in channel count density per package volume. ACF bonding was characterized and measured as 99.7% yield with 3.2Ω of median contact resistance. The system was characterized by an in vitro recording setup and the noise floor was measured as $17\mu V_{rms}$. An acute In vivo validation was conducted and LFP signal from 198 channels and 20 clusters from spike signal were detected.

Overall, a compact package of 256-channel neural probe with high compliance was developed. As seen in **Figure 52**, both the channel density per volume and the compliance of the probe were improved compared with the state-of-the-art active flexible probe system reported by Chung et al.

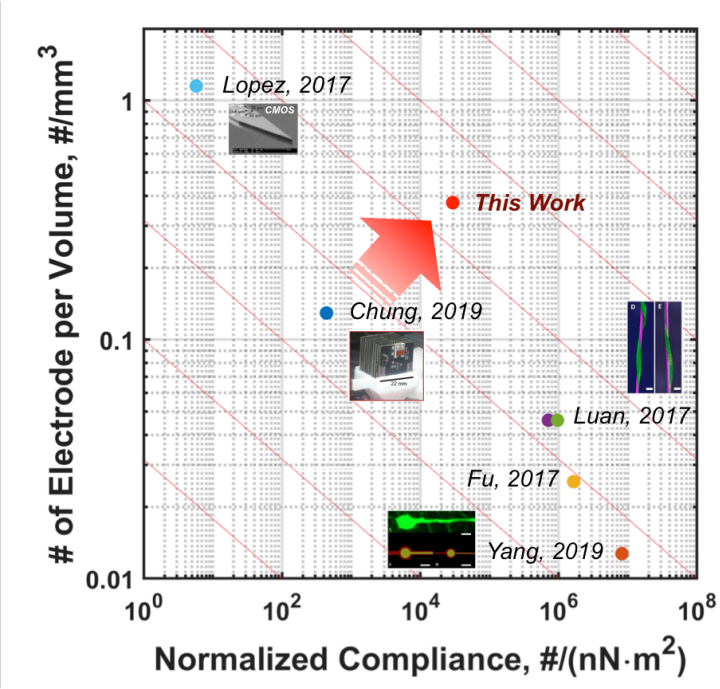

Figure 52. Figure of merit with compliance normalized to channel count and electrode density in package volume.

Future works

The long-term reliability of the polyimide probe with the proposed stack has to be verified by in vivo chronic test though the bench top test showed promising result. 4 animals will be implanted and sustained more than 1 month. SNR, impedance and number of detected single unit will be monitored as the evidence of functionality. A prolonged chronic recording will be performed for at least one animal if the functionality maintains successfully. Also, a study on in vivo reliability with various feature sizes, especially gap between traces, will provide necessary information for effective design guide considering target lifetime.

The active probe has to be optimized for system integration and data transportation and it needs to be validated by an acute in vivo experiment. Spike detection from all 4 shanks will be the indication of a successful recording. As the channel count emerges, data transportation is

potentially going to be a bottleneck for scaling up the electrode. Driving many signal lines through long cable with high inductance induces a lot of issues on data stability. In order to mitigate the issues, miniaturized FPGA has to be integrated on the head stage. That approach would also be beneficial to build a modular configuration.

Bibliography

[1] C. M. Gray, P. E. Maldonado, M. Wilson, and B. McNaughton, "Tetrodes markedly improve the reliability and yield of multiple single-unit isolation from multi-unit recordings in cat striate cortex," *J. Neurosci. Methods*, vol. 63, no. 1, pp. 43–54, 1995.

[2] K. D. Harris, D. A. Henze, J. Csicsvari, H. Hirase, B. Aki, D. Kenneth, D. A. Henze, and J. Csicsvari, "Accuracy of Tetrode Spike Separation as Determined by Simultaneous Intracellular and Extracellular Measurements," *J. Neurophysiol.*, vol. 84, no. 1, pp. 401–414, 2000.

[3] T. J. Blanche, M. A. Spacek, J. F. Hetke, N. V Swindale, J. Timothy, M. A. Spacek, J. F. Hetke, and N. V Swindale, "Polytrodes : High-Density Silicon Electrode Arrays for Large-Scale Multiunit Recording," *J. Neurophysiol.*, vol. 93, pp. 2987–3000, 2004.

[4] G. Buzsáki, "Large-scale recording of neuronal ensembles," *Nat. Neurosci.*, vol. 7, no. 5, pp. 446–451, 2004.

[5] K. D. Wise, J. B. Angell, and A. Starr, "Integrated-Circuit Approach to Extracellular Microelectrodes," *IEEE Trans. Biomed. Eng.*, vol. 17, no. 3, pp. 238–247, 1970.

[6] K. D. Wise, A. M. Sodagar, Y. Yao, M. N. Gulari, G. E. Perlin, and K. Najafi, "Microelectrodes, microelectronics, and implantable neural microsystems," *Proc. IEEE*, vol. 96, no. 7, pp. 1184–1202, 2008.

[7] P. K. Campbell, K. E. Jones, R. J. Huber, K. W. Horch, and R. A. Normann, "A silicon-based, three-dimensional neural interface: manufacturing processes for an intracortical electrode array," *IEEE Trans. Biomed. Eng.*, vol. 38, no. 8, pp. 758–768, 1991.

[8] L. R. Hochberg, M. D. Serruya, G. M. Friehs, J. A. Mukand, M. Saleh, A. H. Caplan, A. Branner, D. Chen, R. D. Penn, and J. P. Donoghue, "Neuronal ensemble control of prosthetic devices by a human with tetraplegia," vol. 442, no. July, 2006.

[9] M. Ballini, J. Müller, P. Livi, Y. Chen, U. Frey, A. Stettler, A. Shadmani, V. Viswam, I. L. Jones, D. Jäckel, M. Radivojevic, M. K. Lewandowska, W. Gong, M. Fiscella, D. J. Bakkum, F. Heer, and A. Hierlemann, "A 1024-Channel CMOS Microelectrode Array With 26 , 400 Electrodes for Recording and Stimulation of Electrogenic Cells In Vitro," *J. Solid-State Circuits*, vol. 49, no. 11, pp. 2705–2719, 2017.

[10] D. Khodagholy, J. N. Gelinas, T. Thesen, W. Doyle, O. Devinsky, G. G. Malliaras, and G. Buzsáki, "NeuroGrid : recording action potentials from the surface of the brain," *Nat. Neurosci.*, vol. 18, no. 2, pp. 310–316, 2015.

[11] F. A. C. Azevedo, L. R. B. Carvalho, L. E. A. T. Grinberg, R. E. L. Ferretti, R. E. P. Leite, W. J. Filho, and R. Lent, "Equal Numbers of Neuronal and Nonneuronal Cells Make the Human Brain an Isometrically Scaled-Up Primate Brain," *J. Comp. Neurol.*, vol. 513, no. September 2008, pp. 532–541, 2009.

[12] "stevenson." [Online]. Available: Https://stevenson.lab.uconn.edu/scaling/#.

[13] C. M. Lopez, S. Mitra, J. Putzeys, B. Raducanu, M. Ballini, A. Andrei, S. Severi, M. Welkenhuysen, C. Van Hoof, S. Musa, and R. F. Yazicioglu, "A 966-Electrode Neural Probe with 384 Configurable Channels in 0 . 13 μ m SOI CMOS," *2016 IEEE Int. Solid-State Circuits Conf.*, pp. 392–393, 2016.

[14] F. Wu, L. W. Tien, F. Chen, J. D. Berke, D. L. Kaplan, and E. Yoon, "Silk-backed structural optimization of high-density flexible intracortical neural probes," *J. Microelectromechanical Syst.*, 2015.

[15] J. Scholvin, J. P. Kinney, J. G. Bernstein, C. Moore-Kochlacs, N. Kopell, C. G. Fonstad, and E. S. Boyden, "Close-Packed Silicon Microelectrode for Scalable Spatially Oversampled Neural Recording," *IEEE Trans. Biomed. Eng.*, vol. 63, no. 1, pp. 120–130, 2016.

[16] J. J. Jun, N. A. Steinmetz, J. H. Siegle, D. J. Denman, M. Bauza, B. Barbarits, A. K. Lee, C. A. Anastassiou, A. Andrei, Ç. Aydin, M. Barbic, T. J. Blanche, V. Bonin, J. Couto, B. Dutta, S. L. Gratiy, D. A. Gutnisky, M. Häusser, B. Karsh, P. Ledochowitsch, C. M. Lopez, C. Mitelut, S. Musa, M. Okun, M. Pachitariu, J. Putzeys, P. D. Rich, C. Rossant, W. L. Sun, K. Svoboda, M. Carandini, K. D. Harris, C. Koch, J. O'Keefe, and T. D. Harris, "Fully integrated silicon probes for high-density recording of neural activity," *Nature*, 2017.

[17] V. S. Polikov, P. A. Tresco, and W. M. Reichert, "Response of brain tissue to chronically implanted neural electrodes," *J. Neurosci. Methods*, vol. 148, pp. 1–18, 2005.

[18] A. J. Sawyer and T. R. Kyriakides, "Nanoparticle-based evaluation of blood – brain barrier leakage during the," 2013.

[19] K. A. Potter, A. C. Buck, W. K. Self, and J. R. Capadona, "Stab injury and device implantation within the brain results in inversely multiphasic neuroinflammatory and neurodegenerative responses," *J. Neural Eng.*, vol. 9, p. 046020, 2012.

[20] T. D. Y. Kozai, T. C. Marzullo, F. Hooi, N. B. Langhals, A. K. Majewska, E. B. Brown, and D. R. Kipke, "Reduction of neurovascular damage resulting from microelectrode insertion into the cerebral cortex using in vivo two-photon mapping," *J. Neural Eng.*, vol. 7, no. 4, p. 46011, 2010.

[21] C. S. Bjornsson, S. J. Oh, Y. A. Al-Kofahi, Y. J. Lim, K. L. Smith, J. N. Turner, S. De, B. Roysam, W. Shain, and S. J. Kim, "Effects of insertion conditions on tissue strain and vascular damage during neuroprosthetic device insertion," *J. Neural Eng.*, vol. 3, pp. 196–207, 2006.

[22] M. B. Christensen, S. M. Pearce, N. M. Ledbetter, D. J. Warren, G. A. Clark, and P. A. Tresco, "The foreign body response to the Utah Slant Electrode Array in the cat sciatic nerve," *Acta Biomater.*, vol. 10, no. 11, pp. 4650–4660, 2014.

[23] A. Gilletti and J. Muthuswamy, "Brain micromotion around implants in the rodent somatosensory cortex," *J. Neural Eng.*, vol. 3, no. 3, p. 189, 2006.

[24] J. Muthuswamy and A. Gilletti, "Tissue Micromotion Induced Stress Around Brain Implants," in *EMBS*, 2005, no. May, pp. 102–103.

[25] P. S. Tsai, J. P. Kaufhold, P. Blinder, B. Friedman, P. J. Drew, H. J. Karten, P. D. Lyden, and D. Kleinfeld, "Correlations of neuronal and microvascular densities in murine cortex revealed by direct counting and colocalization of nuclei and vessels," *J. Neurosci.*, vol. 29, no. 46, pp. 14553–14570, 2009.

[26] A. Lecomte, E. Descamps, and C. Bergaud, "A review on mechanical considerations for chronically-implanted neural probes," *J. Neural Eng.*, vol. 15, p. 031001, 2018.

[27] J. P. Seymour and D. R. Kipke, “Neural probe design for reduced tissue encapsulation in CNS,” *Biomaterials*, vol. 28, no. 25, pp. 3594–3607, 2007.

[28] T. D. Yoshida Kozai, N. B. Langhals, P. R. Patel, X. Deng, H. Zhang, K. L. Smith, J. Lahann, N. A. Kotov, and D. R. Kipke, “Ultrasmall implantable composite microelectrodes with bioactive surfaces for chronic neural interfaces,” *Nat. Mater.*, vol. 11, no. 12, pp. 1065–1073, 2012.

[29] J. Subbaroyan, D. C. Martin, and D. R. Kipke, “A finite-element model of the mechanical effects of implantable microelectrodes in the cerebral cortex,” 2005.

[30] A. Sridharan, J. K. Nguyen, J. R. Capadona, and J. Muthuswamy, “Compliant intracortical implants reduce strains and strain rates in brain tissue in vivo,” *J. Neural Eng.*, vol. 12, p. 036002, 2015.

[31] Y. Kim, R. W. Hitchcock, M. J. Bridge, and P. A. Tresco, “Chronic response of adult rat brain tissue to implants anchored to the skull,” *Biomaterials*, vol. 25, pp. 2229–2237, 2004.

[32] K. C. Cheung, P. Renaud, H. Tanila, and K. Djupsund, “Flexible polyimide microelectrode array for in vivo recordings and current source density analysis,” *Biosens. Bioelectron.*, vol. 22, pp. 1783–1790, 2007.

[33] X. Yang, T. Zhou, T. J. Zwang, G. Hong, Y. Zhao, R. D. Viveros, T. Fu, T. Gao, and C. M. Lieber, “Bioinspired neuron-like electronics,” *Nat. Mater.*, vol. 18, pp. 510–517, 2019.

[34] T. Fu, G. Hong, R. D. Viveros, T. Zhou, and C. M. Lieber, “Highly scalable multichannel mesh electronics for stable chronic brain electrophysiology,” *Proc. Natl. Acad. Sci.*, vol. 114, no. 47, pp. E10046–E10055, 2017.

[35] L. Luan, X. Wei, Z. Zhao, J. J. Siegel, O. Potnis, C. A. Tuppen, S. Lin, S. Kazmi, R. A. Fowler, S. Holloway, A. K. Dunn, R. A. Chitwood, and C. Xie, “Ultraflexible nanoelectronic probes form reliable, glial scar–free neural integration,” *Sci. Adv.*, 2017.

[36] S. Guan, J. Wang, X. Gu, Y. Zhao, R. Hou, H. Fan, L. Zou, L. Gao, and M. Du, “Elastocapillary self-assembled neurotassels for stable neural activity recordings,” *Sci. Adv.*, vol. 5, no. March, p. eaav2842, 2019.

[37] J. E. Chung, H. R. Joo, J. L. Fan, L. F. Greengard, V. M. Tolosa, and L. M. Frank, “High-Density, Long-

Lasting, and Multi-region Electrophysiological Recordings Using Polymer Electrode Arrays," *Neuron*, vol. 101, no. 1, pp. 21–31, 2019.

[38] J. E. Chung, H. R. Joo, J. L. Fan, D. F. Liu, A. H. Barnett, S. Chen, C. Geaghan-breiner, M. P. Karlsson, M. Karlsson, K. Y. Lee, L. F. Greengard, V. M. Tolosa, and L. M. Frank, "High-density, long-lating, and multi-region electrophysiological recordings using polymer electrode arrays," *bioRxiv*, p. 242693, 2018.

[39] T. D. Y. Kozai and D. R. Kipke, "Insertion shuttle with carboxyl terminated self-assembled monolayer coatings for implanting flexible polymer neural probes in the brain," *J. Neurosci. Methods*, vol. 184, no. 2, pp. 199–205, 2009.

[40] J. W. Salatino, K. A. Ludwig, T. D. Y. Kozai, and E. K. Purcell, "Glial Responses to Implanted Electrodes in the Brain," *Nat. Biomed. Eng.*, vol. 1, pp. 862–877, 2017.

[41] E. D. Motti, H. G. Imhof, and M. G. Yaşargil, "The terminal vascular bed in the superficial cortex of the rat. An SEM study of corrosion casts.," *J. Neurosurg.*, vol. 65, pp. 834–846, 1986.

[42] T. W. Secomb, R. Hsu, N. B. Beamer, and B. M. Coull, "Theoretical simulation of oxygen transport to brain by networks of microvessels: effects of oxygen supply and demand on tissue hypoxia.," *Microcirculation*, vol. 7, no. 4, pp. 237–247, 2000.

[43] A. Weerasuriya and A. P. Mizisin, "The blood-nerve barrier: structure and functional significance," in *The Blood-Brain and Other Neural Barriers*, Springer, 2011, pp. 149–173.

[44] P. K. Thomas, "The connective tissue of peripheral nerve: an electron microscope study.," *J. Anat.*, vol. 97, no. Pt 1, pp. 35–44, 1963.

[45] J. T. Maikos, R. A. I. Elias, and D. I. Shreiber, "Mechanical properties of dura mater from the rat brain and spinal cord," *J. Neurotrauma*, vol. 25, no. 1, pp. 38–51, 2008.

[46] A. K. Ostrowski, Z. J. Sperry, G. Kulik, and T. M. Bruns, "Quantitative models of feline lumbosacral dorsal root ganglia neuronal cell density," *J. Neurosci. Methods*, vol. 290, pp. 116–124, 2017.

[47] C. T. Nordhausen, P. J. Rousche, and R. A. Normann, "Optimizing recording capabilities of the Utah intracortical electrode array," *Brain Res.*, vol. 637, no. 1, pp. 27–36, 1994.

[48] H. A. C. Wark, R. Sharma, K. S. Mathews, E. Fernandez, J. Yoo, B. Christensen, P. Tresco, L. Rieth, F. Solzbacher, and R. A. Normann, "A new high-density (25 electrodes/mm2) penetrating microelectrode array for recording and stimulating sub-millimeter neuroanatomical structures," *J. Neural Eng.*, vol. 10, no. 4, p. 45003, 2013.

[49] P. J. Rousche and R. A. Normann, "A method for pneumatically inserting an array of penetrating electrodes into cortical tissue," *Ann. Biomed. Eng.*, vol. 20, no. 4, pp. 413–422, 1992.

[50] A. Branner, R. B. Stein, E. Fernandez, Y. Aoyagi, and R. A. Normann, "Long-term stimulation and recording with a penetrating microelectrode array in cat sciatic nerve," *IEEE Trans. Biomed. Eng.*, vol. 51, no. 1, pp. 146–157, 2004.

[51] H. A. C. Wark, K. S. Mathews, R. A. Normann, and E. Fernandez, "Behavioral and cellular consequences of high-electrode count Utah Arrays chronically implanted in rat sciatic nerve.," *J. Neural Eng.*, vol. 11, no. 4, p. 046027, Jul. 2014.

[52] D. McCreery, S. Cogan, S. Kane, and V. Pikov, "Correlations between histology and neuronal activity recorded by microelectrodes implanted chronically in the cerebral cortex," *J. Neural Eng.*, vol. 13, no. 3, p. 36012, 2016.

[53] S. Wendelken, D. M. Page, T. Davis, H. A. C. Wark, D. T. Kluger, C. Duncan, D. J. Warren, D. T. Hutchinson, and G. A. Clark, "Restoration of motor control and proprioceptive and cutaneous sensation in humans with prior upper-limb amputation via multiple Utah Slanted Electrode Arrays (USEAs) implanted in residual peripheral arm nerves," *J. Neuroeng. Rehabil.*, vol. 14, no. 1, p. 121, 2017.

[54] S. L. BeMent, K. D. Wise, D. J. Anderson, K. Najafi, and K. L. Drake, "Solid-state electrodes for multichannel multiplexed intracortical neuronal recording," *Biomed. Eng. IEEE Trans.*, vol. 2, pp. 230–241, 1986.

[55] S. Herwik, S. Kisban, a a a Aarts, K. Seidl, G. Girardeau, K. Benchenane, M. B. Zugaro, S. I. Wiener, O. Paul, H. P. Neves, and P. Ruther, "Fabrication technology for silicon-based microprobe arrays used in acute and sub-chronic neural recording," *J. Micromechanics Microengineering*, vol. 19, no. 7, p. 074008, Jul.

2009.

[56] K. C. Cheung, K. Djupsund, Y. Dan, and L. P. Lee, “Implantable multichannel electrode array based on SOI technology,” *Microelectromechanical Syst. J.*, vol. 12, no. 2, pp. 179–184, 2003.

[57] T. Saxena, L. Karumbaiah, E. A. Gaupp, R. Patkar, K. Patil, M. Betancur, G. B. Stanley, and R. V. Bellamkonda, “The impact of chronic blood-brain barrier breach on intracortical electrode function,” *Biomaterials*, vol. 34, no. 20, pp. 4703–4713, 2013.

[58] T. Boretius, J. Badia, A. Pascual-Font, M. Schuettler, X. Navarro, K. Yoshida, and T. Stieglitz, “A transverse intrafascicular multichannel electrode (TIME) to interface with the peripheral nerve.,” *Biosens. Bioelectron.*, vol. 26, no. 1, pp. 62–9, Sep. 2010.

[59] S. Wurth, M. Capogrosso, S. Raspopovic, J. Gandar, G. Federici, N. Kinany, A. Cutrone, A. Piersigilli, N. Pavlova, and R. Guiet, “Long-term usability and bio-integration of polyimide-based intra-neural stimulating electrodes,” *Biomaterials*, vol. 122, pp. 114–129, 2017.

[60] S. Takeuchi, T. Suzuki, K. Mabuchi, and H. Fujita, “3D flexible multichannel neural probe array,” *J. micromechanics microengineering*, vol. 14, no. 1, p. 104, 2004.

[61] C. Boehler, F. Oberueber, S. Schlabach, T. Stieglitz, and M. Asplund, “Long-Term Stable Adhesion for Conducting Polymers in Biomedical Applications: IrOx and Nanostructured Platinum Solve the Chronic Challenge,” *ACS Appl. Mater. Interfaces*, vol. 9, pp. 189–197, 2017.

[62] S. H. Felix, K. G. Shah, V. M. Tolosa, H. J. Sheth, A. C. Tooker, T. L. Delima, S. P. Jadhav, L. M. Frank, and S. S. Pannu, “Insertion of Flexible Neural Probes Using Rigid Stiffeners Attached with Biodissolvable Adhesive,” *J. Vis. Exp.*, no. 79, pp. 1–12, 2013.

[63] O. Auciello and A. V Sumant, “Status review of the science and technology of ultrananocrystalline diamond (UNCD^{TM}) films and application to multifunctional devices,” *Diam. Relat. Mater.*, vol. 19, no. 7, pp. 699–718, 2010.

[64] O. Auciello, P. Gurman, M. B. Guglielmotti, D. G. Olmedo, A. Berra, and M. J. Saravia, “Biocompatible ultrananocrystalline diamond coatings for implantable medical devices,” *MRS Bull.*, vol. 39, no. 7, pp. 621–

629, 2014.

[65] S. Ganguli, S. P. Costello, and W. N. Gill, “Theory of Free Boundary Step Coverage in Chemical Vapor Deposition,” *Ind. Eng. Chem. Res*, vol. 34, pp. 3380–3391, 1996.

[66] H. Komiyama, Y. Shimogaki, and Y. Egashira, “Chemical reaction engineering in the design of CVD reactors,” *Chem. Eng. Sci.*, vol. 54, pp. 1941–1957, 1999.

[67] M. Eckert, E. Neyts, and A. Bogaerts, “Molecular Dynamics Simulations of the Sticking and Etch Behavior of Various Growth Species of (Ultra)Nanocrystalline Diamond Films,” *Chem. Vap. Depos.*, 2008.

[68] H. D. Espinosa and B. Peng, “A new methodology to investigate fracture toughness of freestanding MEMS and advanced materials in thin film form,” *J. Microelectromechanical Syst.*, 2005.

[69] N. Moldovan, H. Zeng, J. A. Carlisle, and R. Divan, “Advanced Diamond Technologies, Inc.,” 2010.

[70] I. D. Johnston, D. K. McCluskey, C. K. L. Tan, and M. C. Tracey, “Mechanical characterization of bulk Sylgard 184 for microfluidics and microengineering,” *J. Micromechanics Microengineering*, vol. 24, no. 3, 2014.

[71] J. Subbaroyan and D. R. Kipke, “Chronic injury response evoked by intracortical microelectrodes in different tethering modalities,” pp. 1–33.

[72] A. Gefen, N. Gefen, Q. Zhu, R. Raghupathi, and S. S. Margulies, “Age-dependent changes in material properties of the brain and braincase of the rat,” *J. Neurotrauma*, vol. 20, no. 11, pp. 1163–1177, 2003.

[73] A. M. Okamura, C. Simone, and M. D. O’leary, “Force modeling for needle insertion into soft tissue,” *IEEE Trans. Biomed. Eng.*, vol. 51, no. 10, pp. 1707–1716, 2004.

[74] C. Boehler, C. Kleber, N. Martini, Y. Xie, I. Dryg, T. Stieglitz, U. G. Hofmann, and M. Asplund, “Actively controlled release of Dexamethasone from neural microelectrodes in a chronic in vivo study,” *Biomaterials*, 2017.

[75] Z. J. Sperry, K. Na, S. S. Parizi, H. J. Chiel, J. Seymour, E. Yoon, and T. M. Bruns, “Flexible microelectrode array for interfacing with the surface of neural ganglia,” *J. Neural Eng.*, vol. 15, no. 3, 2018.

[76] B. Rubehn and T. Stieglitz, “In vitro evaluation of the long-term stability of polyimide as a material for

neural implants," *Biomaterials*, vol. 31, no. 13, pp. 3449–3458, 2010.

[77] J. Ordonez, M. Schuettler, C. Boehler, T. Boretius, and T. Stieglitz, "Thin films and microelectrode arrays for neuroprosthetics," *MRS Bull.*, vol. 37, no. 6, pp. 590–598, 2012.

[78] P. R. Patel, H. Zhang, M. T. Robbins, J. B. Nofar, S. P. Marshall, M. J. Kobylarek, T. D. Y. Kozai, N. A. Kotov, and C. A. Chestek, "Chronic in vivo stability assessment of carbon fiber microelectrode arrays," *J. Neural Eng.*, vol. 13, no. 6, p. 66002, 2016.

[79] T. Stieglitz, H. Beutel, and J. U. Meyer, "'Microflex' - A new assembling technique for interconnects," *J. Intell. Mater. Syst. Struct.*, vol. 11, no. 6, pp. 417–425, 2000.

[80] A. Khurram, S. E. Ross, Z. J. Sperry, A. Ouyang, C. Stephan, A. A. Jiman, and T. M. Bruns, "Chronic monitoring of lower urinary tract activity via a sacral dorsal root ganglia interface," *J. Neural Eng.*, 2017.

[81] C. Rossant, S. N. Kadir, D. F. M. Goodman, J. Schulman, M. L. D. Hunter, A. B. Saleem, A. Grosmark, M. Belluscio, G. H. Denfield, A. S. Ecker, A. S. Tolias, S. Solomon, G. Buzski, M. Carandini, and K. D. Harris, "Spike sorting for large, dense electrode arrays," *Nat. Neurosci.*, vol. 19, no. 4, pp. 634–641, 2016.

[82] J. E. Chung, J. F. Magland, A. H. Barnett, V. M. Tolosa, A. C. Tooker, K. Y. Lee, K. G. Shah, S. H. Felix, L. M. Frank, and L. F. Greengard, "A Fully Automated Approach to Spike Sorting," *Neuron*, vol. 95, no. 6, pp. 1381–1394.e6, 2017.

[83] S. N. Kadir, D. F. M. Goodman, and K. D. Harris, "High-Dimensional Cluster Analysis with the Masked EM Algorithm," *Neural Comput.*, vol. 26, pp. 2379–2394, 2014.

[84] H. K. Yasuda, "Some Important Aspects of Plasma Polymerization," pp. 293–304, 2005.

[85] F. Ceyssens and R. Puers, "Insulation lifetime improvement of polyimide thin film neural implants.," *J. Neural Eng.*, vol. 12, no. 5, p. 054001, 2015.

[86] C. Boehler, T. Stieglitz, and M. Asplund, "Biomaterials Nanostructured platinum grass enables superior impedance reduction for neural microelectrodes," *Biomaterials*, vol. 67, pp. 346–353, 2015.

[87] A. Zátonyi, F. Fedor, Z. Borhegyi, and Z. Fekete, "In vitro and in vivo stability of black- platinum coatings on flexible , polymer microECoG arrays," 2018.

[88] Z. J. Sperry, K. Na, S. S. Parizi, H. J. Chiel, J. Seymour, E. Yoon, and T. M. Bruns, “Flexible microelectrode array for interfacing with the surface of neural ganglia,” *J. Neural Eng.*, 2018.

[89] G. Buzsáki, E. Stark, A. Berényi, D. Khodagholy, D. R. Kipke, E. Yoon, and K. D. Wise, “Tools for probing local circuits: High-density silicon probes combined with optogenetics,” *Neuron*, vol. 86, no. 1, pp. 92–105, 2015.

[90] C. Mora Lopez, J. Putzeys, B. C. Raducanu, M. Ballini, S. Wang, A. Andrei, V. Rochus, R. Vandebriel, S. Severi, C. Van Hoof, S. Musa, N. Van Helleputte, R. F. Yazicioglu, and S. Mitra, “A Neural Probe with Up to 966 Electrodes and Up to 384 Configurable Channels in 0.13 μm SOI CMOS,” *IEEE Trans. Biomed. Circuits Syst.*, 2017.

[91] K. A. Ludwig, N. B. Langhals, M. D. Joseph, S. M. Richardson-burns, J. L. Hendricks, and D. R. Kipke, “(PEDOT) polymer coatings facilitate smaller neural recording electrodes,” 2011.

[92] S. Paik, Y. Park, and D. D. Cho, “Roughened polysilicon for low impedance microelectrodes in neural probes,” *J. Micromechanics Microengineering*, vol. 13, pp. 373–379, 2003.

[93] X. C. Ong, M. Forssel, and G. K. Fedder, “Processing of platinum electrodes for parylene-C based neural probes,” in *MEMS*, 2016, vol. 180, no. January, pp. 509–512.

[94] F. Pothof, L. Bonini, M. Lanzilotto, A. Livi, L. Fogassi, G. A. Orban, and P. Ruther, “Chronic neural probe for simultaneous recording of single-unit, multi-unit, and local field potential activity from multiple brain sites.”

[95] A. N. Ivanovskaya, A. M. Belle, A. M. Yorita, F. Qian, S. Chen, A. Tooker, R. Garc, D. Dahlquist, and V. Tolosa, “Electrochemical Roughening of Thin-Film Platinum for Neural Probe Arrays and Biosensing Applications,” vol. 165, no. 12, 2018.

[96] C. Girardeauxa, E. Drueta, P. Demoncy, and M. Delamar, “The polyimide (PMDA/ODA) titanium interface . Part 1 . Untreated PMDA / ODA : an XPS , AES , AFM and Raman study,” *J. Electron Spectros. Relat. Phenomena*, vol. 2048, no. 94, pp. 11–21, 1994.

[97] C. Girardeaux, E. Druet, P. Demoncy, and M. Delamar, “The polyimide (PMDA-ODA) titanium interface.

Part 2. XPS study of polyimide treatments and ageing," *J. Electron Spectros. Relat. Phenomena*, vol. 74, no. 1, pp. 57–66, 1995.

[98] K. Miyauchi and M. Yuasa, "A study of adhesive improvement of a Cr-Ni alloy layer on a polyimide surface by low pressure gas plasma modification," *Prog. Org. Coatings*, 2013.

[99] H. Chen, P. Li, N. Umezawa, H. Abe, J. Ye, K. Shiraishi, A. Ohta, and S. Miyazaki, "Bonding and Electron Energy-Level Alignment at Metal/TiO 2 Interfaces: A Density Functional Theory Study," *J. Phys. Chem. C*, vol. 120, pp. 5549–5556, 2016.

[100] C. M. Lopez, A. Andrei, S. Mitra, M. Welkenhuysen, W. Eberle, S. Member, C. Bartic, R. Puers, R. F. Yazicioglu, and G. G. E. Gielen, "An Implantable 455-Active-Electrode 52-Channel CMOS Neural Probe," *IEEE J. Solid-State Circuits*, vol. 49, no. 1, pp. 248–261, 2014.

[101] J. Du, T. J. Blanche, R. R. Harrison, H. A. Lester, and S. C. Masmanidis, "Multiplexed , High Density Electrophysiology with Nanofabricated Neural Probes," vol. 6, no. 10, 2011.

[102] J. H. Zhang and Y. C. Chan, "Contact resistance and adhesion performance of ACF interconnections to aluminum metallization," vol. 43, pp. 1303–1310, 2003.

[103] S. Vahanen, "Solutions for flip chip bonding of future pixel detectors," in *VERTEX*, 2017.